PROCESS AND MECHANISM OF ULTRASONIC WELDING OF THERMOPLASTICS

LI XIANGCHAO

SCHOOL OF MECHANICAL & AEROSPACE ENGINEERING

NANYANG TECHNOLOGICAL UNIVERSITY

2005

Process and Mechanism of Ultrasonic Welding of Thermoplastics

Li Xiangchao

School of Mechanical & Aerospace Engineering

A thesis submitted to the Nanyang Technological University
in fulfillment of the requirement for the degree of
Doctor of Philosophy

2005

ABSTRACT

Ultrasonic welding of thermoplastics (UWT) is a complicated joining process in which many factors affect the welding process and weld quality. Although it is widely used for fusion bonding of thermoplastics, the mechanism of this joining process has not been well understood. Existing knowledge about UWT is largely qualitative based on extensive experience and trial-and-error studies. This research aims to better understand the thermal and mechanical aspects of the welding mechanism of this technique through precision measurement and numerical simulation.

A fundamental obstacle to fulfilling the objective had been that the existing technology has not been able to measure accurately the actuating force and velocity at the joint interface. The difficulties were due to the limited space available for installing sensors and the high frequency of both measurands for existing sensors. To overcome this obstacle, a sensor-less method is first developed for the in-situ measurement of the welding force and velocity. The method makes use of the existing actuating mechanism of the ultrasonic welding (UW) machine as the sensor simultaneously while it functions as the welding actuator. This capability was achieved by modeling the actuating mechanism as a 2 by 2 transduction matrix which relates the mechanical force and velocity at the joint interface with the input electrical voltage and current to the actuator. For a given UW machine, the transduction matrix is an intrinsic property. After the 4 elements of the transduction matrix were calibrated using a unique method, the aimed measurement is fulfilled by a simple matrix operation.

The measured force and velocity facilitates the study of the heat generation and transfer in welding samples. The equation governing the thermo-mechanical behaviour during UW was derived. Both the applied mechanical force and the dynamic compliance of the materials being welded are involved in the equation, in which the dynamic compliance can be evaluated from the detected mechanical impedance by the above sensor-less method. Using their variations as parameters, a finite element method was then employed to solve the governing equation with appropriate boundary and initial conditions. The numerical results coincide well with the temperatures measured at various locations in welding samples. This study successfully couples the high-frequency mechanical input with the temperature changes at the joint interface which causes the melting of thermoplastics under the welding process.

Since both the welding force and the velocity are obtainable by the in-situ sensor-less method, the impedance variation and the force versus displacement curve at any time spot during UW can be quantified. Referring to these two pieces of information and the qualitative descriptions in literature, a more accurate description of the welding mechanism of UWT was attempted. In this improved mechanism description, the welding process is divided into four distinct phases excluding the hold phase: the viscoelastic-plastic phase, the energy director melting phase, the melting completing phase and the upper & lower parts coupling phase. On the whole, the study clearly reveals that the mechanical impedance at the joint interface is the most characteristic variable of UW. It accurately and fully reflects the shifting of the phases, indicating the weldability at different welding parameters, signifying the weld quality and facilitating the investigation of the welding mechanism of UWT.

The viscoelastic-plastic behaviours of thermoplastics was then modeled by discrete models with time varying parameters for each of the phases through optimization to minimize the discrepancies between the impedances obtained from the models and the measurement. The validations of the models show that they are effective to model the mechanical behaviours of thermoplastics during UWT. The parameters of the models can further reveal the detailed characteristics of UW. Through these models, a tool was obtained for better understanding the welding process.

ACKNOWLEDGEMENT

It is my greatest pleasure to express my deepest gratitude to my supervisor, **Professor Ling Shih-Fu**, for his enthusiasm, encouragement and invaluable guidance. From him, I learnt much about my research and my life. The meetings and discussions with him have greatly contributed to this research project.

I am grateful very much to my co-supervisor, **Dr. Sun Zheng**, from the Singapore Institute of Manufacturing Technology, for his invaluable guidance, his correction of my writing, his kind help and support on the experiments.

My thanks also go to the research students, research staffs and technicians in the Mechanics of Machines Lab and the Centre of Micro Machine Systems Lab for their kind help, support and valuable discussions. Special thanks are given to Dr. Li Weihua, Dr. Ying Ming, Dr. Fu Lianyu, Dr. Liang Fenggang, Ms. Ng Lee Keow, Dr. Xu Limei, Ms. Yin Yanling, Mr. Xiao Zhiyun, Ms. Hou Xiaoyan, Mr. Wang Qiongbo, Mr. Jin Linfang, Mr. Xu Jianguo, Mr. He Hanxiang, Mr. Wang Deyang and Dr. Wen Guilin. Also thanks are given to Mr. Pan Dayou for his kind help on the experiments.

I am also grateful to Nanyang Technological University (Singapore) and Singapore Institute of Manufacturing Technology for granting me a Research Scholarship and providing funding to support this project.

Table of Contents

List of Figures

List of Tables

Chapter 1

Introduction

Ultrasonic welding is a popular technique for joining thermoplastics because the welding process is fast and economical. To improve the quality and productivity of the technique further, more understanding about the welding mechanism is necessary. In this chapter, the background and necessity will be described, which is followed by the objectives and scope of the research.

1.1 Background

Ultrasonic welding was accidentally discovered in 1950 when an investigator found that a weld was produced when the electrode of a spot welder was ultrasonically excited, even though no current was passing though it. Ultrasonic welding appeared in thermoplastic assembly lines in the beginning of 1960's because of massive use of thermoplastics. Now, ultrasonic welding is widely used in almost all major industries in which thermoplastics are assembled [1]: automotive industry, medical industry, chemical industry and electrical industry as well as others.

During ultrasonic welding, high frequency (20-40 kHz), beyond the range of human hearing, and low amplitude (0.001-0.025 mm) mechanical vibrations are applied to the

parts being welded. The vibrations generate heat at the joint interface of the welded parts, resulting in melting of the thermoplastic materials, and the weld is formed after cooling. Ultrasonic welding is one of the fastest welding techniques, with a weld time of less than one second. Ultrasonic welding is generally divided into near field welding and far field welding. In near field welding, the horn surface is less than 6 mm from the joint interface; while in far field welding, the horn surface is more than 6 mm from the joint interface [2].

1.1.1 Main Components of an Ultrasonic Welding System

An ultrasonic welding system mainly consists of a power supply, a converter, a booster, a horn and a fixture (Fig. 1-1). The power supply converts standard low frequency electricity into high frequency electrical energy. The high frequency electrical energy is converted by the converter into the mechanical vibrations of the same frequency. The booster increases or decreases the amplitude of the mechanical vibrations, and conveys the vibration energy to the horn. The horn further amplifies the amplitude of the mechanical vibration. It contacts the parts during welding and transmits the vibratory energy to the parts. The fixture holds the parts in place and applies pressure during welding in order to prevent movement or flexing of the welding stack [3]. For the welding process, the parts are loaded first, and then the welding process begins when the trigger force and the distance are reached by the horn. In this research, a typical ultrasonic welding system, Branson 900 from Branson Ultrasonics Co., USA, is employed for the investigation. In the following, a brief introduction to each component is given.

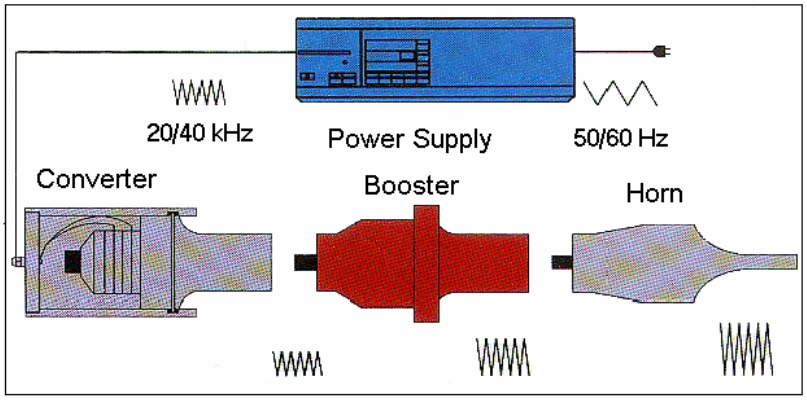

Fig. 1-1 Main components of an ultrasonic welding system [3]

Power Supply The power supply converts conventional low frequency and low voltage electrical power at 50/60 Hz and 120/240 volts into high frequency and high voltage electrical power at 20/40 kHz and 13 kV. It is designed to drive a converter at a specific amplitude, and it can come in a wide range of power capabilities. In order to allow an operator to adjust or reprogram the welding cycles, the power supply also contains all the electric controls. Through the power supply, we can select a welding mode, adjust the welding parameters, and save the collected welding data [4].

Converter The converter consists of two lead-zirconate-titanate (PZT) elements that transform the high frequency (20/40 kHz) electrical oscillations into the mechanical vibrations of the same frequency (see Fig. 1-2). The length of a converter is designed to be one-half wavelength at the operating frequency. The PZT material is an electroelastic material in which the link between deformation field and internal electric field is rather strong. When subjected to an alternating voltage, this element expands and contracts mechanically, causing the whole transducer assembly to resonate at the operating frequency [5]. The PZT elements make use of this characteristic to convert electrical power into mechanical power.

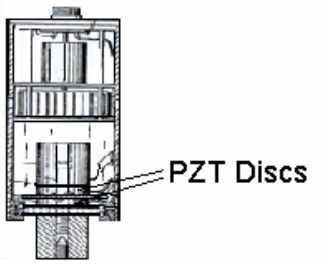

Fig. 1-2 PZT converter [5]

Booster The booster is a half-wave section made of aluminium or titanium. It is used to modify the amplitude of vibrations applied to the parts through the horn, so it is mounted between the converter and the horn and provides a clamping point for more rigid stack mounting. The booster is designed to resonate at the same frequency as the converter. In order to minimise the loss of energy and prevent sound transmitting into support column, the booster is usually mounted at a nodal (minimum vibration) point of the axial motion. The booster has different diameters and masses on either side of its nodal point to provide amplitude change (see Fig. 1-3) [6]. In this project, a titanium booster is used with the amplitude rate of 1:2.5.

Fig. 1-3 Boosters [6]

Horn The horn is usually selected or designed for a specific application (see Fig. 1-4). Each horn is a half-wave section that applies the necessary pressure to the parts to be assembled and transfers ultrasonic vibrations from the booster to the workpiece. For optimal energy transmission, the end of the horn that contacts the part is designed to mate with the part geometry. Depending on their profile, horns are referred to as stepped, conical, exponential, or catenoidal. The shape of the horn alters a gain factor. Depending on the applications, the horn can be made by titanium alloys, aluminium or steel. Aluminium horns are usually chrome-or nickel-plated or hard-coated, and are used widely [5]. In horn manufacturing, the acoustical impedance of the horn material determines the power loss in the horn, and the mechanical strength of the material determines the maximum amplitude that can be achieved.

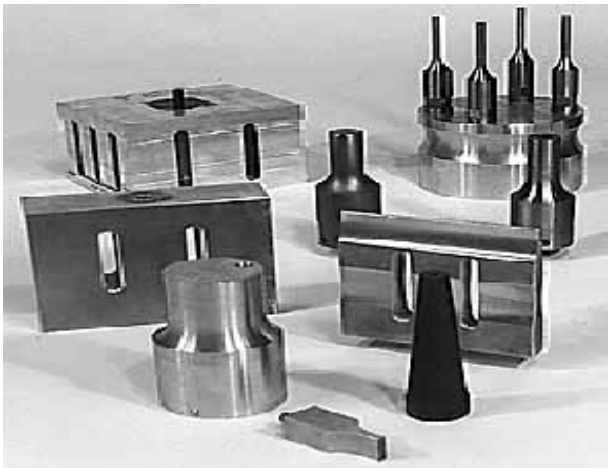

Fig. 1-4 Horns [5]

The Actuating Mechanism The mechanism containing the converter, the booster, and the horn is also called the actuating mechanism. It is the main working mechanism of an ultrasonic welding system. Fig. 1-5 shows the actuating mechanism used in this project, in which the converter is the standard from Branson, and the horn is made of aluminium and designed for standard welding samples, with the length 134.6 mm and the cross sectional area 68.5 mm * 13.05 mm touching the samples.

Fig. 1-5 The actuating mechanism

Fixture The basic purpose of the fixture is to align the parts and hold them stationary during welding. The parts to be joined must be held in alignment with respect to the end of the horn so that the uniform pressure between the parts is maintained during welding, and the process must be repeatable. The material to be welded, part geometry, wall thickness and part symmetry are all taken into consideration when designing the fixture.

1.1.2 Setting Parameters of an Ultrasonic Welding Machine

There are many machine settings in ultrasonic welding of thermoplastics, such as amplitude, pressure, weld time, hold time, trigger force, downspeed, etc. Among them, amplitude, pressure, weld time and hold time have a distinct influence on the welding process [7], which are discussed in the following.

Amplitude Amplitude is the vertical, vibratory, peak-to-peak movement produced by the converter, modified by the booster and fine-tuned by the horn. The vertical motion applied under pressure causes molecular friction at the joint interface of the thermoplastic parts being joined. The friction causes the plastics to melt and flow through the joint interface. As the amplitude is increased, greater amounts of energy are dissipated in the parts and this will give a stronger joint. However, when the

amplitude is more than a certain value, it will make a bad joint. It means there is an optimal amplitude range for a practical application. On the other hand, the amplitude needed is different in different conditions, such as welding materials.

Pressure The actual force or pressure applied to the thermoplastic parts is a critical variable needed to ultrasonically assemble the product. It provides contact between the horn and the parts for transmission of vibratory energy, and causes the energy director to flow and fuse with the parts. Pressure that is too low will result in poor energy transmission or incomplete melt flow. If pressures are too high, the greater melt volume results in molecular alignment in flow direction and decreases weld strength. The pressure needed for ultrasonic welding will vary with different applications. For example, large thermoplastic parts take more pressure than small parts. It has an optimal pressure range for certain application.

Weld Time Weld time is the amount of time that amplitude and pressure are applied to the parts in order to get a desired weld. Increasing the weld time generally increases weld strength until an optimal time is reached. Further increases result in either decreased weld strength or produce large amounts of flash. Weld time also varies according to the ultrasonic application. Small thermoplastic parts require shorter weld time than large parts. Obviously, weld time will change with materials.

Hold Time When a weld time ends, the horn does not move up immediately, but stays for a while. Hold time is the amount of time that the horn keeps on contacting the parts after weld time. It is used for the weld formation. Normally, **Welding Time** includes the amount of weld time and hold time.

1.1.3 Weldability of Thermoplastics in Ultrasonic Welding

The ultrasonic weldability of thermoplastics is defined by a number of mechanical and rheo-logical properties. Three main characteristics determine the weldability: molecular structure, melting temperature and melt flow rate. Among them, a similar melting temperature between the materials to be welded is a basic requirement for successful welding of rigid parts because a temperature difference can be sufficient to hinder the weldability [8].

Thermoplastic materials are categorized as amorphous and semi-crystalline, shown in Fig. 1-6 and Fig. 1-7. Amorphous materials have a structure with random molecular arrangement, and have a broad melting temperature, flow well, and resolidify gradually, so they are well suitable for ultrasonic welding in both near-field and far-field conditions. Semi-crystalline materials have areas of orderly molecular arrangement, and have a well-defined melting temperature and re-solidifying temperature. Thus, compared with amorphous polymers, they tend to weld less readily welding under far-field conditions. However, when both parts are of the same material and designed properly, semi-crystalline materials can also be ultrasonically welded. In this research, PP (Polypropylene) is used as an example of semi-crystalline materials, and PC (Polycarbonate) is used as an example of amorphous materials.

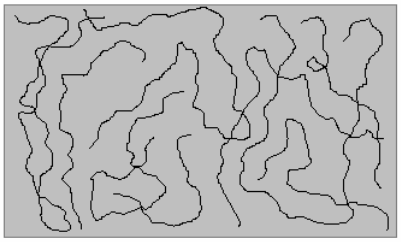

Fig. 1-6 Amorphous structure [8]

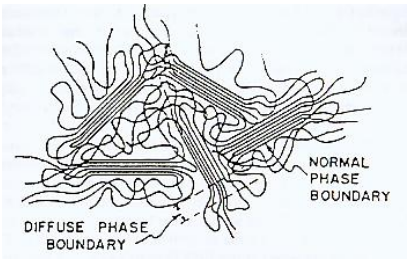

Fig. 1-7 Semi-crystalline structure [8]

1.1.4 AWS Standard Welding Sample for Ultrasonic Welding

For the purpose of comparison, the American Welding Society (AWS) standard samples suggested by the AWS G1 committee are employed, shown in Fig. 1-8 [9]. The sample consists of two parts. The lower part is a T shape structure, 50.8 mm long and 12.7 mm high. The width of the lower part surface is 2.54 mm. The upper part is also T shaped, but the height is only 6.35 mm. A triangular energy director is molded on the surface on which the upper part contacts with the lower part. After welding, the AWS samples form an 'I' beam.

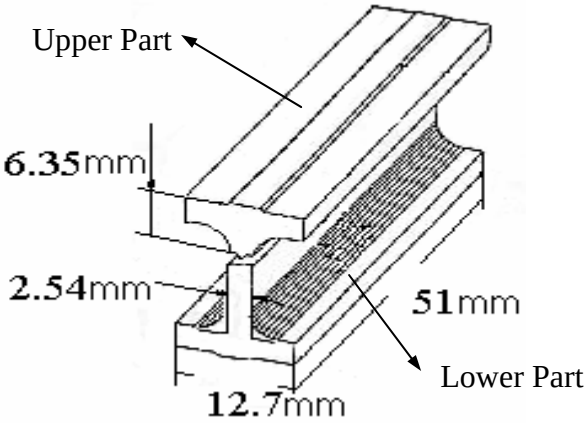

Fig. 1-8 AWS ultrasonic welding sample [9]

1.1.5 Issues in UWT to be Addressed

During ultrasonic welding, the mechanical forces and motions at the joint interface play the most important roles because they determine the weld quality and welding characteristics. However, it is very difficult to measure these variables accurately because no force sensor can measure the dynamic force exactly at such a high frequency, and there is very limited space to put the velocity sensor, especially in a real welding process.

Because of damping of thermoplastics, heat is produced from the mechanical vibrations during the welding process. The heating process directly affects the melting behaviours of the joint, and consequently affects the weld strength. However, the thermo-mechanical interaction during the heating process is not fully understood yet. Moreover, the time-varying temperature distributions of the cross sections in welding samples during the heating process are very important to study the heating process, while no instrument can measure the temperature distributions in such a short time.

Ultrasonic welding is a complicated process because many mechanical behaviours happen, such as viscoelastic deformation, plastic deformation, material melting, intermolecular friction, material coupling, intermolecular entanglement and autohesion. However, the existing studies have not revealed the welding mechanism clearly, and the effects of the machine settings on the welding mechanism are not fully clear. Furthermore, the mechanical behaviours of thermoplastics are also very important to study the welding process, but the available models (in the literature) for thermoplastics under welding are too simple to understand the process well.

1.2 Objectives

The study reported in this thesis aims to better understand the thermal and mechanical aspects of the welding mechanism of this technique through precision measurement and numerical simulation. Thus, the objectives of this research project are:

1. Develop an in-situ sensor-less method to measure the actuating mechanical force and velocity at the joint interface,
2. Investigate the thermo-mechanical interaction in ultrasonic welding of thermoplastics,
3. Investigate the welding mechanism of ultrasonic welding of thermoplastics
4. Model the mechanical behaviours of thermoplastics under welding.

1.3 Scope

In this research work, in order to measure the actuating force and velocity, a system dynamic viewpoint is taken to study the actuating mechanism. From this viewpoint, the actuating mechanism can be viewed as a two port device with an input port and an output port. The output mechanical force and velocity are related to the input electrical voltage and current by a transduction matrix. When the transduction matrix is made available, the output mechanical variables in real time can be indirectly detected from the input variables. In this thesis, the modeling of the actuating mechanism and the identification of the transduction matrix are presented in Chapter 3.

With the detected mechanical variables, the thermo-mechanical interaction in ultrasonic welding of thermoplastics is further understood. The governing equations of

heat generation and heat transfer are deduced. A finite element model was used to solve the equations to reveal the dynamic thermal behaviours during the heating process. The characteristic heating process is investigated via experiments to validate the simulation. The theoretical analysis, simulation and experiment of the thermo-mechanical interaction are presented in Chapter 4.

The welding mechanism in ultrasonic welding of thermoplastics is further understood with the heating characteristics of the welding process and the detected mechanical variables. The mechanical impedance and the force-displacement curve can reveal well the mechanical behaviours of ultrasonic welding. The effects of main machine settings on the mechanical impedance are also investigated via experiments. The electrical impedance can be used to monitor the weld quality produced by ultrasonic welding. The mechanical behaviours of thermoplastics under welding are modeled based on the welding mechanism of ultrasonic welding of thermoplastics. Chapter 5 presents the description of the welding mechanism and the studies of the mechanical impedance and the electrical impedance. Chapter 6 presents the modeling of the mechanical behaviours of thermoplastics under welding.

Chapter 2

Literature Review

From the literature, we found that the knowledge about ultrasonic welding is largely qualitative, and mainly obtained from practical experience and trial-and-error investigations based on the data acquired by indirect measurement of operating conditions. In this chapter, the information from literature is reviewed in five areas. First, in order to investigate the thermo-mechanical interaction and the welding mechanism of ultrasonic welding, the achieved results about the heating mechanism and the welding mechanism of ultrasonic welding of thermoplastics are reviewed. Then, since accurate measurement of the forces and motions at the joint interface is difficult, the measurement methods through modeling of ultrasonic welding system are presented. The materials modeling under ultrasonic welding are also investigated to study the mechanical bahaviours of the welding process. Lastly, the available methods for the measurement of the dynamic modulus of thermoplastics in ultrasonic welding are discussed because they are important for the study of the heating mechanism.

2.1 Heating Mechanism in UWT

Menges and Potente [10] studied the weldability of thermoplastics in ultrasonic welding. In their study, Plexiglas, polycarbonate and polystyrene samples with a

triangular energy director were used. They measured the distribution of vibration amplitude and the temperature in the energy director, and found that the heat was produced mainly by internal friction instead of interface friction. They also found that the maximum vibration amplitude corresponded to the maximum energy generation. Based on their observations and calculations, an index, which is a function of material properties, geometry, vibration frequency and weld pressure, was suggested.

Aloisio, et al. [11] investigated the ultrasonic welding of polycarbonate, ABS and Nylon using rectangular energy directors. They used elastic analysis to estimate the strain amplitude within the parts. Using the viscoelastic model, they predicted the initial temperature rise rate within the energy directors during ultrasonic welding, which agreed fairly well with their experimental data. The results showed the gradients of around $1000\,^{o}C/s$ in the early beginning of welding. It means the temperature increases sharply and reaches polymer's transition or melting temperature in a very short time.

Mori [12] investigated the effects of vibration strain distribution in long plastic rods on the amount of heat generated in the welding process. He found that the highest temperature rise rates were produced at displacement nodes. This was because the maximum stress and strain occurred at a displacement node. This was confirmed by Ng [13] in studying the vibration and heating mechanism during welding with finite element method. To improve the understanding of vibration and viscoelastic heating, a simpler structure of a flexural beam was studied to obtain the viscoelastic beam solutions. It was found that the hot spots were at the displacement nodes that corresponded to the peaks in strain and stress due to bending.

Tolunay et al. [14] studied the heating and bonding mechanism in ultrasonic welding of thermoplastics. The samples without energy directors were made from polystyrene. They found that increasing the static pressure resulted in higher power levels, although bond strengths did not differ substantially. Fig. 2-1 and Fig. 2-2 show the experimental diagram and results. They measured the temperature changes in the interface ($T_{IF,}$ "4" location in Fig. 2-1) and inside the parts being welded (T_1, $T_{2,}$ "2" and "3" locations in Fig. 2-1). Based on the analysis of their experimental data, they found that the most rapid heating occurred at the interface, probably due to the energy dissipation in the highly stressed surface asperities on which the stress concentrated, and the force had an appreciable effect on the heating rate, both at the interface and within the interior part. The heating rate at the interface was greatest ($>10{,}000\,^{o}C/s$), but slowed markedly after the interface temperature reached approximately $250\,^{o}C$. The rises of the two internal temperatures were significant over longer times and were caused by viscous dissipation associated with local strain oscillations. They also developed models for bulk heating and interface heating, including one dimensional heat conduction. Based on their experimental results and models, they concluded the bonding strength increased with time at the elevated temperature as diffusion interlinks polymer chains from the interface.

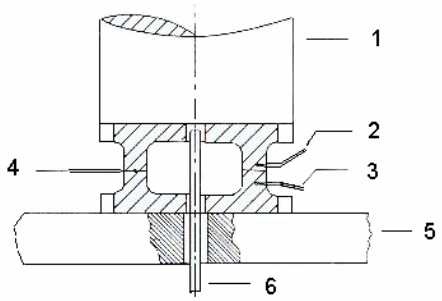

Fig. 2-1 Tolunay's experimental diagram [14]

1. Horn 2.3.4. Thermocouples 5. Base 6. LVDT

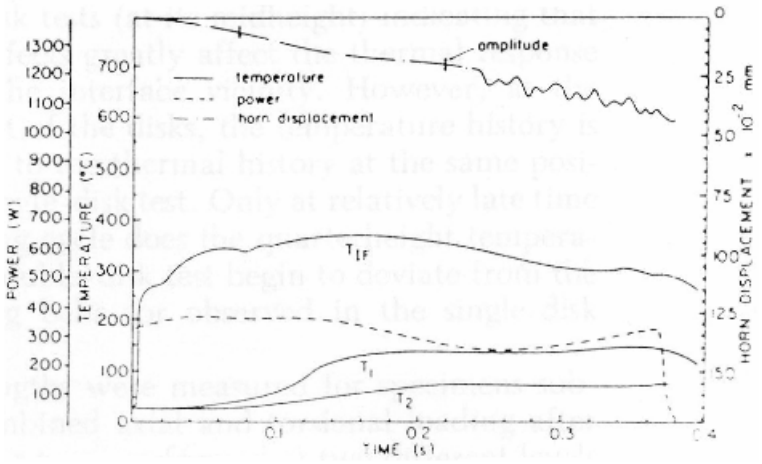

Fig. 2-2 Experiment results of temperature, power, and horn displacement traces [14]

Tateishi, et al. [15-16] studied the ultrasonic welding of oriented polypropylene (OPP) using tie-layer material whose function was like energy directors. Two thermocouples were embedded in the tie-layer material: one was at the centerline; the other was at the OPP/tie-layer interface (see Fig. 2-3). They measured the temperature of the two points during welding, shown in Fig. 2-4.

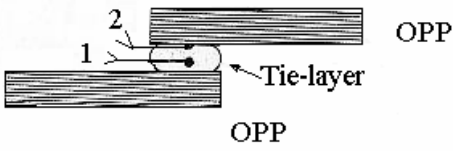

Fig. 2-3 Placement of thermocouples in the weld specimen [15]

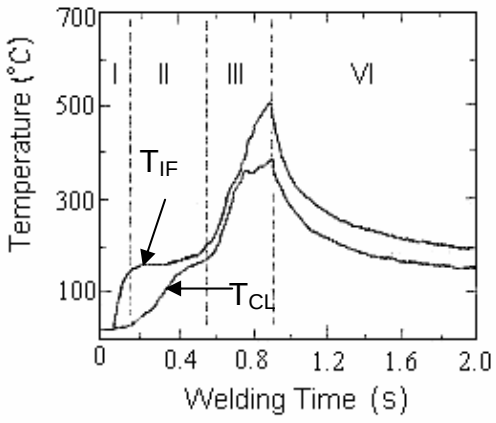

Fig. 2-4 Temperature T_{IF} and T_{CL} vs. time [15]

From the curves, the temperature of the OPP/tie-layer interface T_{IF} increased quickly to 160~170^{o}C, which was close the melting temperature of tie-layer, within less than 50 ms. The rate of the temperature rise ranged from 4000 to 5000$^{o}C/s$. However, the temperature at the centerline T_{CL} rose slowly compared with that at the OPP/tie-layer interface. This was because the stresses within the asperites on the contacting surface were much higher than that in the material far from the interface. These asperities were actually small energy directors. T_{IF} kept constancy while T_{CL} continued to increase gradually till the tie-layer material softened and flowed. And then T_{IF} and T_{CL} increased together. According to the temperature curves, the ultrasonic welding cycle could be divided by four distinct phases: Phase I, heating occurred because of the high stresses generated in asperities at the OPP/tie-layer interface; Phases II, melting occurred at the interface and the tie-layer temperature rise to the melting point; Phase III, melted polymer heating rapidly as a result of viscous dissipation; and finally, Phase IV, the tie-layer cooled and weld formed. These phases could also be recognized in the horn displacement curve (Fig. 2-5). They also found that the total time required for completion of the welding operation decreased with the increase in both vibration amplitude and applied pressure.

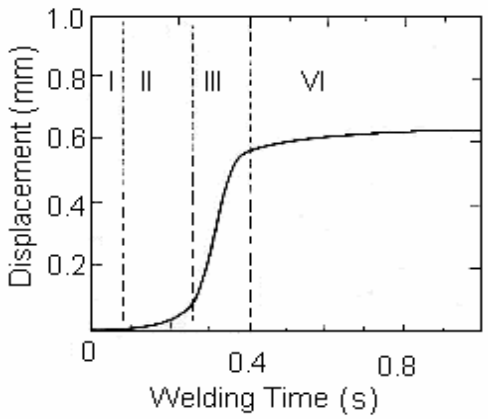

Fig. 2-5 Horn displacement vs. time [15]

Benatar [17-20] analysed the heat transfer and flow during ultrasonic welding. From his work, the heat flow and the local dissipation in the weld zone depended on the temperature distribution because the properties of plastics are acutely temperature dependent (the frequency is fixed at 20 kHz). However, he could not get the temperature distribution during the welding process.

2.2 Mechanism of UWT

Land et al. [21] recorded the ultrasonic welding of polycarbonate, ABS and Nylon with a high speed camera. From the analysis of the movie, they observed that the development of the process was not continuous but occurred in stages. The gap between the upper part and the lower part decreased for a short time, and then it remained constant for a while, and finally decreased again. Benatar [17-20] used a high speed video to videotape the ultrasonic welding of PEEK APC-2 composites at a rate of 1000 frames per second. He measured the variation of the gap between the composites and reached the same conclusion namely that ultrasonic welding occured in steps.

Benatar [17-20] did much research work in ultrasonic welding of plastics to investigate the welding mechanism. The welding process, in his concept, could be modeled by a five-part model that included mechanics and vibration of the parts, viscoelastic heating, heating transfer, flow and wetting, and intermolecular diffusion. He modeled the five subprocesses, which were distinct yet highly coupled.

The mechanics and vibration model was used to evaluate the strain distribution within the parts. Through the strain values and viscoelasticity, the heat dissipated in materials could be determined. In his study, the energy director was molded to concentrate welding energy. Some of the vibration amplitude was taken up by other parts (like part bodies, base, fixture, etc.) in the system instead of the energy director. Heat transfer and flow were also analyzed in his study. The energy balance in the welding zone was dictated by local dissipation of energy, heat diffusion to the solid plastic and the squeezing out of hot, low viscosity polymer. The squeeze flow apparently was an important factor in cooling the weld zone. When the molten plastic can flow freely this mechanism may be self-regulating. The hottest plastic had the lowest viscosity and was squeezed out preferentially. When the weld became too cold, the flow and thereby the cooling stopped. At the end of the welding process, the mechanical impedance of the joint interface rose rapidly when the melt fronts met.

Coupling the four subprocesses, the overall model is shown in Fig. 2-6. Starting with the original geometry, the lumped model was used to calculate the mechanics and vibrations of parts. From the estimated strains, the viscoelastic heating was calculated or the lumped model could be used to calculate the energy dissipated by dampers. Then, the finite element heat transfer program was activated to determine the temperature rise. If melting occurred, the flow model was used to determine the effective impedance of the molten layer. The material properties and geometry of parts were updated. The sequence was repeated until the welding process was completed.

One very important conclusion in Benatar’s study was that the mechanical impedance of the joint interface would change sharply when the melt fronts met. He thought the

mechanical impedance could be used to monitor the states and geometry of the energy director and thus monitor weld quality. However, measuring the mechanical impedance at high frequency and high dynamic loading was extremely difficult. Inertial effects and compliance of the fixture and the base plate were important, yet the force and displacement could not be easily measured. He measured the acceleration of the fixture and base whose impedance was known instead of measuring the mechanical impedance itself, because he thought the increase of the mechanical impedance of interface would increase the power dissipated and the acceleration of the fixture.

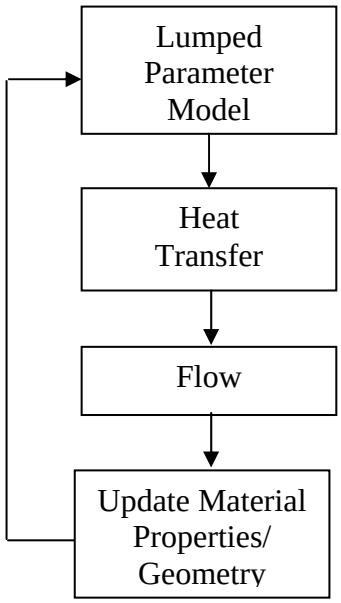

Fig. 2-6 Overall process model of ultrasonic welding [17]

Nonhof, et al. [22-23] gave the optimization and estimation for process condition during ultrasonic welding of thermoplastics. The process condition mainly consists of deformation of the product under the welding force, energy dissipation during the welding process, material flow of material after melting, thickness of weld zone and acoustical damping of the acoustical wave injected into the product.

Based on the penetration of the product parts, ultrasonic welding was divided into four phases by Netze [24], shown in Fig. 2-7. In Phase I, the solid material, especially the energy director, was heated to the softening point. In Phase II, the welding zone developed and the plastic started to flow out of the welding zone. In Phase III, as much plastic flowed out of the welding zone as was added to it, which leaded to a steady state. Phase IV started with turning off the ultrasonic generator. The weld zone solidified, and a weld was made.

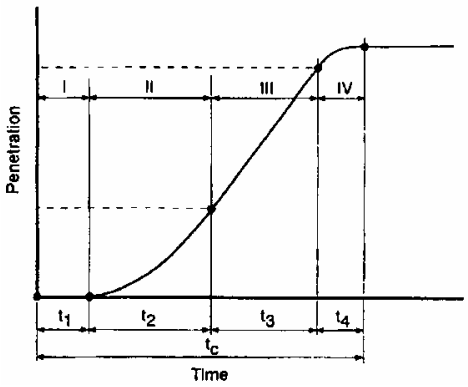

Fig. 2-7 Division of ultrasonic welding using the penetration [24]

Ultrasonic welding could also be divided into four phases based on welding displacement by Michaeli [25], shown in Fig. 2-8. In the first phase, the energy director started to melt. The melting rate fell steadily with increasing area of the energy director. In the second phase, the upper and lower parts were coupled together. The melting rate remained constant for a certain period of time. The third phase was characterized by steady-state melting behaviour. A constant melt layer thickness formed in the weld. During the fourth phase, the holding phase, additional melt was squeezed out by the horn. The structure and morphology of the weld were generated and frozen in place by the cooling process, which commenced at the same time.

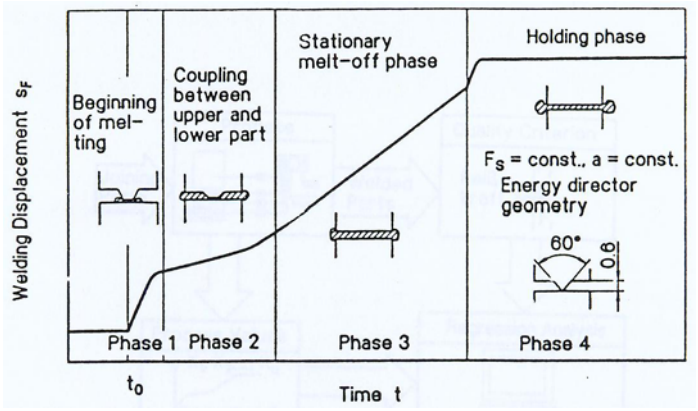

Fig. 2-8 Schematical behaviour of the welding displacement during ultrasonic welding with an energy director [25]

Shih-Jung Liu, et al. [26-27] and Weihua Shi [28] studied the effects of machine settings on ultrasonic welding efficiency. From their results, weld time, amplitude and pressure were the most critical parameters. Optimum weld times could be found that will yield the best welding efficiency. However, the hold time had minor effects on the ultrasonic welding efficiency. For amplitude and pressure, amplitude had more effects on welding strength than pressure. The effects of machine settings on the weld strength were also studied in their papers. The amplitude of vibrations strongly affected the weld strength obtained. Increasing the amplitude of vibrations enhanced the energy dissipated and strength. Increasing the weld time increased the weld strength initially, but further increases in weld time caused a decrease in the weld strength.

2.3 Modeling of Ultrasonic Welding System

Benatar [17-20] proposed a mechanics and vibration model for a composite welding system. Since the thickness of the composite parts used in his work was much less compared to the acoustical wavelength of the material at 20 kHz (it is about 12.5 cm

for composites), he used a lumped parameter dynamic model (shown in Fig. 2-9) for the whole system including a converter, a booster, a horn, composite parts, a fixture and a base. In this model, all elements are connected by springs and dampers according to the material properties.

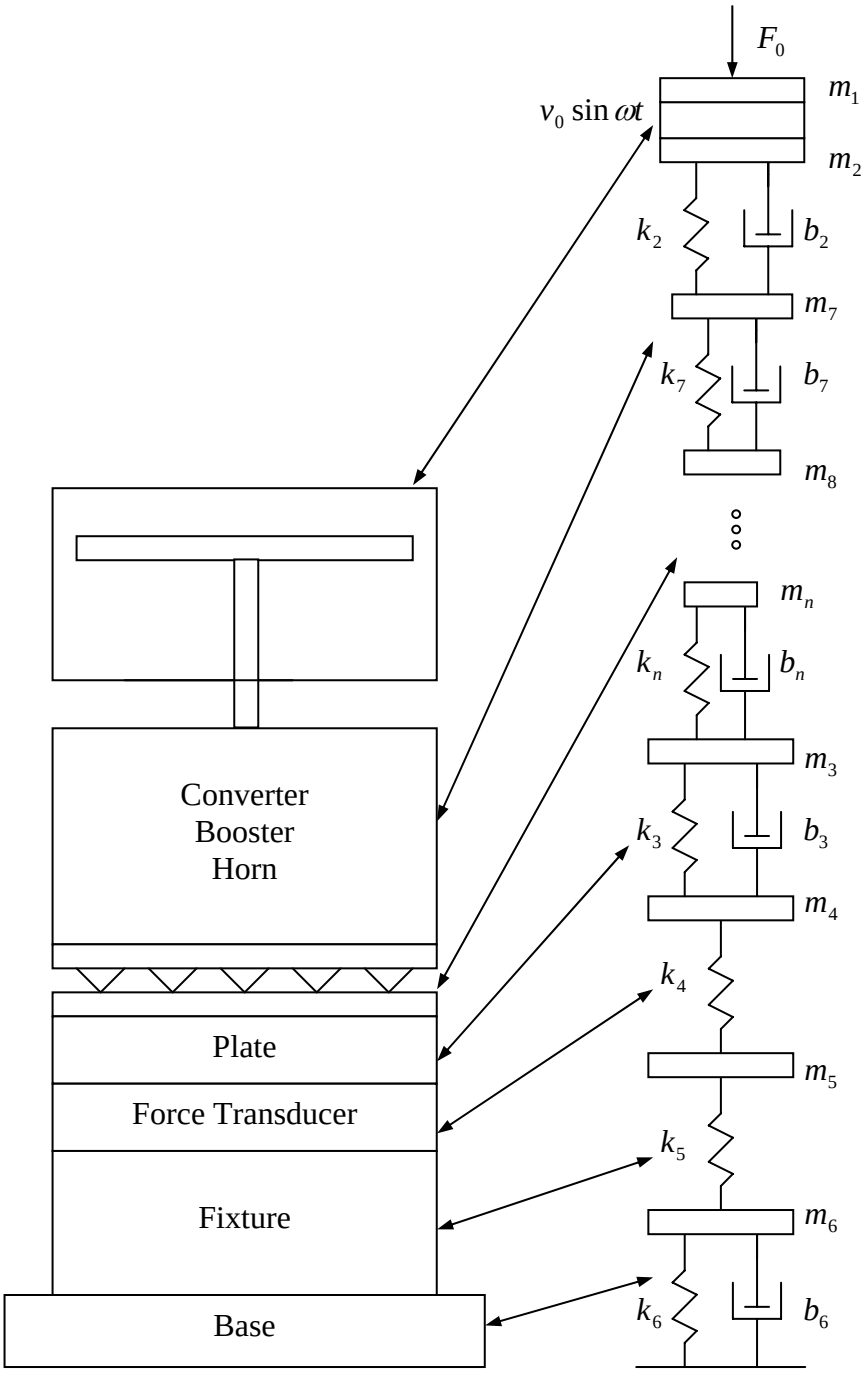

Fig. 2-9 Composite welding system and corresponding lumped parameter model [17]

Fugui [29] simplified Benatar's complicated model and proposed an electromechanical analogy model (Fig. 2-10) for the whole system to study the welding process. According to network theory, the actuating mechanism of ultrasonic welding system can be regarded as a filter. C_C is the equivalent capacitor for the converter; C_m and L_m are equivalent capacitor and inductor for the booster and horn assembly; C_L, L_L and R_L are the equivalent capacitor, inductor and resistor for the workpiece. The combination of the two circuits and the power supply circuit makes the whole model.

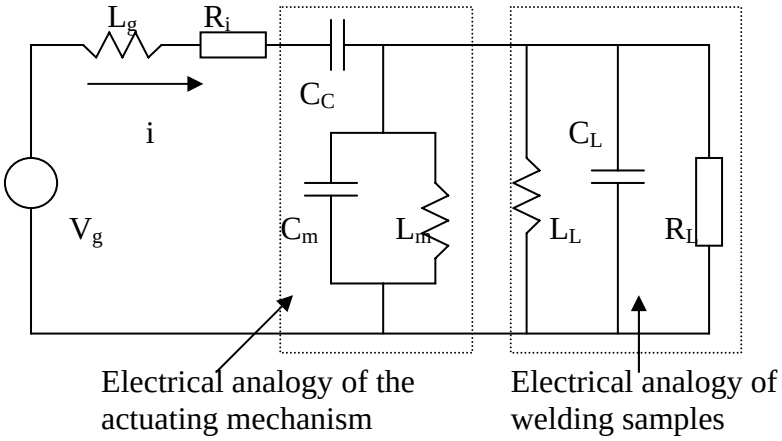

Fig. 2-10 Electromechanical analogy model of ultrasonic welding system [29]

Based on this system model, he measured the voltage and current of the actuating mechanism and calculated the input electrical impedance and input power. After compared the input electrical impedance and input power curves, he thought the electrical power level could be used as a process parameter. According to this idea, He proposed open loop control tests with power level as a control parameter to show that the strength of welding joint was strongly related to the power level. However, because of the uncertainties in the process caused by unpredictable changes of the system properties and external disturbance, his method was not very successful to control the weld quality.

Fu Si and Masao [30] studied an ultrasonic welding system constituting a feedback transducer, a driving transducer, an exponential horn and an anvil. In order to measure the acoustic impedance on specimen, they developed an equivalent circuit of the vibration system around resonant frequency, shown in Fig. 2-11. From the derived acoustic impedance, they found that the acoustic impedance was time-dependent. The acoustic impedance under different amplitudes and pressures of the welding machine were measured. They concluded amplitude and pressure were two of the key welding process parameters that were relative to weld quality, and the reactance of the specimen was dominant in ultrasonic plastic welding.

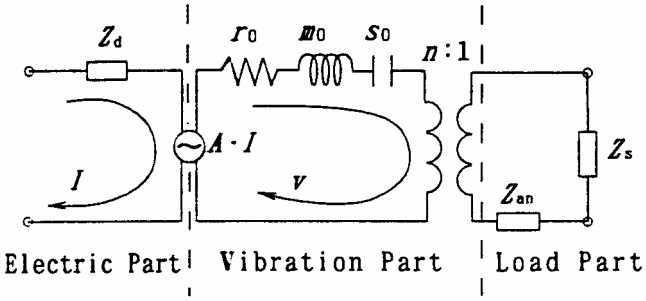

Fig. 2-11 Equivalent circuit of transducer system around resonant frequency [30]

Wijk, et al. [23] studied an ultrasonic welding system containing a welding actuator, a product part and an anvil. In order to measure the impedance of the welding head when placed on a product, a simple electrical analogue of a welding head was used, shown in Fig. 2-12. In this circuit, C_P and C_S are the parallel and series capacitances, respectively, and L is the inductance. R is the resistance, which is affected by the loading of the welding head with the product parts and anvil. From the experimental results, they found that the impedance interfered with a proper welding process. However, the parameters for the equivalent circuit were very difficult to estimate exactly because of the complicated system and the high working frequency.

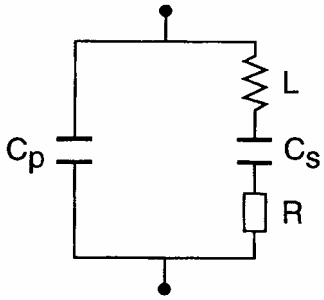

Fig. 2-12 Simple electrical analogue of a welding head [23]

Jingen Luan [31] studied the actuating mechanism of an ultrasonic welding system using two-port theory. Each subsystem of the actuating mechanism can be presented by a two-port model with two input variables and two output variables, so the overall model is shown in Fig. 2-13. In this model, E and I are the input voltage and current to the converter; F and V are the output force and velocity of the horn.

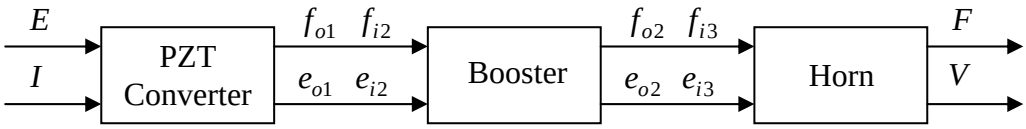

Fig. 2-13 Two-port model of subsystems of the actuating mechanism [31]

According to the two-port model, the actuating mechanism was modeled as

$$\begin{bmatrix} E \\ I \end{bmatrix} = \begin{bmatrix} S_{11} & S_{12} \\ S_{21} & S_{22} \end{bmatrix} \begin{bmatrix} F \\ V \end{bmatrix}$$

The details about this model will be reviewed in Chapter 3. For the transduction matrix, in Luan's work, S_{11} and S_{21} were evaluated using two sets of voltage, current, velocity data points (E_1, I_1, V_1) and (E_2, I_2, V_2) under two conditions from:

$$S_{11} = \frac{V_1 E_2 - V_2 E_1}{E_2 I_1 - E_1 I_2}$$

$$S_{21} = \frac{V_1 I_2 - V_2 I_1}{E_2 I_1 - E_1 I_2}$$

S_{12} was evaluated using the voltage E and the velocity V when the force F is 0:

$$S_{12} = \frac{E}{V}\Big|_{F=0}$$

S_{22} was calculated from the following equation:

$$S_{22} = \frac{S_{12} \times S_{21} + 1}{S_{11}}$$

However, in his evaluation, the two sets of voltage, current, velocity data points (E_1, I_1, V_1) and (E_2, I_2, V_2) under two conditions were uncertain, and the last equation should be used for validation, not for calculation. Furthermore, the processing of the data was not efficient in his work. Therefore, his method was not proper and caused inaccuracy in the measurement results.

2.4 Materials Modeling under Ultrasonic Welding

In ultrasonic welding, rectangular energy directors are rarely used, but they are much easier to analyze. Doyle [32] and Benatar [17-20] studied the heating rates in PEEK APC-2 composites with rectangular energy directors. Since the parts were thin (at most 2 mm) compared to the wavelength at 20 kHz (about 13 mm), they used a lumped parameter model for the parts (see Fig. 2-14). The lumped masses accounted for inertial effects, and Voigt-Kelvin models described the viscoelastic materials. The heat flow was modeled using one-dimensional heat conduction. The model agreed very well with experimentally measured temperature rise rates (see Fig. 2-15) showing that a lumped parameter model was effective in describing the heating during ultrasonic welding.

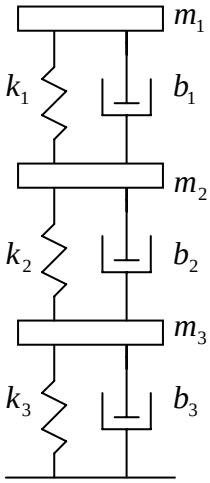

Fig. 2-14 Lumped parameter model for parts with rectangular energy directors [32]

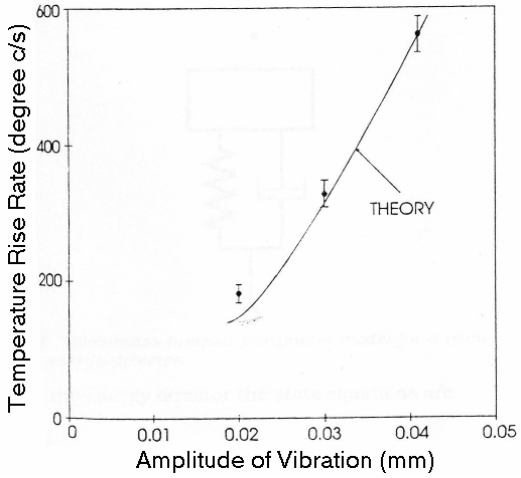

Fig. 2-15 Effect of vibration amplitude on the initial temperature rise rate for composites with rectangular energy directors [32]

Benatar [17-20] used a linear viscoelastic model for a triangular energy director when the energy director was divided into many equivalent rectangular masses, each with a spring constant and damping coefficient (see Fig. 2-16). The advantage of the linear model was that the solution of the equations was simpler.

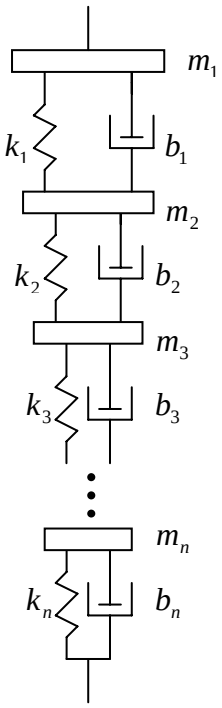

Fig. 2-16 Multi-mass lumped parameter model for a triangular energy director [18]

Fugui [29] simplified the multi-mass lumped parameter model by assuming that all deformations happen within the energy director. Because the average cross sectional area of the energy director was much smaller than other portion of the top part, and the mass of energy director was only 0.5% of the top part, the top part of the sample could be represented by a mass and the energy director was represented by a spring and a damper in parallel (see Fig. 2-17).

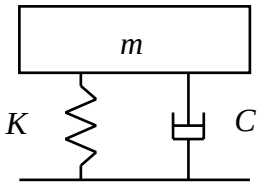

Fig. 2-17 Model of welding process [29]

Based on Fugui He's work, Luan [31] developed the model as a time-varying model (see Fig. 2-18). The mass of this model was actually the mass of the upper part

including the energy director, and it changed little during welding, so he thought it kept constant. Because the temperature was the function of time during ultrasonic welding, the material properties were functions of time. Additionally, the contact area between the two parts increased while the energy director melted during welding, so the stiffness coefficient and the damping coefficient must be time-varying.

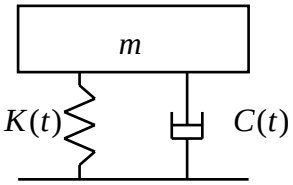

Fig. 2-18 Time-varying viscoelastic model of welding process [31]

2.5 Dynamic Modulus of Thermoplastics during UWT

For viscoelastic materials, the heat generation rate and the change of the temperature depend on the dynamic modulus of the materials. The dynamic modules both vary with temperature and frequency. For ultrasonic welding, the welding system only works at one single frequency. Therefore, the dynamic modulus is only a function of temperature for a given material. However, the dynamic modules were difficult to measure because of high working frequency.

Potente [33] and Benatar [17-20] measured the dynamic modulus of thermoplastics using time-temperature superposition, which used the collected data at lower frequencies to estimate the dynamic modulus at 20 kHz using the time-temperature shift factor. This methodology involves the assumptions in regard to linear viscoelastic behaviours and constant properties, such as temperature independent density, when shifting temperature data. The applicability of this technique is questionable in the case

of semi-crystalline polymers because they do not obey the superposition principles even at low strain levels. Barbari and Menges [34] used a linear viscoealstic model to derive a correlation between the loss factor and measurable parameters. However, these two methods were not reliable for such a high frequency [15].

Ng [13] used flexural resonance method to determine the dynamic modulus of thermoplastics at 20 kHz. For this method, the vibration amplitude was measured over a range of frequencies. Then the resonant frequencies were determined by locating the frequencies that produced peak amplitudes. The dynamic modulus was calculated using the resonant frequencies at different temperatures, shown Fig. 2-19 and Fig. 2-20. However, this method is so complex and difficult to achieve.

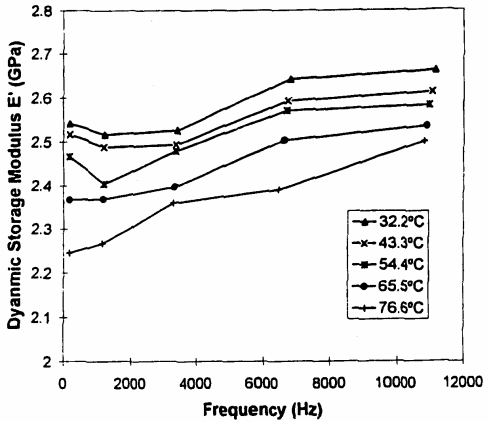

Fig. 2-19 Dynamic storage modulus at the different temperatures [13]

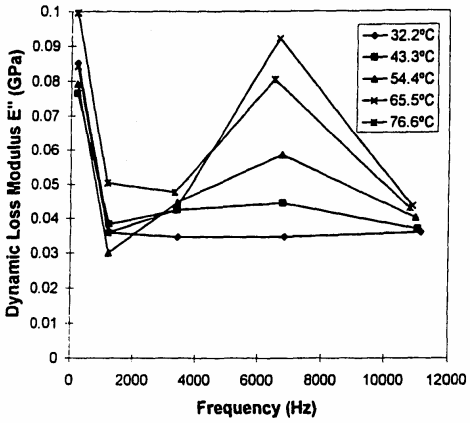

Fig. 2-20 Dynamic loss modulus at the different temperatures [13]

Chapter 3

Measurement of Forces and Motions at Joint Interface

Literature review in the above reveals that the lack of ability to measure the welding force and velocity at the joint interface in-situ has been an obstacle to quantitative modeling of the welding process. In this chapter, the simultaneous sensing and actuating using transduction matrix will be developed and employed in the actuating mechanism of ultrasonic welding system to measure accurately the welding force and velocity. The results show that the welding force and velocity can be derived from the input voltage and current through the transduction matrix of the actuating mechanism.

Then, the experimental method is used to identify the transduction matrix for Branson 900 system. The transduction matrix is calculated using a new developed signal processing and data processing method. The validation of the evaluated transduction matrix shows the force and velocity at joint interface can be easily detected by measuring the input electrical voltage and current of the actuating mechanism. From these quantities, the mechanical impedances at joint interface in deferent cases are detected. In addition, an equivalent circuit of the actuating mechanism is also studied to reveal the relationships between the transduction matrix and the system properties.

3.1 Simultaneous Sensing and Actuating using Transduction Matrix

In order to measure the welding force and velocity at the joint interface, simultaneous sensing and actuating using a transduction matrix is employed. In this section, the concept of simultaneous sensing and actuating is introduced first, and then the definition of transduction matrix is explained. Using transduction matrix, the loading effect of the actuator can be decoupled from the measurement. Lastly, the main applications of the transduction matrix are presented.

3.1.1 Simultaneous Sensing and Actuating

Transducers convert one form of energy to another. They are generally divided into two classes: sensors and actuators. Sensors are the devices that can monitor a parameter of a system. Actuators are the devices that can impose a state on a system. It has been thought for decades that any transducer in operation functions either as a sensor or as an actuator at any given moment, but not as both simultaneously.

In the past few years, dynamically characterizing structure of doubtful integrity has drawn more and more interests. The structure under test is usually excited by an actuator, and its response to the excitation is measured at the same time. Actuators and sensors are widely used as parts of frequency response measurement system. However, the loading effects introduced by the conventional transducers are often unsatisfactorily too big. Thus achieving high measurement accuracy as well as reducing the complexity of the measurement system is in great demand.

In late 1990s, Ling, *et al.* developed simultaneous sensing and actuating technology [31, 35-50], in which an actuator serves as a sensor simultaneously. The device, which could perform sensing and actuating simultaneously, is thus called a simultaneous sensing and actuating device. A few simultaneous sensing and actuating devices have been applied in many areas, such as obtaining the material properties of micro-specimen, monitoring of wire bonding, and so on. Many efforts have been devoted to exploring if an actuator can function as a sensor simultaneously.

Sensors are often specially designed and fabricated from a certain type of smart materials to effectively sense certain external stimuli. For real sensors, it is not possible to achieve the ideal of a sensor which measures a measurand while having absolutely no affect on it, because the act of making a measurement requires either adds or subtracts energy to or from the system. It is also impossible to achieve the ideal of a load-independent actuator, because there is always a load from the system under testing to the actuator. Using simultaneous sensing and actuating, the actuator performs actuating and sensing at the same time, so the output values of the actuator can be determined from the input values, just like the conventional sensors. From this, we need not add any sensor to get the output values if we know the characteristics of the actuator. It is very useful for those actuators whose output values are difficult to measure and whose input values are easy to measure. Using simultaneous sensing and actuating, the loading effects of the simultaneous sensing and actuating device on the structure under testing and the loading effects of the structure on the simultaneous sensing and actuating device are also de-coupled from the measurement. This method also decreases the number of transducers involved, and subsequently, lowers down the maintenance cost.

3.1.2 Transduction Matrix

According to two port theory, some devices can be viewed as two ports: input port and output port, in which each port is defined by two power conjugate variables, making for a total of four variables for the device. Power conjugate variables are two variables which when multiplied yield the power in a given energy domain. The standard power conjugate variables for different energy domain are listed below:

Translational: force, F, and velocity, V.

Rotational: torque, τ, and angular velocity, Ω.

Electrical: voltage, E, and current, I.

Magnetic: magnetomotive force M, and time rate of change of magnetic flux, $d\Phi / dt$.

Fluid: pressure, P, and volume flow rate, Q.

Thermal: temperature, T, and time rate of change of entropy, ds/dt.

Two of these variables are designated as independent, and the remaining two variables are determined by the details of the device, so they are dependent variables. Fig. 3-1 is a conventional model using two input variables and two output variables.

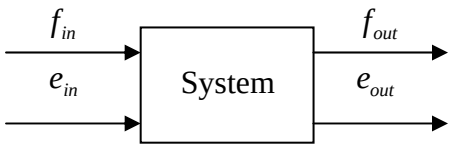

Fig. 3-1 Conventional two port model [51]

For the two port model, the relationships between the input variables and the output variables can be written as

$$e_{out} = Ae_{in} + Bf_{in}$$

$$f_{out} = Ce_{in} + Df_{in} \tag{3.1}$$

The relationships can also be described by the following equation

$$\begin{bmatrix} e_{out} \\ f_{out} \end{bmatrix} = \begin{bmatrix} A & B \\ C & D \end{bmatrix} \begin{bmatrix} e_{in} \\ f_{in} \end{bmatrix} \tag{3.2}$$

where, e_{in}, f_{in} are input variables; e_{out}, f_{out} are output variables; the matrix containing A, B, C, and D is called transduction matrix. For linear systems, the transduction matrix is usually the functions of frequency only, reflecting the system dynamic characteristics, and it is independent on input and output variables. The advantage of transduction matrix is to develop the relationships between input variables and output variables without caring much about details of the system studied.

Generally, there are three necessary factors for a transduction matrix. The first one is that the system should be a linear system; the second one is that there is no internal energy production or consumption in the system; the third one is that the system must obey the reciprocity theorem. Regarding the linearity of the system, the transduction matrix of the system is independent on the input or output variables. In other words, they are set by the system characteristics (such as mass, nominal capacitance, etc.). Once the system is set up, the four elements of the transduction matrix are constants if the frequency is fixed.

Regarding the reciprocity theorem, if the input variables of the system are unknown while the output variables are known, Eq. (3.2) can be rewritten as

$$\begin{bmatrix} e_{in} \\ f_{in} \end{bmatrix} = \begin{bmatrix} A & B \\ C & D \end{bmatrix}^{-1} \begin{bmatrix} e_{out} \\ f_{out} \end{bmatrix} = \frac{1}{AD - BC} \begin{bmatrix} D & -B \\ -C & A \end{bmatrix} \begin{bmatrix} e_{out} \\ f_{out} \end{bmatrix} \tag{3.3}$$

Although the above equation is reasonable mathematically, there might be many

problems in practical system when the inverse problem is done. However, reciprocity theorem can be a great help to solve some thorny measurement problems. The four elements of transduction matrix are not independent, and obey the following relationship:

$$AD - BC = 1 \tag{3.4}$$

This rule is proved in Appendix A.

Now, we see that it takes only three independent elements to describe a system no matter how complex it might be. Substituting Eq. (3.4) into Eq. (3.3), we obtain

$$\begin{bmatrix} e_{in} \\ f_{in} \end{bmatrix} = \begin{bmatrix} D & -B \\ -C & A \end{bmatrix} \begin{bmatrix} e_{out} \\ f_{out} \end{bmatrix} \tag{3.5}$$

According to Eq. (3.5), the four elements A, B, C, D of transduction matrix can be defined as

$$A = f_{in} / f_{out} \mid (e_{out} = 0)$$

$$B = -e_{in} / f_{out} \mid (e_{out} = 0)$$

$$C = -f_{in} / e_{out} \mid (f_{out} = 0)$$

$$D = e_{in} / e_{out} \mid (f_{out} = 0) \tag{3.6}$$

The discussed simultaneous sensing and actuating in the above is achieved using transduction matrix. For an actuator, the output variables can be easily detected from the input variables using Eq. (3.2). Here, the actuator is viewed as a sensor to detect the output variables. Using the transduction matrix, the relationships between the output variables and the input variables are fixed. Therefore, the loading effects of the sensor on the actuator and the loading effects of the actuator on the sensor are both de-coupled from the measurement.

3.1.3 Applications of the Transduction Matrix

Ling and Xie [43] introduced a transduction matrix for the first time when they studied the simultaneous sensing and actuating capability of a PIA (Piezo-ceramic Inertial Actuator), shown in Fig. 3-2. An aluminum plate with a piezoceramic patch bonded to its inner surface is clamped as the cap onto the base of the PIA. A proof mass with an appropriate weight is then fixed at the center of the outer surface of the aluminum plate, which is designed for dynamic testing. The two port model of PIA is shown in Fig. 3-3. Because PIA obeys the three factors of transduction matrix, the relationships between the two mechanical and two electrical variables of PIA are given by:

$$\begin{bmatrix} E \\ I \end{bmatrix} = \begin{bmatrix} P_{11} & P_{12} \\ P_{21} & P_{22} \end{bmatrix} \begin{bmatrix} F \\ V \end{bmatrix} \tag{3.7}$$

From Eq. (3.7), $P_{11} = E/F\big|_{V=0}$ and $P_{21} = I/F\big|_{V=0}$ are the transduction function of voltage to force and the transduction function of current to force respectively when a PIA is clamped on ground; $P_{12} = E/V\big|_{F=0}$ and $P_{22} = I/V\big|_{F=0}$ are the transduction function of voltage to velocity and the transduction function of current to velocity respectively when a PIA is freely suspended. Taking advantages of Eq. (3.7), the PIA was used to measure the mechanical properties of the test structure by measuring the input electrical variables of the PIA.

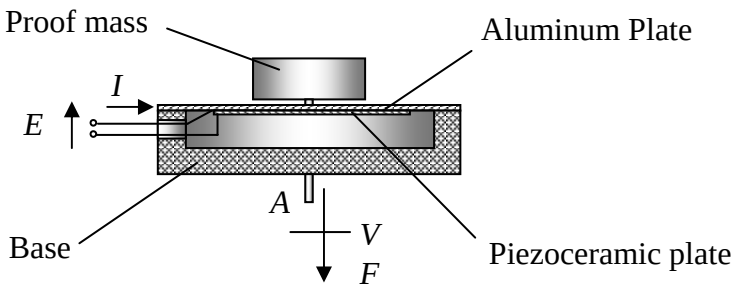

Fig. 3-2 Structure of a piezo-ceramic inertial actuator [43]

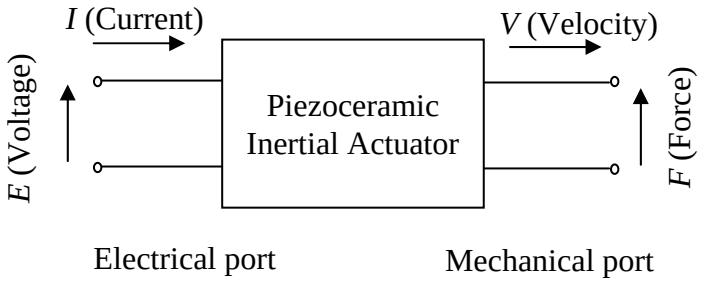

Fig. 3-3 Modeling of system dynamics [43]

Zhang Dong [44] introduced a transduction matrix when he studied the simultaneous sensing and actuating capability of wire bonder, which is shown in Fig. 3-4. A wire bonder consists of an ultrasonic generator, an actuating mechanism (a piezoelectric driver, a concentrator and a bonding capillary) and a bonding interface. The two port model of the actuating mechanism of a wire bonder is shown in Fig. 3-5. Because the actuating mechanism of a wire bonder obeys the three factors of transduction matrix, the relationships between the two mechanical and two electrical variables are given by:

$$\begin{bmatrix} E \\ I \end{bmatrix} = \begin{bmatrix} W_{11} & W_{12} \\ W_{21} & W_{22} \end{bmatrix} \begin{bmatrix} F \\ V \end{bmatrix} \tag{3.8}$$

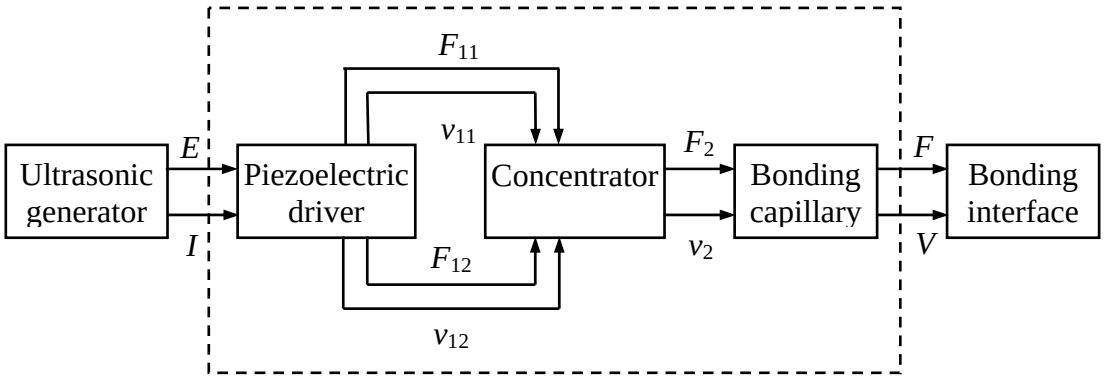

Fig. 3-4 Diagram of the subsystem for bonding in a wire bonder [44]

The definition of the transduction matrix is based on the clamped condition and the free condition, which is similar with Ling and Xie's work. Taking advantages of Eq. (3.8), the detected mechanical variables from the electrical variables were used to study the bonding mechanism and monitor the bonding process.

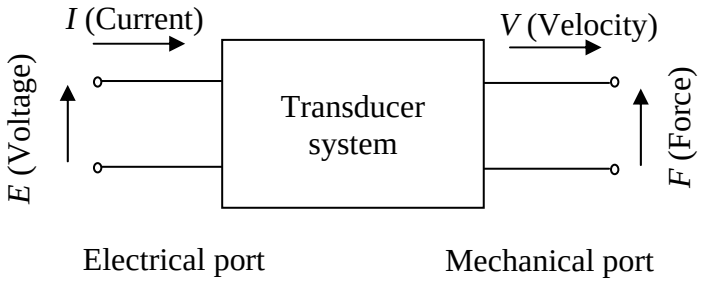

Fig. 3-5 Two port model of transducer system [44]

Luan Jingen [31] introduced a transduction matrix in ultrasonic welding system when he studied the monitoring of ultrasonic welding. Fig. 3-6 is the two port model of the actuating mechanism of an ultrasonic welding system. Form the two port model, the actuating mechanism can be regarded as one system with one input electrical port, which is the input port of the PZT converter, and one output mechanical port, which is the output port of the horn.

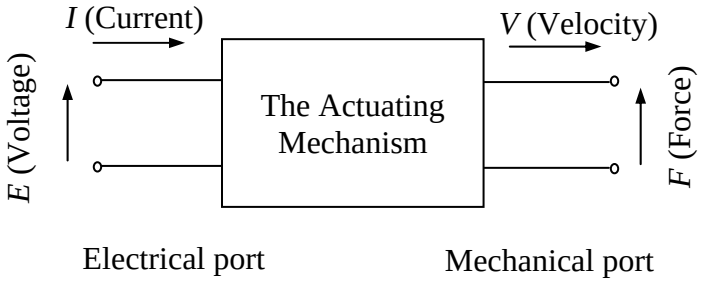

Fig. 3-6 Two port model of the actuating mechanism

Because the converter, the booster and the horn of the actuating mechanism obey the three factors of the transduction matrix, the whole actuating mechanism obeys the

three factors of transduction matrix. In Luan's work, the relationships between the two mechanical and two electrical variables of the actuating mechanism are given by:

$$\begin{bmatrix} E \\ I \end{bmatrix} = \begin{bmatrix} S_{11} & S_{12} \\ S_{21} & S_{22} \end{bmatrix} \begin{bmatrix} F \\ V \end{bmatrix} \tag{3.9}$$

The definition of the transduction matrix is also similar with Ling and Xie's work.

For an ultrasonic welding system, the force and velocity at the output port of the actuating mechanism are very difficult to measure because of the high operating frequency and limited space for installing sensors. However, the voltage and current at the input port are easy to measure. In order to calculate the force and velocity conveniently, we take the inverse expression of Eq. (3.9). The relationships between the input and the output variables can also be written as

$$\begin{bmatrix} F \\ V \end{bmatrix} = \begin{bmatrix} T_{11} & T_{12} \\ T_{21} & T_{22} \end{bmatrix} \begin{bmatrix} E \\ I \end{bmatrix} \tag{3.10}$$

The matrix containing T_{11}, T_{12}, T_{21}, and T_{22} is called the transduction matrix of the actuating mechanism. T_{11}, T_{12}, T_{21}, and T_{22} are the four elements of the transduction matrix.

For the actuating mechanism of the ultrasonic welding system, although it is originally designed as an actuator which converts electrical energy to mechanical energy in order to join plastic parts, it can concurrently be used to detect the output force and velocity, which is also the force and velocity at the joint interface, through measuring the input voltage and current. Therefore, the actuating mechanism can also viewed as a sensor. In other words, the actuating mechanism may act as a sensor as well as an actuator. Hence this technology is simultaneous sensing and actuating.

The actuating mechanism is a reciprocal system, so the four elements of the transduction matrix are related by the following equation

$$T_{11} \times T_{22} - T_{12} \times T_{21} = 1 \tag{3.11}$$

In order to define the four elements of the transduction matrix, the inverse equation between the input variables and the output variables are derived from Eq. (3.5) as

$$\begin{bmatrix} E \\ I \end{bmatrix} = \begin{bmatrix} T_{22} & -T_{12} \\ -T_{21} & T_{11} \end{bmatrix} \begin{bmatrix} F \\ V \end{bmatrix} \tag{3.12}$$

where, voltage E and current I at the input port are known. According to Eq. (3.12), the four elements T_{11}, T_{12}, T_{21}, T_{22} can be expressed as

$$T_{11} = I / V \,|_{F=0}$$

$$T_{12} = -E / V \,|_{F=0}$$

$$T_{21} = -I / F \big|_{V=0}$$

$$T_{22} = E / F \big|_{V=0} \tag{3.13}$$

T_{11} and T_{12} are the transfer function of current to velocity and the minus transfer function of voltage to velocity respectively when the actuating mechanism vibrates freely. T_{21} and T_{22} are the minus transfer function of current to force and the transfer function of voltage to force respectively when the actuating mechanism is clamped on ground.

Since ultrasonic welding only works at one single frequency, T_{11}, T_{12}, T_{21} and T_{22} are constant for a given actuating mechanism, the output variables can be derived from the input variables easily. From the literature review, Luan's result about the transduction matrix was proper. In the next section, a new process of signal processing and data processing for the identification of the transduction matrix is developed.

3.2 Identification of Transduction Matrix of UW Machine

3.2.1 Experimental Setup

In this experiment, a Branson 900 ultrasonic welding system is employed to identify the transduction matrix of the actuating mechanism. For the measurements, a voltage probe system (Tektronix P5205 voltage probe and TM 502A power module) is used to measure the input voltage; a current probe system (Tektronix A6302 current probe and TM 502A amplifier) is used to measure the input current; a LDV (Laser Doppler Vibrometer, Ometron VPI) is used to measure the output velocity. The sensed voltage, current and velocity are filtered with an analog filter (Krohn-Hite Model 3944) first, and then stored with a digital oscilloscope (Nicolet Integra 40). Finally the signals are transferred to a computer for processing.

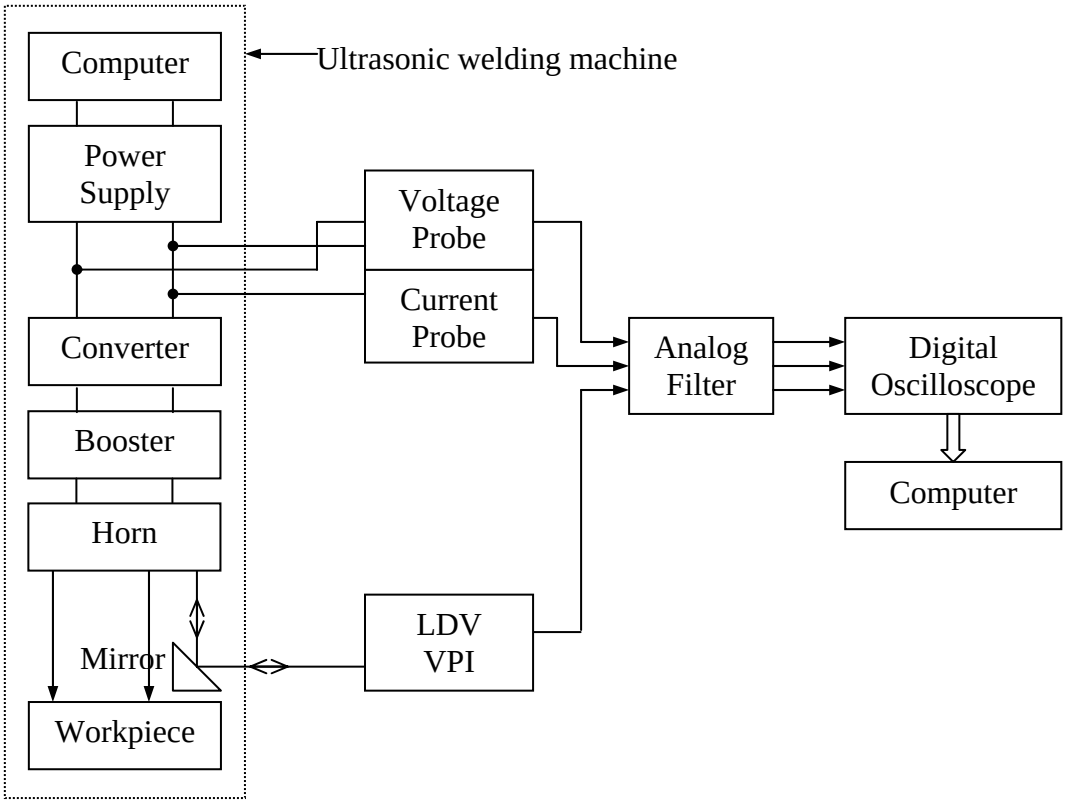

Fig. 3-7 Experimental setup

From this figure, we can see that we get the voltage and current from the output of the power supply. A mirror is mounted at 45 degree with the horizontal plane because the actuating mechanism vibrates up and down vertically and the horizontal laser beam must be reflected to the lower surface of the horn vertically. Thus, the mirror can change the laser beam between vertically and horizontally, and the laser beam can be reflected back to the vibrometer. Fig. 3-8 shows the collection part of the equipment, and Fig. 3-9 shows the signals processing part.

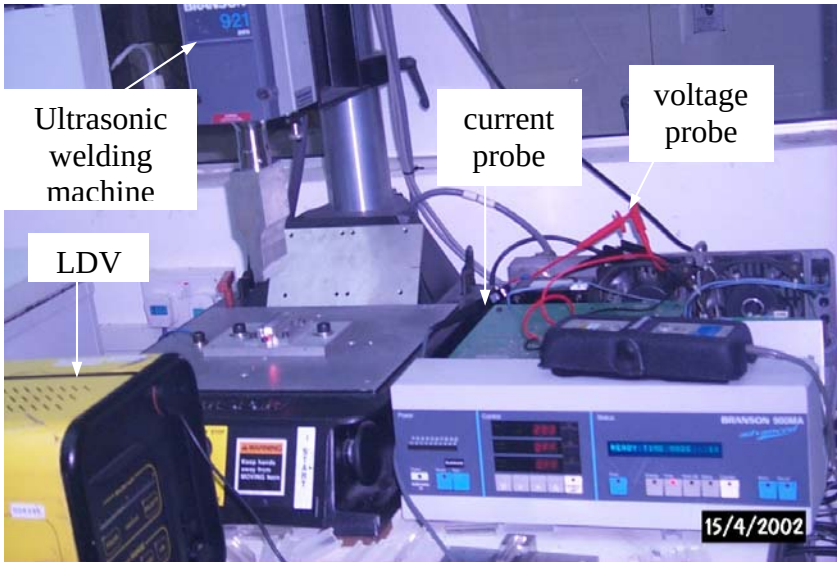

Fig. 3-8 Signals collection part of the equipment

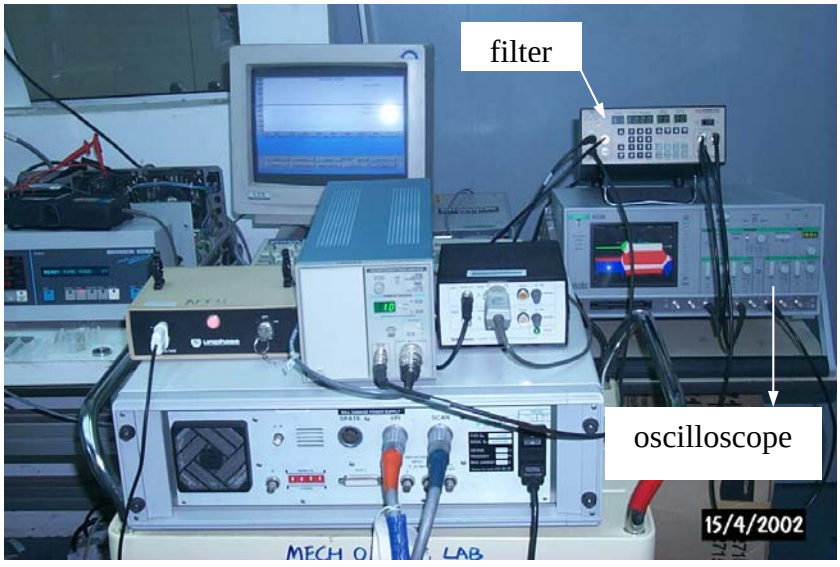

Fig. 3-9 Signals processing part of the equipment

According to Eq. (3.10), we can identify T_{21} and T_{22} from sets of velocity, voltage and current data. However, these signals are not stable in normal welding process because they change so sharply when the energy director melts and collapses quickly. In order to get better results, we had better use more stable signals, so there should be a more stable sinusoidal dynamic force applied to the horn surface. We can weld 'I' samples with no energy director (see Fig. 3-10) using lower vibration amplitudes, so the force will not change much during the welding cycle and keep stable. The reason for using lower vibration amplitude and a short time is that there is little energy dissipated, which will reduce the characteristics of the sample to change. Using the 'I' sample, the experimental settings for identification of T_{21} and T_{22} are listed in Table 3-1, in which the amplitudes are set from 10% to 20% of the maximum amplitude (0.078 mm). For a given amplitude, the same experiments were done 3 times. In total, 33 times experiments were done at 11 different amplitude settings. T_{21} and T_{22} do not change with these settings because they are the properties of the ultrasonic welding system.

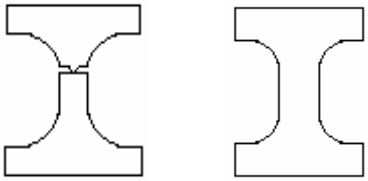

Fig. 3-10 Diagram of a normal AWS sample (left) and an 'I' sample (right)

Table 3-1 Experimental setting

Welding Time (ms)	200
Hold Time (ms)	300
Down Speed (m/s)	0.9
Pressure (psi)	20
Trigger Force (psi)	10
Amplitude (%)	10; 11; 12; 13; 14; 15; 16; 17; 18; 19; 20

The typical collected signals under this setting are shown in Fig. 3-11. From the typical figure, we can see that when the welding process begins, the horn will moves down until it touches the sample. Once it touches the sample, the horn is subjected to an opposed force applied by the sample, so the signals change suddenly and sharply at the beginning part of the whole process. After that, they enter a stable period. At the end part of the process, the voltage and current suddenly change to zero, which also causes the signals not to be stable.

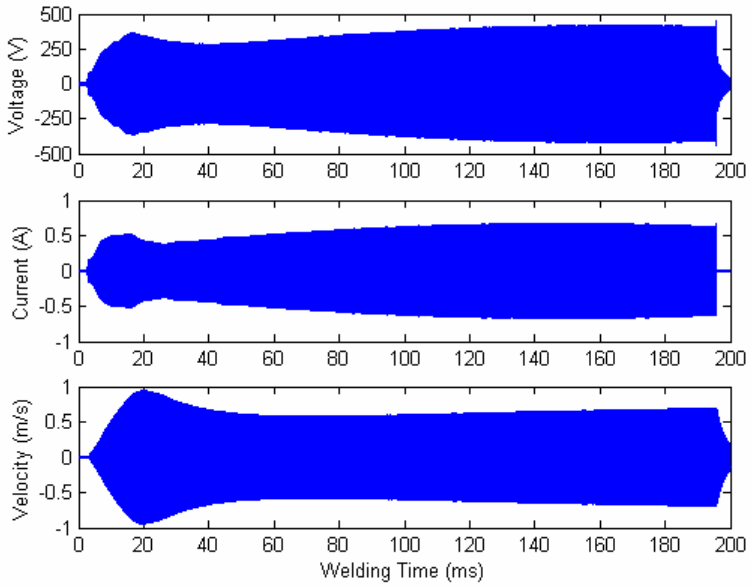

Fig. 3-11 Typical voltage, current and velocity signals

3.2.2 Signal Processing

For the signal processing in this experimental setup, first, a low-pass analog filter is used to avoid aliasing when sampling, and then a band-pass digital filter is designed to filter other frequency signals except 20 kHz signals. Lastly, Hilbert transform is used to get the real time magnitudes and phases of the filtered signals. In the following, the detail of each processing is discussed.

Analog Filter and Sampling

For the measured signals, these are always mixed with some harmonic signals. If the frequencies of the harmonic signals are higher than the half sampling rate, they will cause aliasing when sampling. In order to avoid the aliasing, a low-pass analog filter is needed to filter away the higher frequency signals, but the changes of the signals introduced by the utilized filter cannot affect the evaluation of the transduction matrix.

For analog filters, only Bessel filters have linear phase and all infinite zeros. With the linear phase, the signals of voltage, current and velocity will be delayed by the same time period after Bessel filters, so the transduction matrix will not be influenced. Therefore, we chose the Bessel filter in order to keep phase relationships and prevent pulse distortion.

Fig. 3-12 and Fig. 3-13 show the signals distribution in the frequency domain. From the two figures, the voltage and current have a lot of noise, while the velocity signal mainly focuses at the 20 kHz. According to the voltage and current signals distribution in frequency domain, the cut-off frequency can be put at 60 kHz for the Bessel low-pass filter. According to the Bessel filter definition, the attenuation at the cut-off frequency is 3 dB. From the Bessel approximation, the initial stop band attenuation can be approximated (for any order, up to $\omega/\omega_c = 2$) by the following equation:

$$A_B = 3(\frac{\omega}{\omega_c})^2 dB \tag{3.14}$$

From Eq. (3.14), we can get the attenuation at 20 kHz is $A_B = 3(\frac{20k*2\pi}{60k*2\pi})^2 dB = \frac{1}{3} dB$, so the ratio of the input signal to the output signal is 1/3*1/20=1.0391. The difference

is very little. Because the signals of voltage, current and velocity have the same little attenuation, the transduction matrix will not be influenced by the low-pass filter. Therefore, we can use the order five Bessel 60 kHz low-pass filter to filter the signals. The frequency response of the filter is shown in Fig. 3-14. The distribution of the voltage and current after this filter is shown in Fig. 3-15.

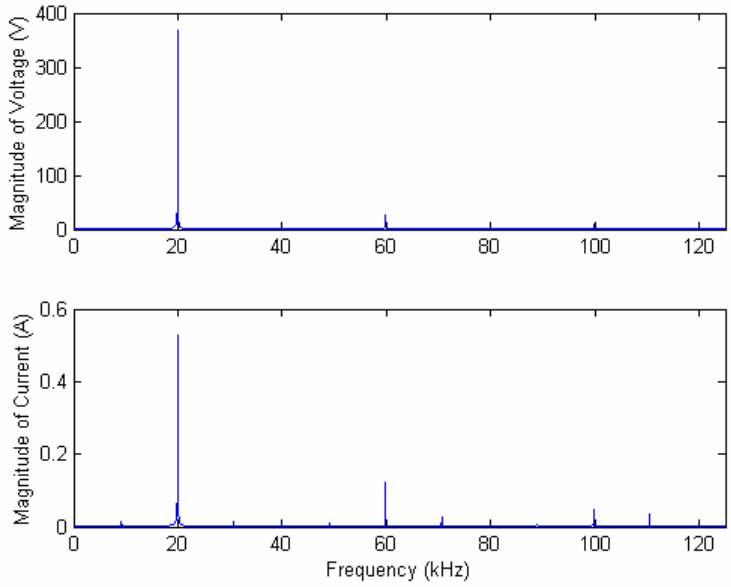

Fig. 3-12 Voltage and current signals distribution in the frequency domain

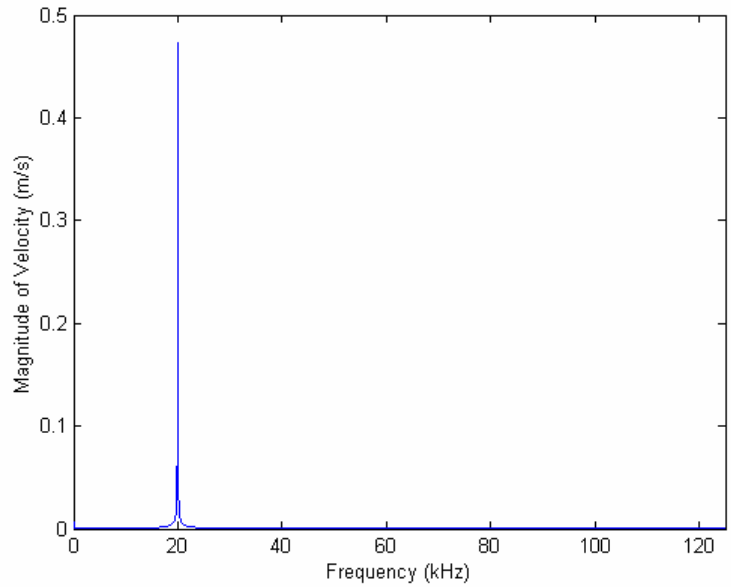

Fig. 3-13 Velocity signal distribution in the frequency domain

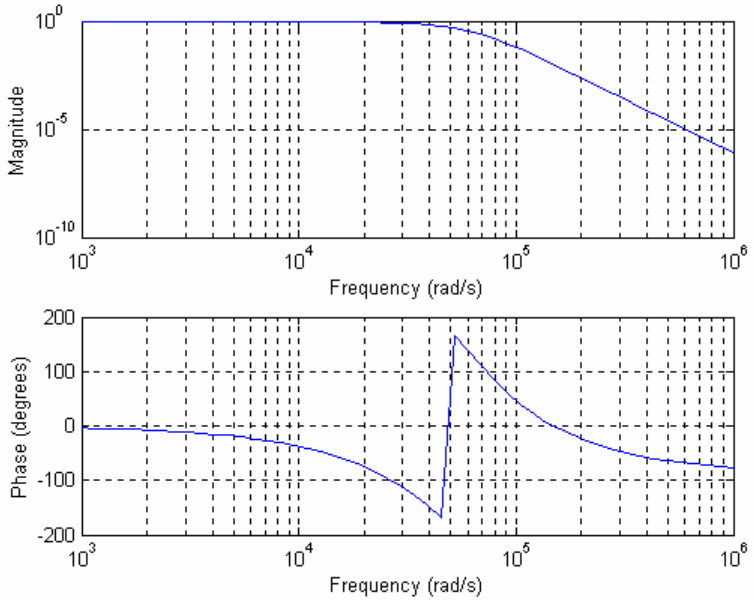

Fig. 3-14 Bessel 60 kHz low-pass filter frequency response (order 5)

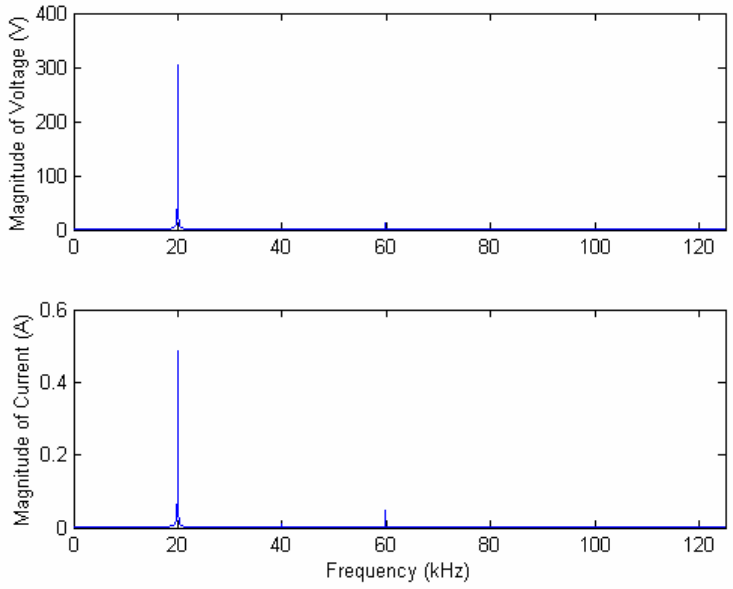

Fig. 3-15 Signal distribution after Bessel low-pass filtering

We need to do the sampling when we collect the data using a digital oscilloscope. According to the Nyquist-Shannon sampling theorem, without loss of information, the sampling frequency f_s must exceed twice the highest signal frequency f_m. The frequency f_m is commonly refered as the Nyquist frequency. Then the signal $f(t)$ can be reconstructed from its sampled value $f(nT)$ by $f(t) = \sum_{n=-\infty}^{\infty} f(nT) \frac{\sin \omega_m (t - nT)}{\omega_m (t - nT)}$, where $T = 1/f_s$, $\omega_m = 2\pi f_m$.

For this application, the Nyquist frequency is 60 kHz because we use the 60 kHz low-pass filter, so the sampling frequency should be $f_s > 2 f_m = 2 * 60kHz = 120kHz$. Normally, the sampling frequency is often chosen four times or five times more than the Nyquist frequency to get better results. From the digital oscilloscope, we choose a sweep length of 50000, so the sampling frequency is equal to sweep length/welding time=50000/200 ms=250 kHz.

Digital Filtering

Digital filters have much better response than analog filters. For this processing, only 20 kHz signals are needed, so it is very necessary to use a digital filter to filter other frequency signals. There are two types of digital filters: FIR (finite impulse response) and IIR (infinite impulse response). FIR have feed-forward coefficients, no feed-back coefficients, while IIR have feed-forward coefficients and feed-back coefficients. Because FIR filters are always stable and can be designed with exact linear phase, a FIR filter is chosen for this processing. For FIR filters, the impulse response [55] is:

$$y[n] = \sum_{i=0}^{N} b_i x[n-i] \tag{3.15}$$

where x[n] is the current input, x[n-1], x[n-2], ... are the past inputs; y[n] is the current output; b_i is the coefficient of FIR filter.

For this processing, we only want 20 kHz signals, so a band-pass filter is needed. However, it is very difficult to design such a filter because the frequency 20 kHz is so high. There are three types of FIR filters mainly: Equiripple, Least-Squares and Windows, in which Equiripple filter has the best performance for this application. The pass band is set from 10 kHz to 30 kHz, and the cut-off frequencies are 5 kHz and 35 kHz. The attenuation at the cut-off frequencies is –60 dB, and the attenuation at pass band is nearly 0 dB. For the better response, we choose the order N=150, which is stable. The design result of coefficients b_i is shown in Fig. 3-16.

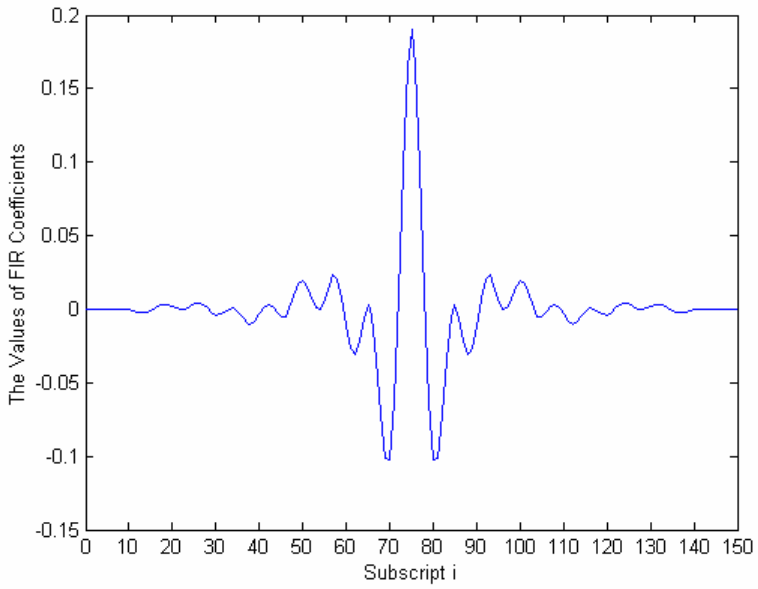

Fig. 3-16 Values of b_i

From the values of b_i, we can get the frequency response (Fig. 3-17) and signal distribution after the digital filter (Fig. 3-18). From the filtered signals, we can see the band-pass Equiripple has good performance, and it nearly cut off all the harmonic noise. Therefore, the filtered signals can be used to evaluate the transduction matrix.

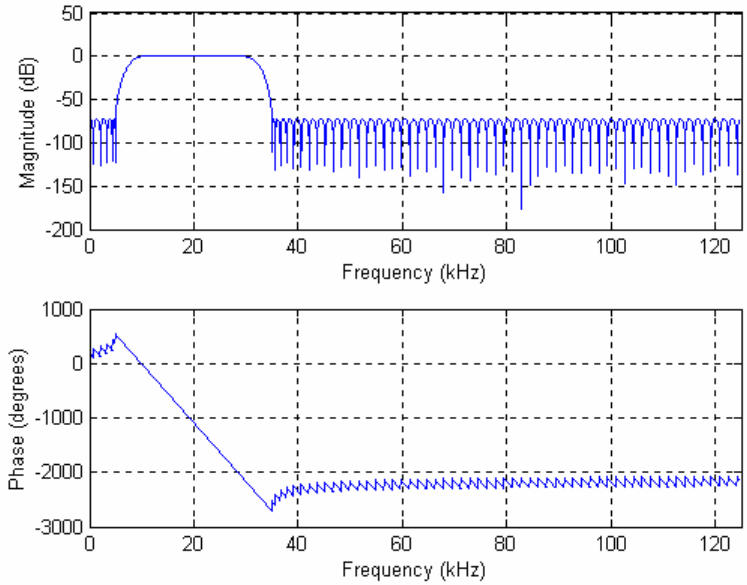

Fig. 3-17 Equiripple band-pass filter frequency response

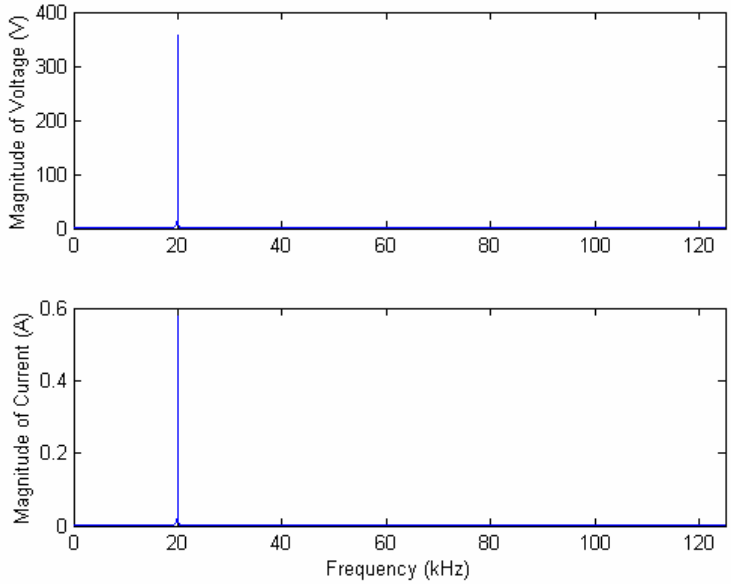

Fig. 3-18 Signal distribution in frequency domain after digital filter

Hilbert Transform

For the filtered signals, we cannot use them to calculate the transduction matrix directly because there are many zero values in the signals. Normally, the FFT (Fast Fourier Transform) or the Hilbert Transform can be used to get the magnitudes and phases of the signals. Because the Hilbert transform is a real time transform from time domain to time domain, we choose the Hilbert transform rather than the FFT.

The Hilbert transform of a real-valued function $x(t)$ extending over the range $-\infty < t < \infty$ is a real-valued functional $\tilde{x}(t)$ defined by [57, 58]

$$\tilde{x}(t) = H[x(t)] = \int_{-\infty}^{\infty} \frac{x(u)}{\pi(t-u)} du \tag{3.16}$$

Thus $\tilde{x}(t)$ is the convolution integral of $x(t)$ and $(1/\pi t)$, written as

$$\tilde{x}(t) = x(t) * (1/\pi t) \tag{3.17}$$

The complex signal $z(t)$ whose imaginary part is the Hilbert transform of the real part is called the analytic signal. We write it as

$$z(t) = x(t) + j\tilde{x}(t) = A(t)e^{j\theta(t)} \tag{3.18}$$

where $A(t)$ is called the envelop signal of $x(t)$, and $\theta(t)$ is called the instantaneous phase signal of $x(t)$. In terms of $x(t)$ and $\tilde{x}(t)$, it is clear that

$$A(t) = [x^2(t) + \tilde{x}^2(t)]^{1/2} \tag{3.19}$$

$$\theta(t) = \tan^{-1}\left[\frac{\tilde{x}(t)}{x(t)}\right] \tag{3.20}$$

For the digital signals, $t = nT$, $T = 1/f = 1/250kHz = 0.004ms$, n is sampling point.

$$\tilde{x}_n = H[x_n] \tag{3.21}$$

$$z_n = x_n + j\tilde{x}_n = A_n e^{j\theta_n} \tag{3.22}$$

In the following, 2 ms signals (Fig. 3-19) are extracted from the voltage, current, and velocity curves as an example to analyze using Hilbert Transform.

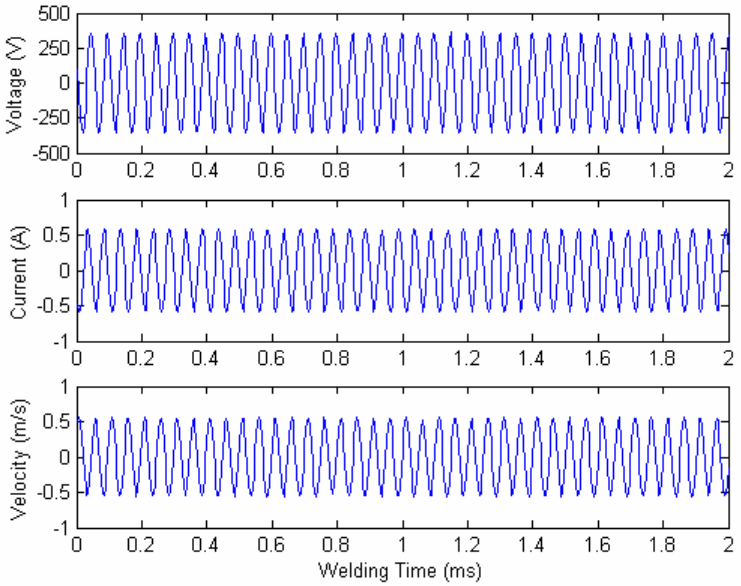

Fig. 3-19 Extracted signals for analyzing amplitude and phase

A program has been written to do the Hilbert transform. Fig. 3-20 is the transform result of the voltage (the same for the current and the velocity signal). From the figure, we can see the magnitude is almost constant except that there are some oscillations near the start part and the end part of the signal. The oscillation is a defect of the Hilbert transform, and we cannot overcome it. However, for the whole welding process, we don't use the start part and the end part for calculation, so it will not influence the transduction matrix. From Fig. 3-20, we also can see that the phase is not constant. However, if we calculate the differences among the voltage, the current and the velocity, we can get the phase differences. The upper part in Fig. 3-21 shows the phase difference between voltage and velocity. If the minus values are added 2π, we

can get the lower part in Fig. 3-21. It is shown that the difference is almost constant. The result is same for the difference between current and velocity. Hence, the transduction matrix can be calculated based on this.

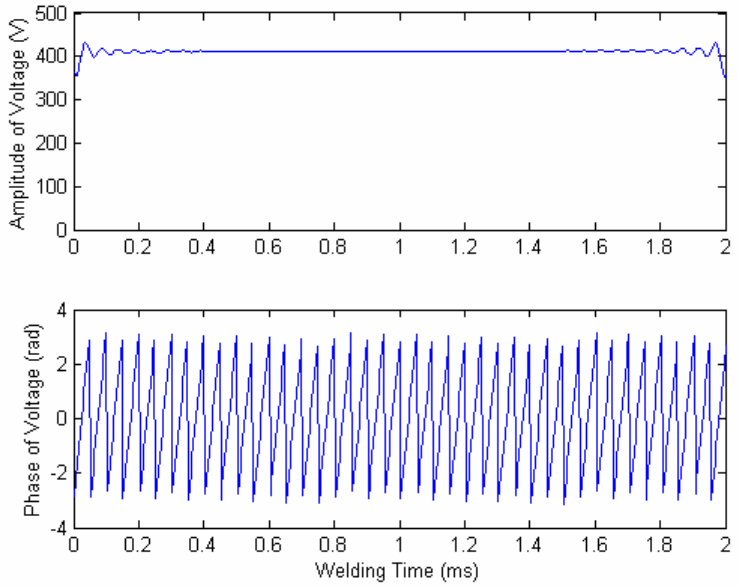

Fig. 3-20 Hilbert transform of the extracted voltage signal

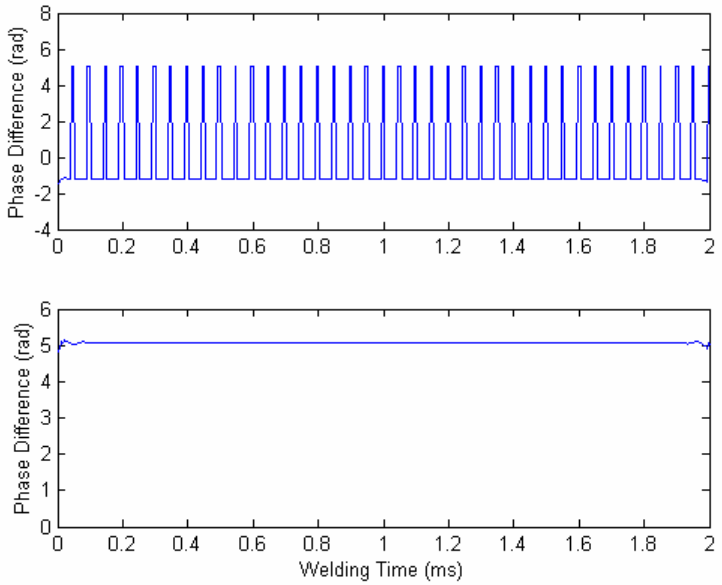

Fig. 3-21 Phase difference between voltage and velocity

3.2.3 Calculation of T_{21} and T_{22} under 'I' Samples Process

Because there are two transient periods in the beginning of a welding process and at the end of a welding process, and also because of the oscillation induced by Hilbert Transform, they will cause errors if we calculate the transduction matrix using the voltage, current, and velocity at these two transient periods. Therefore, we extract the stable signals from 40 ms to 190 ms to calculate T_{21} and T_{22}.

According to Eq. (3.10), the two independent variables E and I and one dependent variable V have the linear relationship as:

$$V = T_{21}E + T_{22}I = f(E,I) \tag{3.23}$$

For the given data set (E_1,I_1,V_1), (E_2,I_2,V_2), … , (E_n,I_n,V_n), where $n \geq 3$, the best fitting curve $f(E_i,I_i)$ has the least square error, i.e.,

$$\prod = \sum_{i=1}^{n}[V_i - f(E_i,I_i)]^2 = \sum_{i=1}^{n}[V_i - (T_{21}E_i + T_{22}I_i)]^2 = \min. \tag{3.24}$$

To obtain the least square error, the unknown coefficients T_{21} and T_{22} must yield zero first derivatives:

$$\begin{cases} \dfrac{\partial \prod}{\partial T_{21}} = 2\sum_{i=1}^{n} E_i[V_i - (T_{21}E_i + T_{22}I_i)] = 0 \\ \dfrac{\partial \prod}{\partial T_{22}} = 2\sum_{i=1}^{n} I_i[V_i - (T_{21}E_i + T_{22}I_i)] = 0 \end{cases} \tag{3.25}$$

Expanding the above equations, we have

$$\begin{cases} \sum_{i=1}^{n} E_iV_i = T_{21}\sum_{i=1}^{n} E_i^{\,2} + T_{22}\sum_{i=1}^{n} E_iI_i \\ \sum_{i=1}^{n} I_iV_i = T_{21}\sum_{i=1}^{n} E_iI_i + T_{22}\sum_{i=1}^{n} I_i^{\,2} \end{cases} \tag{3.26}$$

The unknown coefficients T_{21} and T_{22} can hence be obtained by solving the above linear equations. Appendix B proves this method.

For the exacted signals of each amplitude level from 10% to 20%, each process has 37500 sampling points at the 250 kHz sampling rate, and for each process, it will be $\sum_{i=1}^{n} E_i V_i = \sum_{i=10001}^{47500} E_i V_i$, $\sum_{i=1}^{n} E_i^{\,2} = \sum_{i=10001}^{47500} E_i^{\,2}$, $\sum_{i=1}^{n} E_i I_i = \sum_{i=10001}^{47500} E_i I_i$, $\sum_{i=1}^{n} I_i V_i = \sum_{i=10001}^{47500} I_i V_i$, $\sum_{i=1}^{n} I_i^{\,2} = \sum_{i=10001}^{47500} I_i^{\,2}$, where i is the sampling point. For the more exact results, we combine all the signals at all amplitude levels together. From Eq. (3.26), the final results T_{21} and T_{22} are:

$$T_{21} = -2.0564 \times 10^{-3} - 2.6513 \times 10^{-3} i$$

$$T_{22} = 1.0455 - 0.7329 i$$

3.2.4 Calculation of T_{11} and T_{12} under an Unloaded Condition

The unloaded condition means the actuating mechanism vibrates freely without any loading. Under this condition, the force F is equal to zero. According to Eq. (3.13), we can evaluate T_{11} and T_{12} by measuring the voltage, the current and the velocity under this condition. For the Branson 900 system, the unload condition is achieved when the system works at the 'TEST' model (Branson User Manual: WPC-2 Weld Profile Controller). In order to get better results, the maximum record length 500,000 of the digital oscilloscope is selected. The sampling rate is also 250 kHz, so we can collect two-second signals by setting a trigger. Fig. 3-22 shows the collected voltage, current and velocity signals.

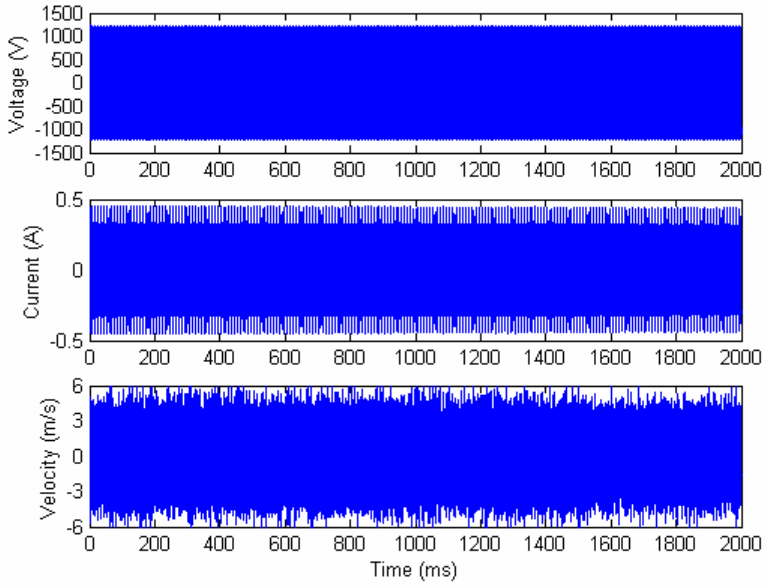

Fig. 3-22 Signals of an unloaded condition

From this figure, we can see that the voltage keeps constant in the whole process, and the current almost keeps constant. The velocity is not stable because the system is not steady enough, and caused a lot of noise. Under the unloaded condition, the values of voltage, current and velocity do not vary with time, so it had better for us to use FFT to get the amplitude and the phase. Fig. 3-23 and Fig. 3-24 show the three signals in the frequency domain. We can calculate T_{11} and T_{12} from the values of the three signals at 20 kHz as

$$T_{11} = \left.\frac{I(f = 20kHz)}{V(f = 20kHz)}\right|_{F=0} = \frac{-0.2373 + 0.1974i}{3.4337 + 0.0846i} = -0.0676 + 0.0591i$$

$$T_{12} = -\left.\frac{E(f = 20kHz)}{V(f = 20kHz)}\right|_{F=0} = -\frac{-6.2349 \times 10^2 + 9.1979 \times 10^2 i}{3.4337 + 0.0846i}$$

$$= 1.7487 \times 10^2 - 2.7218 \times 10^2 i$$

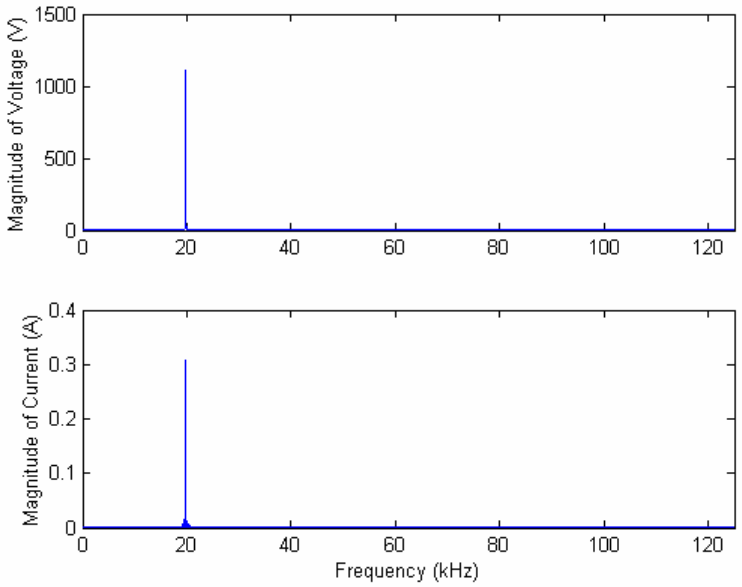

Fig. 3-23 Frequency distribution of voltage and current

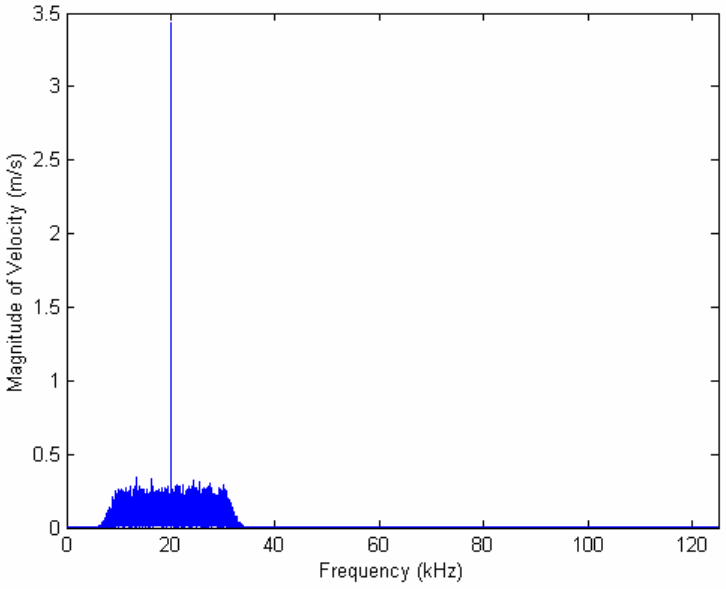

Fig. 3-24 Frequency distribution of velocity

3.3 Measurement of the Force and Velocity

From the values of the transduction matrix, we can calculate the determinant of the transduction matrix as

$$T = T_{11}T_{22} - T_{12}T_{21} = 1.0539 + 0.0153i$$

This value is nearly equal to one, having very little error, which confirms that the proposed measurement method is proper. According to the reciprocity theorem, the determinant T should be equal to one. For this case, there are many reasons that cause this error, such as the inevitable equipment error caused by the equipment and the environment, the little temperature rise of the actuating mechanism during welding process, the unstable velocity signal when unloading, etc.

In order to validate the evaluated transduction matrix, the transduction matrix will be used to detect the velocity during the welding processes. The discrepancy between the detected velocity and the measured velocity can be an indicator of the measurement method. The output velocity of the actuating mechanism during the welding process is calculated using Eq. (3.10). In the following, three cases under different vibration amplitudes are selected to study the discrepancy between the detected velocity and the measured velocity using LDV. For case 1, the vibration amplitude is set as 13%. The sensed voltage and current is shown in Fig. 3-25. The amplitudes of the detected velocity and the measured velocity are shown in Fig. 3-26. For case 2, the vibration amplitude is set as 16%. The sensed voltage and current is shown in Fig. 3-27. The amplitudes of the detected velocity and the measured velocity are shown in Fig. 3-28. For case 3, the vibration amplitude is set as 18%. The sensed voltage and current is shown in Fig. 3-29. The amplitudes of the detected velocity and the measured velocity

are shown in Fig. 3-30. In the velocity figures, the solid lines are the measured velocity, and the dash-dot lines are the detected velocity using the transduction matrix.

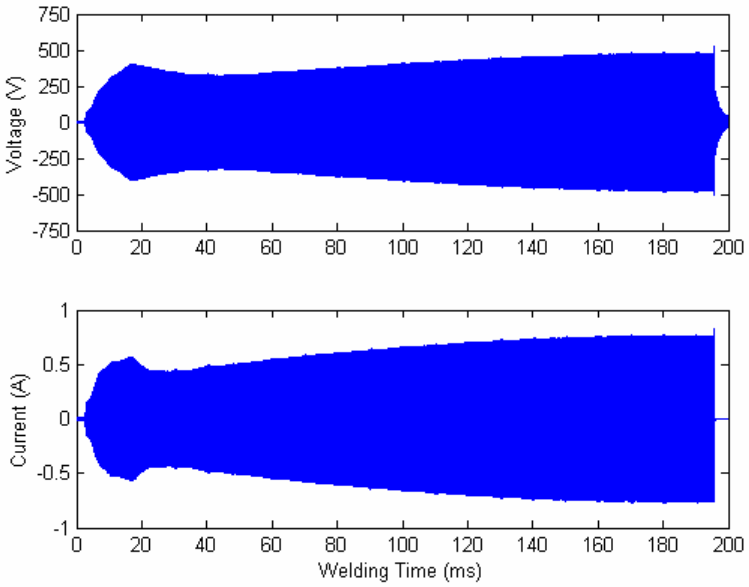

Fig. 3-25 Voltage and current for case 1

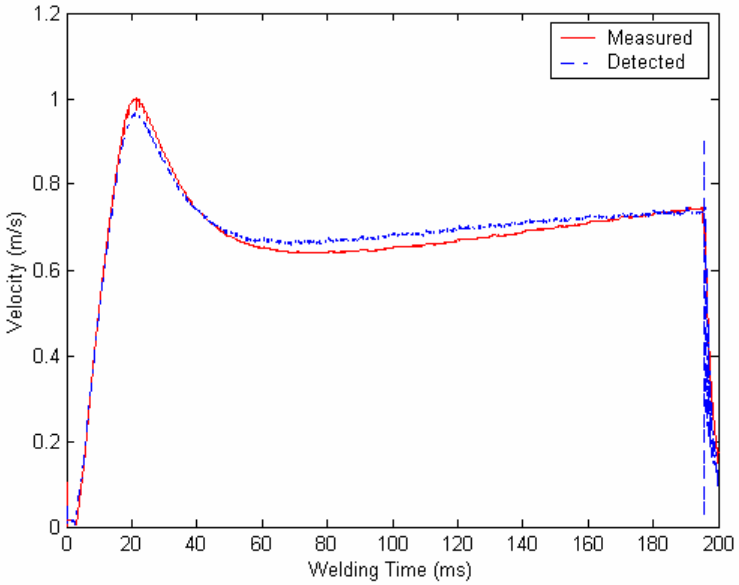

Fig. 3-26 Amplitudes of detected velocity and measured velocity for case 1

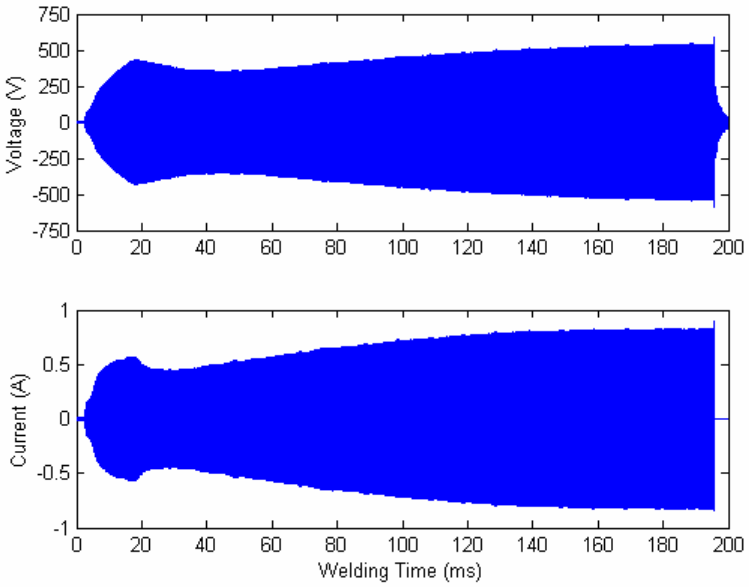

Fig. 3-27 Voltage and current for case 2

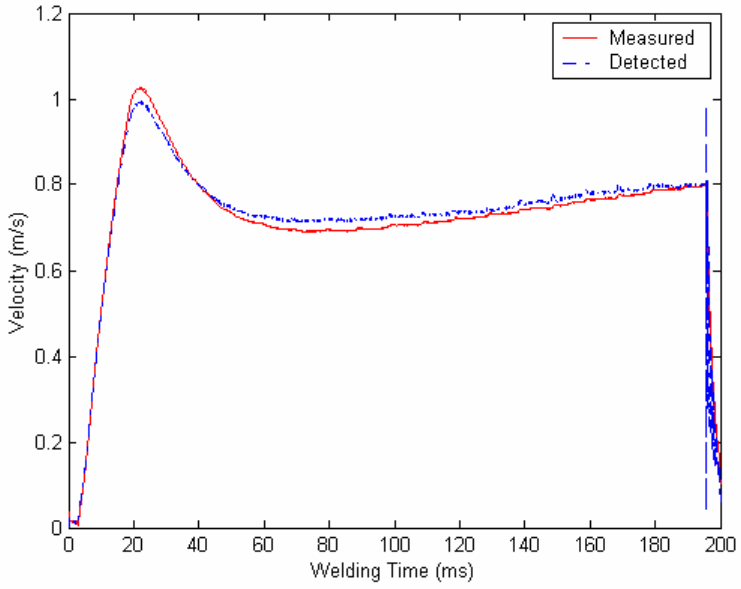

Fig. 3-28 Amplitudes of detected velocity and measured velocity for case 2

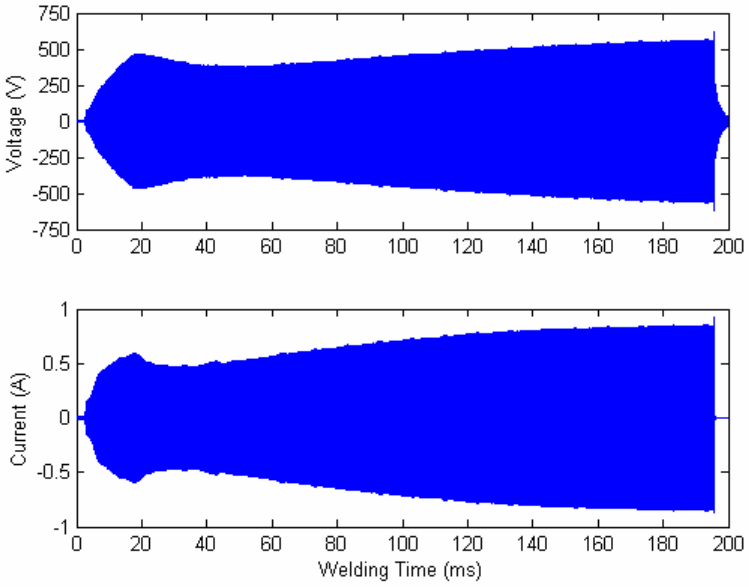

Fig. 3-29 Voltage and current for case 3

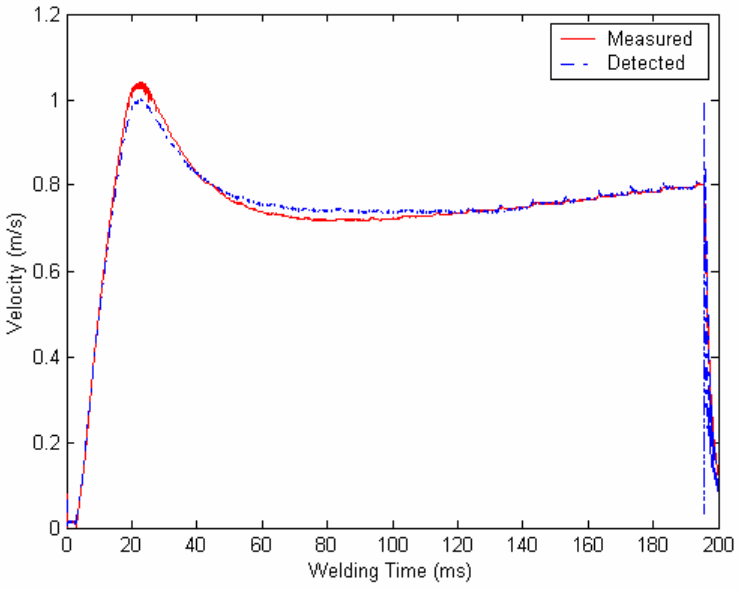

Fig. 3-30 Amplitudes of detected velocity and measured velocity for case 3

When the welding process begins, both the detected velocity and the measured velocity begin to increase sharply because the horn is subjected to an opposed force applied by the workpiece. After that, they enter a more stable period. When the

welding process ends, the voltage and current disappear suddenly, which cause the sudden change for the detected velocity; while, for the measured velocity, it decreases smoothly. The little difference between the detected velocity and the measured velocity will not affect the usage of detected velocity for the whole welding process.

The discrepancies between the detected velocity and the measured velocity are very small, which gives us full confidence to use the transduction function. Since there is no force sensor which can measure the dynamic force in so high a frequency, there is no method to determine the force. However, based on the small errors of the velocity and the determinant, we can calculate the force using the transduction matrix. Fig. 3-31, Fig. 3-32 and Fig. 3-33 show the amplitudes of the detected force during the three welding processes respectively. The detected force changes similarly with the detected velocity, which are also the force and the velocity at the joint interface. The drop of the force at about 20 ms is due to the yielding of the material. After yielding, the force begins to increase again with the increase of the joint area.

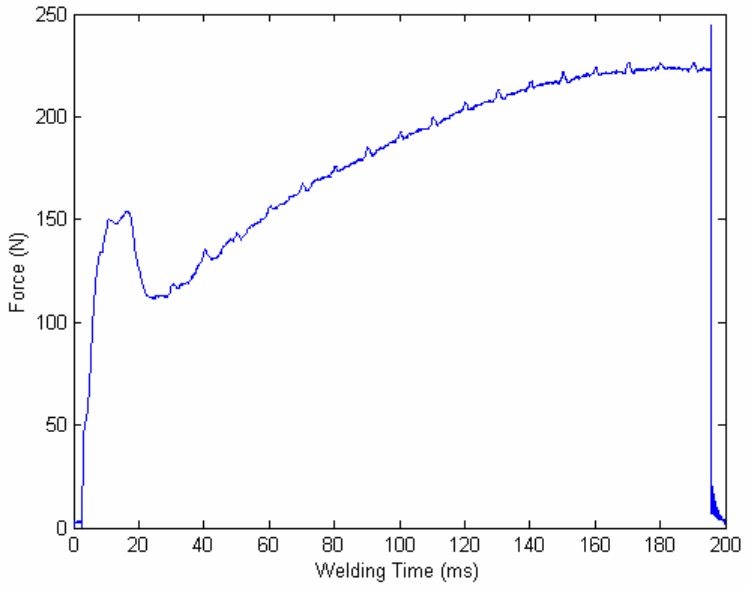

Fig. 3-31 Amplitude of the detected force for case 1

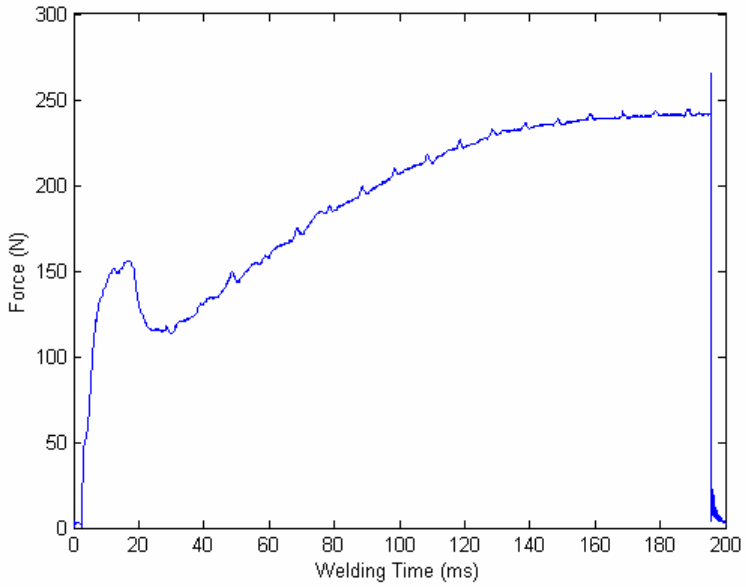

Fig. 3-32 Amplitude of the detected force for case 2

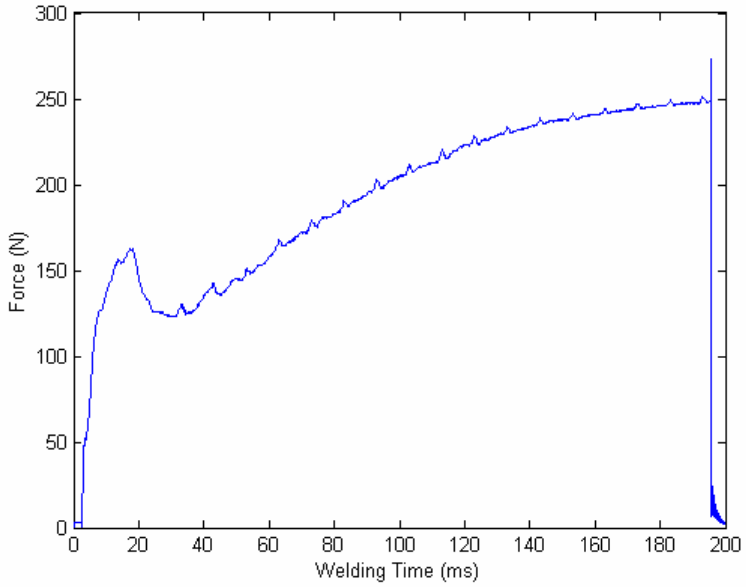

Fig. 3-33 Amplitude of the detected force for case 3

3.4 Detection of Mechanical Impedance

Based on Eq. (3.22), we can calculate the complex representation at each sampling point for a real sampled signal. After converting the sensed voltage and current into complex representation, we can obtain the electrical impedance for a time varying system. The sensed voltage and current can be represented in an analytical signal as:

$$E(t) = |E(t)|e^{j\theta_E(t)} \tag{3.27}$$

$$I(t) = |I(t)|e^{j\theta_I(t)} \tag{3.28}$$

Then the electrical impedance is

$$Z_e(t) = \frac{E(t)}{I(t)} = \frac{|E(t)|}{|I(t)|} e^{j[\theta_E(t)-\theta_I(t)]} = |Z_e(t)|e^{j\varphi(t)} \tag{3.29}$$

where $|Z_e(t)|$ is the amplitude of the electrical impedance, and $\varphi(t)$ is its corresponding phase.

This is the fundamental principle. However, in practice, there are some situations that must be taken into account. As we know, the capacitance and inductance varies with frequency. For a signal including several harmonic components, the instantaneous frequency of an analytic signal is neither of any component frequency. Therefore, we can only obtain time varying impedance at a certain frequency.

From the last section, the mechanical force and velocity can be detected from the electrical voltage and current. The mechanical impedance should also be calculated from the analytic signals of the force and velocity. As the variables of the actuating mechanism are all analytic signals, the force and velocity are both in complex form. It is convenient to complete the dividing operation and get the mechanical impedance.

The detected force and velocity can be represented as:

$$F(t) = |F(t)|e^{j\theta_F(t)} \tag{3.30}$$

$$V(t) = |V(t)|e^{j\theta_V(t)} \tag{3.31}$$

The mechanical impedance can be derived as

$$Z_m(t) = \frac{F(t)}{V(t)} = \frac{|F(t)|}{|V(t)|}e^{j[\theta_F(t)-\theta_V(t)]} = |Z_m(t)|e^{j\theta(t)} \tag{3.32}$$

where, $|Z_m(t)|$ is the amplitude of the mechanical impedance and $\varphi(t)$ is its corresponding phase.

Rearranging Eq. (3.10) gives

$$\frac{F}{V} = \frac{T_{11}E + T_{12}I}{T_{21}E + T_{22}I} = \frac{T_{11}\dfrac{E}{I} + T_{12}}{T_{21}\dfrac{E}{I} + T_{22}} \tag{3.33}$$

Thus, we get the relationship between input electrical impedance and the output mechanical impedance (which is also the mechanical impedance at joint interface) as:

$$Z_m = \frac{T_{11}Z_e + T_{12}}{T_{21}Z_e + T_{22}} \tag{3.34}$$

$$Z_e = \frac{T_{22}Z_m - T_{12}}{-T_{21}Z_m + T_{11}} \tag{3.35}$$

Through Eq. (3.34) and Eq. (3.35), the mechanical impedance at the output port of the actuating mechanism is correlated to its input electrical impedance.

In the following, the mechanical impedance will be detected from the electrical impedance for the above three cases in last section. The electrical impedances are shown in Fig. 3-34, Fig. 3-36 and Fig. 3-38 respectively. The corresponding

mechanical impedances are shown in Fig. 3-35, Fig. 3-37 and Fig. 3-39. At the beginning and the end of the welding process, the electrical impedances and the mechanical impedances are very big due to the dividing operation caused by the small current. The drops of the mechanical impedances are due to the yielding of the material. After the yielding, the mechanical impedances begin to increase.

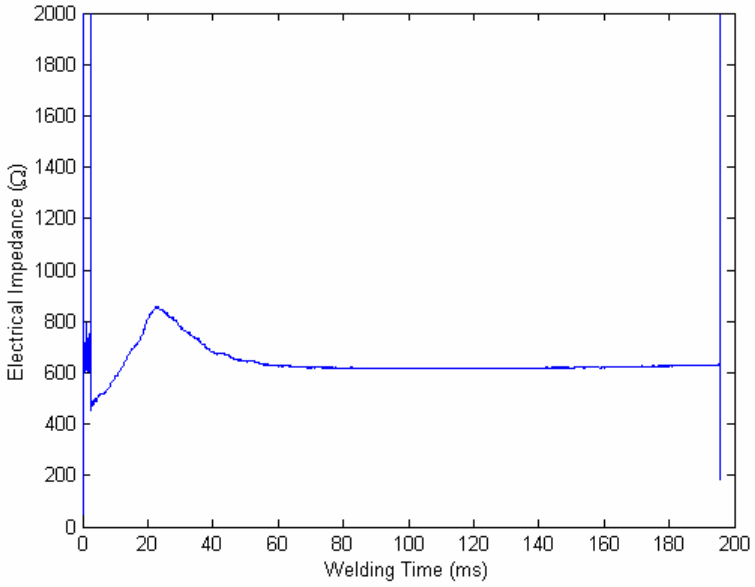

Fig. 3-34 Electrical impedance for case 1

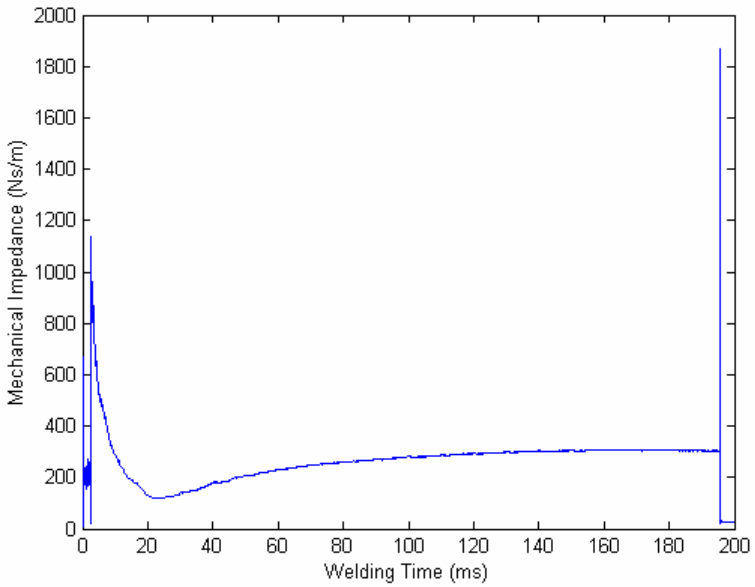

Fig. 3-35 Mechanical impedance for case 1

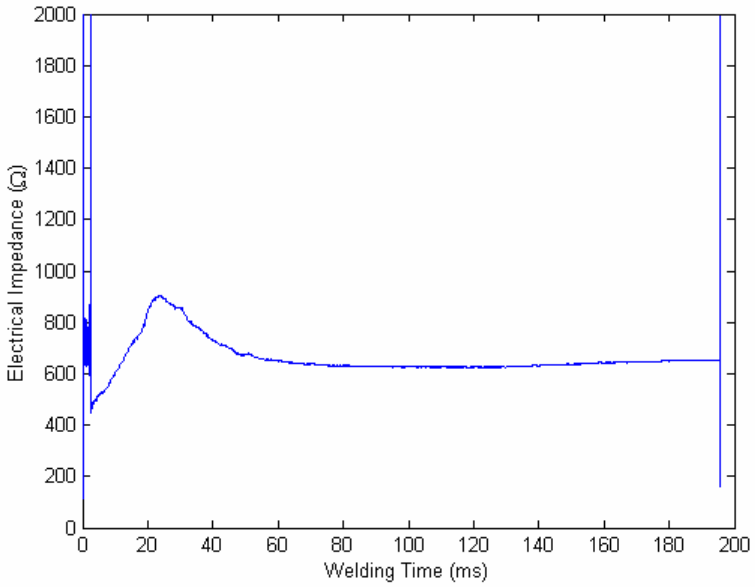

Fig. 3-36 Electrical impedance for case 2

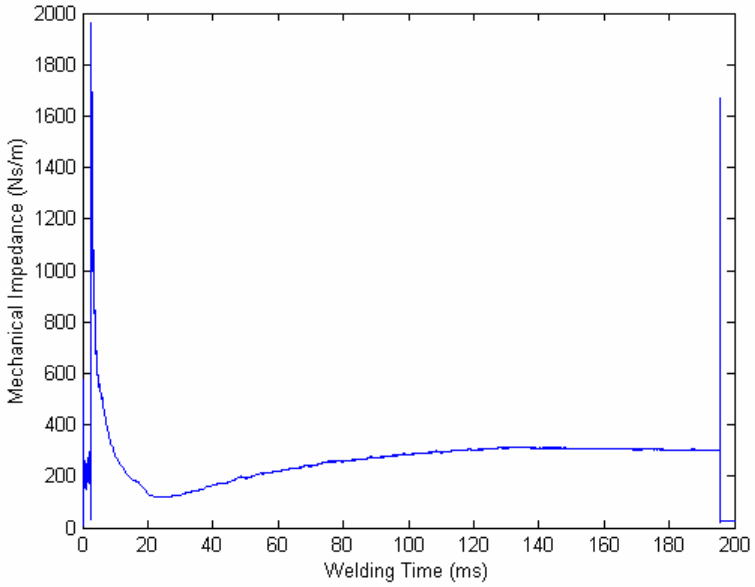

Fig. 3-37 Mechanical impedance for case 2

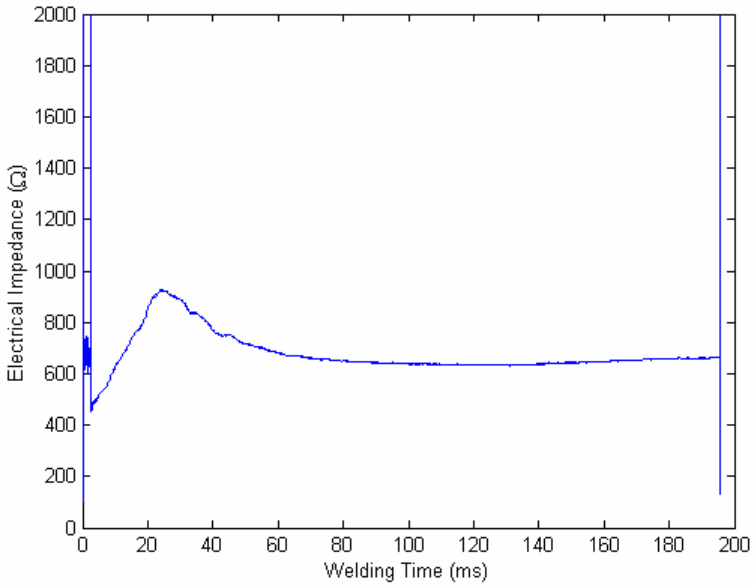

Fig. 3-38 Electrical impedance for case 3

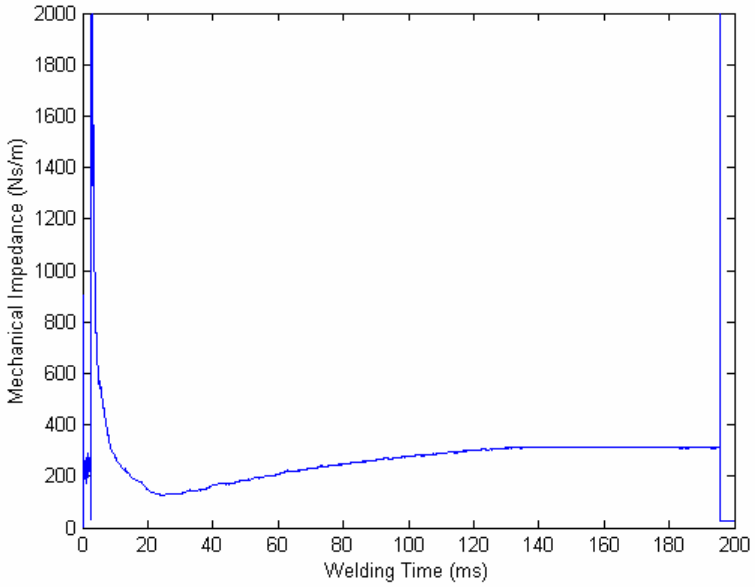

Fig. 3-39 Mechanical impedance for case 3

3.5 Equivalent Circuit of the Actuating Mechanism

For ultrasonic welding system, the converter only works at its thickness direction, so the PZT converter can be viewed as a one-dimensional model with a two-layer piezoelectric transformer [59-66]. The 1D model is based on one-dimensional wave propagation along one axis, and it is assumed that the electric field intensity and the electric displacement are in the same direction. The converter only has load at one side when working in ultrasonic welding system. Based on the 1D model, the converter can be modeled as a simple equivalent network, shown in Fig. 3-40. In this circuit, E and I are the input voltage and current; F_I and V_I are the output voltage and current. The parameters of the circuit are defined in Appendix C.

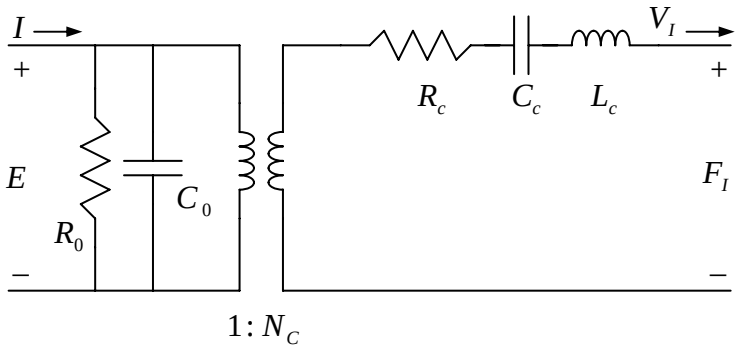

Fig. 3-40 Equivalent circuit of the converter [59]

Using Laplace transform, the equivalent circuit can be expressed in s domain. Based on the impedance concept, we can define

$$Z_c(s) = R_c + \frac{1}{sC_c} + sL_c \tag{3.36}$$

$$Z_0(s) = R_0 \,||\, \frac{1}{sC_0} = \frac{R_0}{sC_0R_0 + 1} \tag{3.37}$$

The relationships between the input electrical variables and the output mechanical variables of the converter are expressed by matrix as

$$\begin{bmatrix} F_I(s) \\ V_I(s) \end{bmatrix} = \begin{bmatrix} N_c - \dfrac{Z_c(s)}{N_c Z_0(s)} & \dfrac{Z_c(s)}{N_c} \\ -\dfrac{1}{N_c Z_0(s)} & \dfrac{1}{N_c} \end{bmatrix} \begin{bmatrix} E(s) \\ I(s) \end{bmatrix} = T_C \begin{bmatrix} E(s) \\ I(s) \end{bmatrix} \tag{3.38}$$

As we see, the determinant of the matrix is equal to one.

Both the booster and the horn are mechanical amplifiers (or attenuators) for the vibration amplitude because the vibration is transmitted from the converter to the horn. The increase (or decrease) of vibration amplitude is inversely proportional to the increase (or decrease) in cross-sectional area. In practice, the increase (or decrease) of vibration amplitude is achieved through the periodic deformation of the input port and the output port. There is a node between the input port and the output port. The node is a static point for the booster and the horn, which is the property of the device. The booster and horn can be divided into upper part and lower part from the node.

Because the booster and the horn only work at one single frequency and vibrate at one direction, so the upper part and the lower part of the booster and the horn can be simplified as one degree of freedom mass-spring-damping model [68], in which a mass is connected in parallel with a Kelvin model. Since the equivalences between mechanical force F and electrical voltage E, and, between mechanical velocity V and electrical current I, have been established, the mass-spring-damping model is equivalent to one resistor, one capacitor and one inductor in series. For the equivalent circuit of the booster, the mechanical amplifier (or attenuator) can be equivalent to an electrical transformer. The equivalent circuit of the booster is shown in Fig. 3-41.

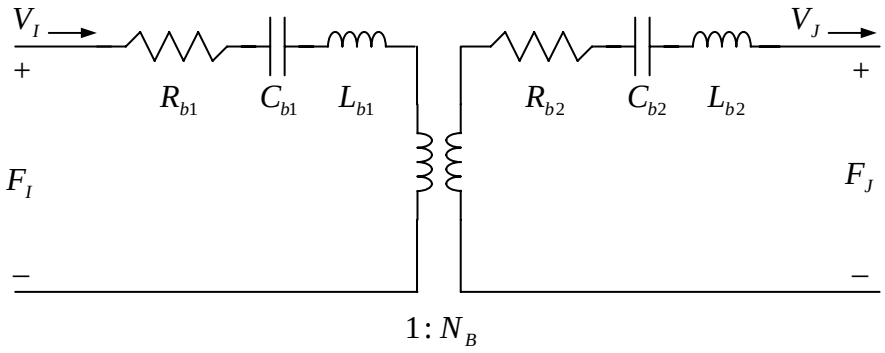

Fig. 3-41 Equivalent circuit of the booster

In this equivalent circuit, F_I and V_I are the input voltage and current, F_J and V_J are the output voltage and current. After Laplace transform, based on the impedance concept, we can define

$$Z_{b1}(s) = R_{b1} + \frac{1}{sC_{b1}} + sL_{b1} \tag{3.39}$$

$$Z_{b2}(s) = R_{b2} + \frac{1}{sC_{b2}} + sL_{b2} \tag{3.40}$$

The relationships between the input electrical variables and the output mechanical variables of the booster are expressed by matrix as

$$\begin{bmatrix} F_J(s) \\ V_J(s) \end{bmatrix} = \begin{bmatrix} N_B & -N_B Z_{b1}(s) - Z_{b2}(s)/N_B \\ 0 & 1/N_B \end{bmatrix} \begin{bmatrix} F_I(s) \\ V_I(s) \end{bmatrix} = T_B \begin{bmatrix} F_I(s) \\ V_I(s) \end{bmatrix} \tag{3.41}$$

As we see, the determinant of the matrix is equal to one.

Similar result is also applied to the horn. The equivalent circuit of the horn is shown in Fig. 3-42. In this figure, F_J and V_J are the input voltage and current of the horn, F and V are the output voltage and current, Z_m is the load mechanical impedance. After Laplace transform, based on the impedance concept, we can define

$$Z_{h1}(s) = R_{h1} + \frac{1}{sC_{h1}} + sL_{h1} \tag{3.42}$$

$$Z_{h2}(s) = R_{h2} + \frac{1}{sC_{h2}} + sL_{h2} \tag{3.43}$$

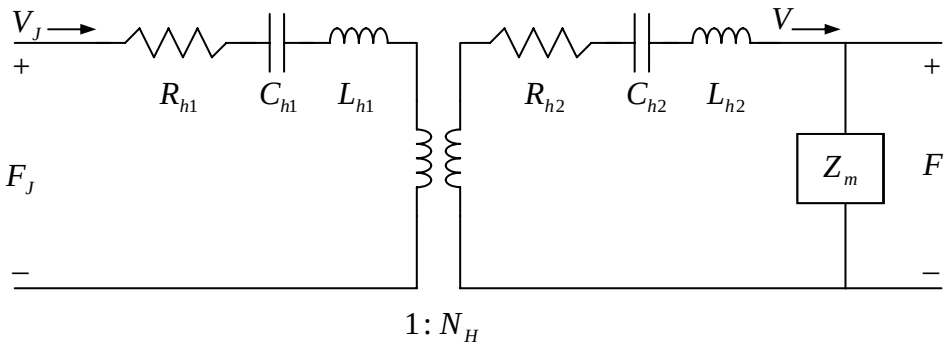

Fig. 3-42 Equivalent circuit of the horn

The relationships between the input electrical variables and the output mechanical variables of the horn are expressed by matrix as

$$\begin{bmatrix} F(s) \\ V(s) \end{bmatrix} = \begin{bmatrix} N_H & -N_H Z_{h1}(s) - Z_{h2}(s)/N_H \\ 0 & 1/N_H \end{bmatrix} \begin{bmatrix} F_J(s) \\ V_J(s) \end{bmatrix} = T_H \begin{bmatrix} F_J(s) \\ V_J(s) \end{bmatrix} \tag{3.44}$$

As we see, the determinant of the matrix is equal to one.

For analysis of the overall actuating mechanism, the equivalent circuit models of the converter, the booster and the horn may be combined in series as shown in Fig. 3-43. In the overall circuit, the definitions of the parameters are shown in Appendix C.

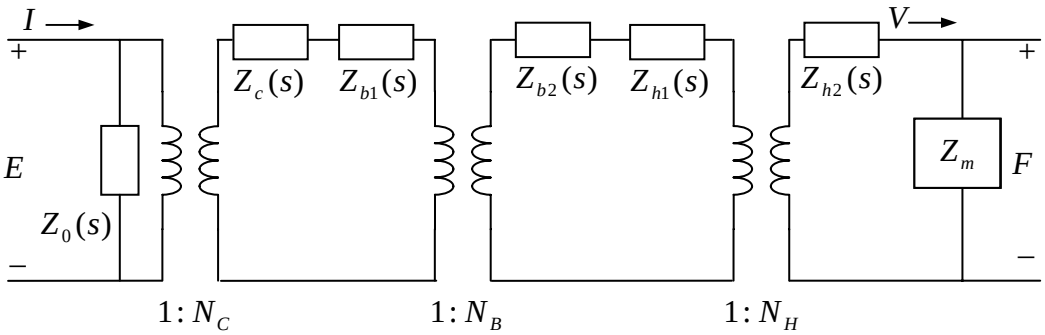

Fig. 3-43 Overall equivalent circuit of the actuating mechanism

From Eq. (3.38), Eq. (3.41) and Eq. (3.44), for the overall circuit, we can get the relationships between the input variables and the output variables as

$$\begin{bmatrix} F(s) \\ V(s) \end{bmatrix} = T_H T_B T_C \begin{bmatrix} E(s) \\ I(s) \end{bmatrix} \tag{3.45}$$

Eq. (3.45) shows that the output variables can be derived from the input variables through a transduction matrix, and the determinant of each transduction matrix is equal to one. Because ultrasonic welding system only works at one single frequency, s is constant, so the transduction matrix does not change with the input and output variables, which is the property of the actuating mechanism. Compare Eq. (3.45) with Eq. (3.10), and we will get the following relationships:

$$T_{11} = N_H N_B N_C + \frac{N_H N_B (Z_{b1} - Z_C)}{N_C Z_0} + \frac{N_H (Z_{b2} + Z_{h1})}{N_C N_B Z_0} + \frac{Z_{h2}}{N_C N_B N_H Z_0}$$

$$T_{12} = \frac{N_H N_B Z_c}{N_C} - \frac{N_H N_B Z_{b1}}{N_C} - \frac{N_H Z_{b2}}{N_B N_C} - \frac{N_H Z_{h1}}{N_B N_C} - \frac{Z_{h2}}{N_H N_B N_C}$$

$$T_{21} = \frac{-1}{N_H N_B N_C Z_0}$$

$$T_{22} = \frac{1}{N_H N_B N_C} \tag{3.46}$$

Eq. (3.46) gives the details for the relationships between each element of the transduction matrix and the system properties. Because the parameters in Eq. (3.46) are difficult to measure, we cannot use Eq. (3.46) to evaluate the transduction matrix. However, the equation for T_{21} and T_{22} can be used to validate the experimental results in some way. As we can see from the equation, T_{21} is negative, and T_{22} is positive. The values of T_{21} and T_{22} estimated from the equation are in the same order of the magnitude with the experimental results.

Chapter 4

Thermo-Mechanical Interaction in UWT

In ultrasonic welding of thermoplastics, the heating process of the workpiece directly affects the melting behavior of the joint, and consequently affects the weld strength, so it is important to study the heating process. Basically the joining of thermoplastics is due to a conversion of mechanical power (in the form of high frequency vibrations) into heat which melts the material to be joined. In this chapter, the governing equation of heat generation due to mechanical power input is first derived. The governing equation of temperature distribution in the workpiece for the transient heat transfer is also deduced based on thermodynamics.

The welding force and the dynamic compliance of the welding materials are then used as time-varying parameters when the equation is integrated along time with proper boundary conditions. A finite element method is used to solve the initial boundary value problem. Lastly, the temperature variations in the workpiece measured by the thermocouples are compared with the numerical results to validate the model of the thermo-mechanical interaction. Based on the correlation, the time-varying temperature distributions in the welding samples can be derived from the model.

4.1 Theoretical Analysis of Heating Mechanism

4.1.1 Heat Generation in UWT

Since ultrasonic welding system only works at one single frequency, the welding sample is subjected to a sinusoidal stress

$$\sigma^* = \sigma_0 \sin \omega t \tag{4.1}$$

The corresponding strain lags behind the stress by a phase angle δ as

$$\varepsilon^* = \varepsilon_0 \sin(\omega t + \delta) = \varepsilon_0 \sin \omega t \cos \delta + \varepsilon_0 \cos \omega t \sin \delta \tag{4.2}$$

The first part has the magnitude in phase with the stress. The second part has the magnitude 90^0 out of phase with the stress.

The complex compliance J^* of materials is defined as

$$J^* = \frac{\varepsilon^*}{\sigma^*} = J' - iJ'' \tag{4.3}$$

where the dynamic storage compliance J' is the ratio of the strain in phase with the stress and related to the material's ability to store elastic energy. The dynamic loss compliance J'' is the ratio of the strain 90^0 out of phase with the stress and related to the material's ability of dissipated energy or intermolecular friction. The relationship between the complex compliance J^* and the complex modulus E^* is

$$J^* = \frac{1}{E^*} = \frac{1}{E' + iE''} \tag{4.4}$$

where E' is the dynamic storage modulus, E'' is the dynamic loss modulus. The dynamic storage compliance and the dynamic loss compliance can also be expressed using the dynamic storage modulus and the dynamic loss modulus as

$$J' = \frac{E'}{E'^2 + E''^2} = \frac{1/E'}{1 + \tan^2 \delta} \tag{4.5}$$

$$J'' = \frac{E''}{E'^2 + E''^2} = \frac{1/E''}{1 + (\tan^2 \delta)^{-1}} \tag{4.6}$$

The tangent of the phase angle is called the loss factor, and it can be expressed as the ratio of the loss modulus to the storage modulus or the ratio of the loss compliance to the storage compliance as:

$$\tan \delta = \frac{E''}{E'} = \frac{J''}{J'} \tag{4.7}$$

According to the complex compliance, the strain can also be expressed as:

$$\varepsilon^* = J'\sigma_0 \sin \omega t - J''\sigma_0 \cos \omega t \tag{4.8}$$

Therefore, the total work W done in one cycle can be calculated by assuming adiabatic heating as [69]:

$$W = \oint \sigma^*(t) d\varepsilon^*(t) \tag{4.9}$$

Which can be rewritten using integration by parts as

$$\oint \sigma^*(t) d\varepsilon^*(t) = \sigma^*(t)\varepsilon^*(t)\Big|_0^{2\pi/\omega} - \oint \varepsilon^*(t) d\sigma^*(t) \tag{4.10}$$

By substituting Eq. (4.1) and Eq. (4.8) to Eq. (4.10), we get

$$\oint \sigma^*(t) d\varepsilon^*(t) = (J'\sigma_0^2 \sin^2 \omega t - J''\sigma_0^2 \sin \omega t \cos \omega t)\Big|_0^{2\pi/\omega}$$

$$- \int_0^{\frac{2\pi}{\omega}} J'\sigma_0 \sin \omega t (\sigma_0 \cos \omega t) dt + \int_0^{\frac{2\pi}{\omega}} J''\sigma_0 \cos \omega t (\sigma_0 \cos \omega t) dt \tag{4.11}$$

which is then reduced to

$$W = 0 - 0 + \pi J''\sigma_0^2 = \pi J''\sigma_0^2 \tag{4.12}$$

From Eq. (4.12), the average dissipated energy per unit time in the material is

$$\dot{Q} = \frac{W}{2\pi/\omega} = \frac{\omega\sigma_0^{\,2} J''}{2} \tag{4.13}$$

Eq. (4.13) is deduced for per unit volume of viscoelastic materials. For the specimen with cross sectional area A and height L, the average energy dissipated rate can be expressed as

$$\dot{Q} = \frac{\omega\sigma_0^{\,2} J'' AL}{2} = \frac{\omega F^2 J'' L}{2A} \tag{4.14}$$

where F is the applied force to the parts. From Eq. (4.14), the heat generation rate can be calculated from the applied force. The governing equation of heat generation rate shows that the energy dissipation is through J'', while J' produces no work. However, in the purely elastic material, the phase angle is equal to zero. According to Eq. (4.7), J'' is also equal to zero, so that there will be no dissipation for the purely elastic material. In the purely viscous material, the phase angle is 90^0, so that the storage compliance vanishes. The equation cannot be applied in the two cases.

From Eq. (4.14), we can see that the heat generation rate inside the welding sample is mainly determined by the cross sectional area, and the dissipated energy rate is inversely proportional to the local cross sectional area. For the AWS ultrasonic welding sample, the energy director has the least cross sectional area, so the highest heat generation rate occurs at the joint interface. The heat generation rate of the non-joint interface parts (including the upper part and the lower part, excluding the energy director) is much less than that of the energy director. Therefore, heating will be concentrated at the joint interface during the welding process, and the temperature of the joint interface is much higher than the non-joint interface parts.

4.1.2 Heat Transfer in UWT

Since the temperature of the joint interface is much higher than the non-joint interface parts, the heat will be transferred from the joint interface to the other positions by heat conduction, and then dissipated to the surroundings. When the heat is transferred, some heat also increases the thermodynamic energy of the parts. In the following, based on the governing equation of heat generation rate, the governing equation of the temperature for the transient heat transfer is deduced.

For AWS ultrasonic welding sample, it has the same structure along Z-axis, shown in Fig. 1-8, so the temperature distributions in the all cross sections along Z-axis are the same. Therefore, for the governing equation of temperature distributions, we can consider a two-dimensional model, shown in Fig. 4-1. In this figure, the tip of the energy director is the origin of the coordinate.

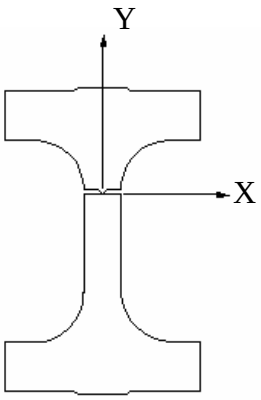

Fig. 4-1 Two-dimensional model for temperature distribution of AWS sample

Fig. 4-2 shows an arbitrary differential volume inside the domain of the two dimensional model. Here, Q_x and Q_y are the thermal energy entering the unit, and

Q_{x+dx} and Q_{y+dy} are the thermal energy leaving the unit. According to Fourier's Law for conduction, the thermal energies can be expressed as

$$Q_x = q_x l dy = -k\frac{\partial T}{\partial x} l dy \tag{4.15}$$

$$Q_y = q_y l dx = -k\frac{\partial T}{\partial y} l dx \tag{4.16}$$

$$Q_{x+dx} = Q_x + \frac{\partial Q_x}{\partial x} dx = Q_x + \frac{\partial}{\partial x}(-k\frac{\partial T}{\partial x} l dy)dx = Q_x - k\frac{\partial^2 T}{\partial x^2} l dy dx \tag{4.17}$$

$$Q_{y+dy} = Q_y + \frac{\partial Q_y}{\partial y} dy = Q_y + \frac{\partial}{\partial y}(-k\frac{\partial T}{\partial y} l dx)dy = Q_y - k\frac{\partial^2 T}{\partial y^2} l dx dy \tag{4.18}$$

where $T = T(x, y, t)$, l is the length of the sample, and k is the thermal conductivity.

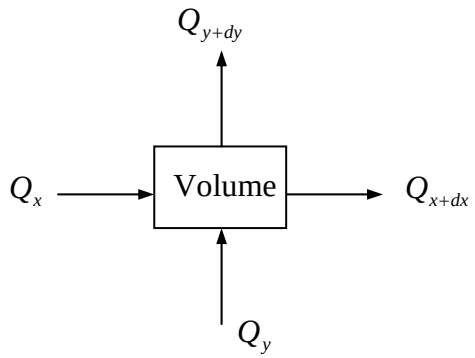

Fig. 4-2 Volume for thermal energy relationships

According to the first law of thermodynamics, the following relationship exists: thermal energy entering the unit + internal heat generation of the unit = thermal energy leaving the unit + change of the thermodynamic energy of the unit [71]. Therefore, there will be

$$Q_x + Q_y + \dot{Q} l dx dy = Q_{x+dx} + Q_{y+dy} + \rho c\frac{\partial T}{\partial t} l dx dy \tag{4.19}$$

where ρ is the density of the material, and c is the specific heat of the material.

By substituting Eq. (4.14), Eq. (4.15), Eq. (4.16), Eq. (4.17) and Eq. (4.18) to Eq. (4.19), we can get

$$\rho c \frac{\partial T}{\partial t} l dx dy = k \frac{\partial^2 T}{\partial x^2} l dx dy + k \frac{\partial^2 T}{\partial y^2} l dx dy + \frac{\omega F^2 J'' L}{2A} l dx dy \tag{4.20}$$

It will reduce to

$$k \frac{\partial^2 T}{\partial x^2} + k \frac{\partial^2 T}{\partial y^2} + \frac{\omega F^2 J'' L}{2A} - \rho c \frac{\partial T}{\partial t} = 0 \tag{4.21}$$

This equation is the governing equation of the temperature for the transient heat transfer. In this equation, the applied force F is time varying; the dynamic loss compliance J'' of the welding material is the function of time-varying temperature, so J'' is also time varying. Based on the boundary condition and the initial condition, provided that F and J'' are known, we can calculate the time-varying temperature distributions in the welding sample during ultrasonic welding by solving the governing equation with a step size of the welding time.

For the boundary condition of the above governing equation, an equivalent circuit model for the heat transfer is developed. As we know, there exists an analogy between the diffusion of heat and the electrical charge. From this analogy, temperature is equivalent to voltage, and heat flux is equivalent to current [72]. Fig. 4-3 shows the equivalent thermal circuit model for the heat transfer from the joint interface to the surroundings.

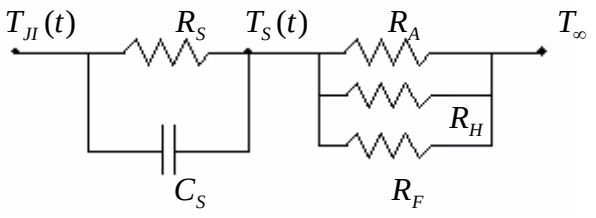

Fig. 4-3 Equivalent thermal circuit for the heat transfer

In this model, $T_{JI}(t)$, $T_S(t)$ and T_∞ are the temperatures of the joint interface, the surface of the sample, and the surroundings respectively. R_S is the heat conduction from the joint interface to the surface, R_A donates the heat convection from the surface to the air, and R_H, R_F represent the heat conduction from the surface to the horn and to the fixture respectively. C_S is the thermodynamic energy of the sample. Comparing the thermodynamics equation $q = \rho v c \frac{\partial T}{\partial t}$ with electrical capacitor equation $E = \frac{1}{C}\int I dt$, we can get the thermal capacitance as

$$C_S = \rho v_s c \tag{4.22}$$

where v_s is the volume of the sample.

From the equivalent thermal circuit, the heat mainly loses to the air by heat convection, and to the horn and the fixture by heat conduction. The governing equation of the heat flux to the surroundings is

$$q_n = h(T_S - T_\infty) + k_h(T_S - T_\infty)/l_h + k_f(T_S - T_\infty)/l_f \tag{4.23}$$

where h is the heat convection coefficient of the material to the air. k_h and k_f are the heat conduction coefficients of the horn and the fixture respectively, and l_h and l_f are the distances for the heat conduction of the horn and the fixture respectively. Because there is melting behaviour at the joint interface, the governing equation of the heat generation rate does not apply to the heating of the joint interface, so the temperature of the joint interface $T_{JI}(t) = T(0,0,t)$ is considered as another boundary condition, which can be measured easily using a thermocouple.

4.2 Force Detection in Ultrasonic Welding

According to the transduction matrix of the actuating mechanism, the output force and velocity can be derived from the input voltage and current through the transduction matrix, which is repeated as

$$F = T_{11}E + T_{12}I \tag{4.24}$$

$$V = T_{21}E + T_{22}I \tag{4.25}$$

Therefore, the heat generation rate equation Eq. (4.14) can be expressed as

$$\dot{Q} = \frac{\omega F^2 J'' L}{2A} = \frac{\omega J'' L \,|\, T_{11}E + T_{12}I \,|^2}{2A} \tag{4.26}$$

The governing equation of the temperature Eq. (4.21) can also be expressed as

$$k\frac{\partial^2 T}{\partial x^2} + k\frac{\partial^2 T}{\partial y^2} + \frac{\omega J'' L \,|\, T_{11}E + T_{12}I \,|^2}{2A} - \rho c\frac{\partial T}{\partial t} = 0 \tag{4.27}$$

Assume the displacement of the horn-workpiece interface during welding is

$$x = A_0 e^{j\omega t} \tag{4.28}$$

and then, the corresponding velocity is

$$V = \dot{x} = (j\omega)A_0 e^{j\omega t} = j\omega x \tag{4.29}$$

where A_0 is the vibration amplitude, ω is the working angular frequency, and t is time. From Eq. (4.29), the amplitude of the velocity is proportional to the amplitude of displacement.

In the following, we will use the transduction matrix of the actuating mechanism to evaluate the force and the displacement in ultrasonic welding. Fig. 4-4 and Fig. 4-7 show the measured voltage and current during the heating process for PP and PC

respectively. Fig. 4-5 and Fig. 4-8 show the amplitude of the force during the heating process for PP and PC respectively. From Eq. (4.29), the displacement can be derived from the velocity. Fig. 4-6 and Fig. 4-9 show the amplitude of the displacement during the heating process for PP and PC respectively, which can reflect the deformation of the energy director because the energy director is the softest part in the workpiece.

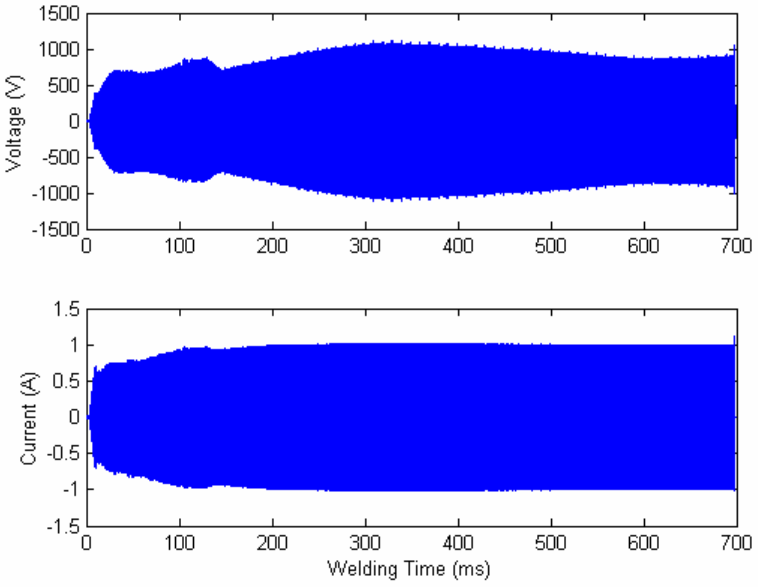

Fig. 4-4 Voltage and current for PP during ultrasonic welding

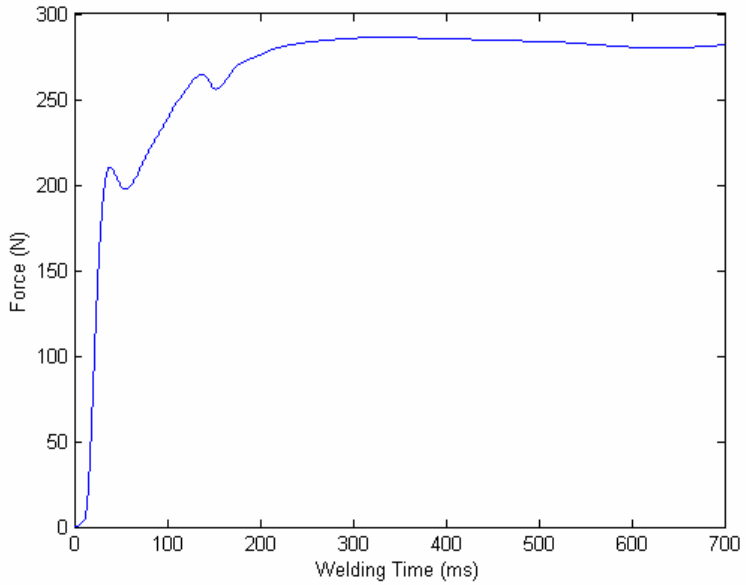

Fig. 4-5 Amplitude of force for PP during ultrasonic welding

The displacement calculated through the transduction matrix is the displacement of the tip of the horn. This vibration amplitude transmits through a system with horn, upper workpiece, energy director and lower workpiece in series. Since the stiffness of the energy director is much smaller than other components in the system, the displacement of horn tip is ideally 100% transmitted into the deformation of the energy director.

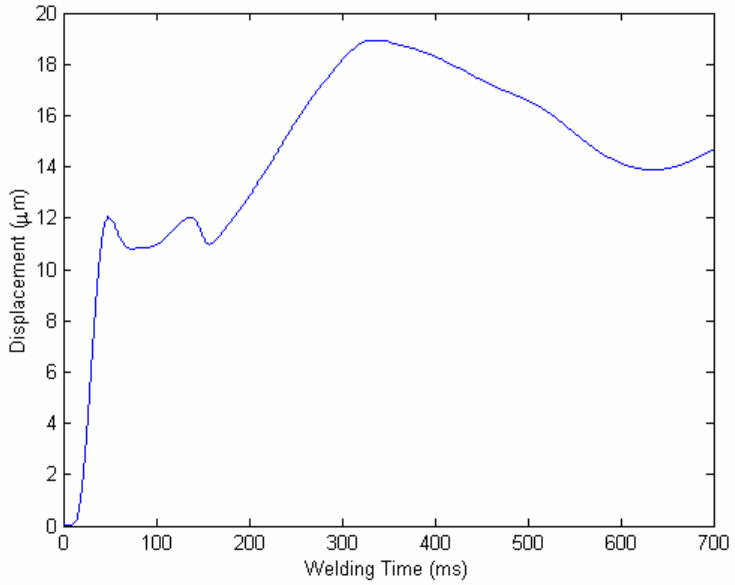

Fig. 4-6 Amplitude of displacement for PP during ultrasonic welding

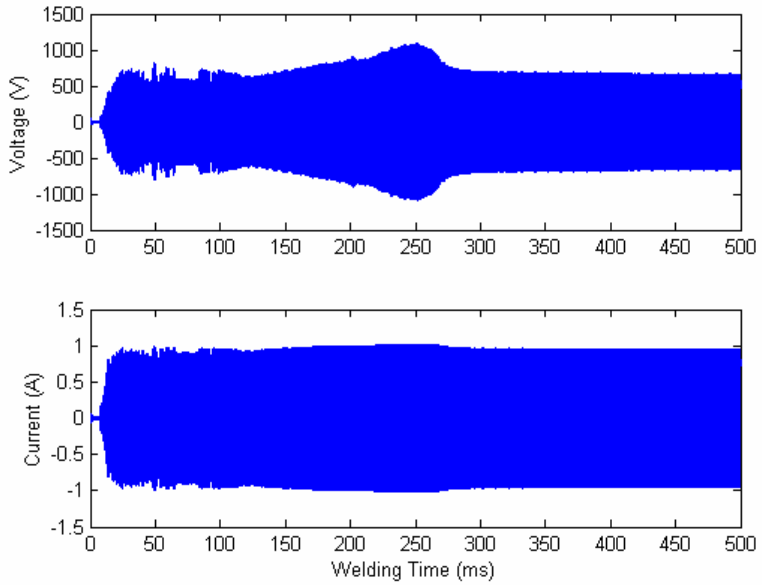

Fig. 4-7 Voltage and current for PC during ultrasonic welding

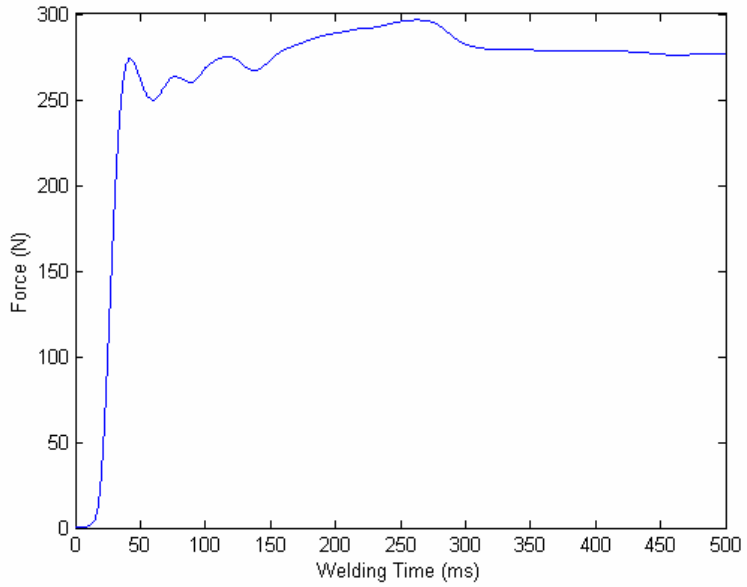

Fig. 4-8 Amplitude of force for PC during ultrasonic welding

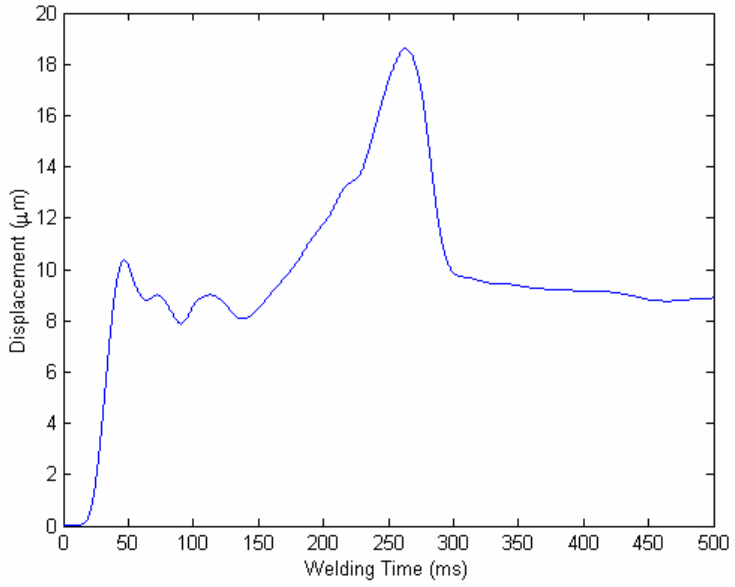

Fig. 4-9 Amplitude of displacement for PC during ultrasonic welding

4.3 Measurement of Dynamic Compliance of Welding Materials

4.3.1 Relationship between Compliance and Impedance

The dynamic compliance or the dynamic modulus of a material is functions of both frequency and temperature. For ultrasonic welding of thermoplastics, the welding system only works at one single frequency. Therefore, the dynamic compliance or the dynamic modulus is only a function of temperature. Normally, the dynamic modulus is used to describe the properties of thermoplastics.

Temperature is the most important factor affecting the properties of viscoelastic materials. The dynamic modulus changes significantly with the temperature during the heating process. The material softens and the storage modulus drops near the glass transition temperature T_m for amorphous materials or the melting temperature T_g for semi-crystalline materials, and the loss factor increases drastically, resulting in increased energy dissipation. Then, the material will be approximately purely viscous with a low storage modulus and a high loss angle.

The behavior of viscoelastic materials in the heating process can be divided into four different regions: the glassy region, the transition region, the rubberlike region and the flow region with the sequence from low temperature to high temperature. The glass region occurs near the room temperature. In this region, the storage modulus decreases slightly and the loss factor increases sharply as the temperature increases. This trend will continue in the next region, the transition region, until the transition temperature T_g is reached. At the transition temperature T_g, the loss factor reaches its maximum value, while the storage modulus decreases. In the third region, the rubberlike region,

both the storage modulus and the loss factor nearly remain constant. This trend continues in the flow region, in which the storage modulus decreases and the loss factor increases. The typical plot of the storage modulus and loss factor vs. temperature is presented in Fig. 4-10.

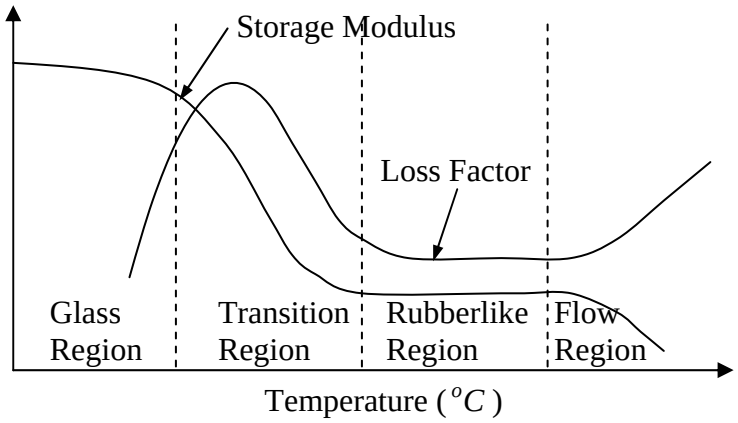

Fig. 4-10 Modulus and loss factor vs. temperature [73]

For such a high working frequency of ultrasonic welding system, it is very difficult to measure the dynamic compliance or the dynamic modulus. From the literature review, those available methods are not reliable for such a high frequency. Here, a new method to measure the dynamic compliance at the given ultrasonic frequency is proposed. Using this method, the dynamic compliance can be derived from the input electrical impedance of ultrasonic welding system, which can be easily measured.

Firstly, we define the inverse of impedance as admittance

$$R_e = \frac{I}{E}, \text{ Electrical admittance} \tag{4.30}$$

$$R_m = \frac{V}{F}, \text{ Mechanical admittance} \tag{4.31}$$

According to the transduction matrix of the actuating mechanism, we can get the relationship between the input electrical admittance and the output mechanical admittance of the actuating mechanism as

$$R_m = \frac{T_{21} + T_{22} R_e}{T_{11} + T_{12} R_e} \tag{4.32}$$

For the cuboid specimen (see Fig. 4-11), its cross sectional area is A_s, and h is its height. If we use the specimen as the welding sample, the dynamic compliance will be

$$J^* = \frac{\varepsilon^*}{\sigma^*} = \frac{\Delta h^* / h}{F / A_s} = \frac{\Delta h^*}{F} \cdot \frac{A_s}{h} \tag{4.33}$$

where Δh^* is the horn displacement in complex value, F is the applied force.

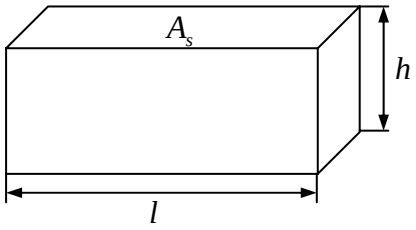

Fig. 4-11 Specimen for measuring the dynamic compliance

From Eq. (4.29), we can get the horn displacement as

$$\Delta h^* = \frac{V}{j\omega} \tag{4.34}$$

Substitute Eq. (4.34) with Eq. (4.33), and it will be

$$J^* = \frac{V}{F} \cdot \frac{A_s}{j\omega h} = \frac{R_m A_s}{j\omega h} \tag{4.35}$$

Substitute Eq. (4.32) into Eq. (4.35), and the dynamic compliance is

$$J^* = \frac{A_s (T_{21} + T_{22} R_e)}{j\omega h (T_{11} + T_{12} R_e)} \tag{4.36}$$

Eq. (4.36) shows that the dynamic compliance can be derived from the input admittance. From Eq. (4.30), the dynamic compliance can also be derived from the input electrical impedance as

$$J^* = \frac{A_s(T_{21}Z_e + T_{22})}{j\omega h(T_{11}Z_e + T_{12})} \tag{4.37}$$

The dynamic modulus can also be derived from the input electrical admittance and impedance as

$$E^* = \frac{1}{J^*} = \frac{j\omega h(T_{11} + T_{12}R_e)}{A_s(T_{21} + T_{22}R_e)} \tag{4.38}$$

$$E^* = \frac{1}{J^*} = \frac{j\omega h(T_{11}Z_e + T_{12})}{A_s(T_{21}Z_e + T_{22})} \tag{4.39}$$

From Eq. (4.14), we can see that the same heat generation rate occurs throughout the specimen because the specimen has the same cross sectional area perpendicular to the direction of the force. Hence, the temperature should be same throughout the specimen. From Eq. (4.37), the dynamic compliance of material with the time at the working frequency can be derived from the electrical impedance. The corresponding temperature with time can be measured to get the dynamic compliance vs. temperature.

4.3.2 Experimental Results

In the present section, Eq. (4.37) is used to calculate the dynamic compliance of materials at 20 kHz from the electrical impedance. The dimension of the specimen used in this experiment is $12.79mm \times 19.55mm \times 50.95mm$, so $h = 1.955 \times 10^{-2} m$, and $A_s = 12.79 \times 50.95 = 6.517 \times 10^{-4} m^2$. The machine settings for the experiment for both

PP and PC are listed in Table 4-1, in which weld time is set at 700 ms because of the limitations of the instruments.

Table 4-1 Experimental settings for compliance measurement

	PP	PC
Downspeed	1.5 m/s	1.5 m/s
Weld Time	700 ms	700 ms
Amplitude	30%	20%
Pressure	60 PSI	50 PSI

However, there is a range for the experimental settings that the strain must be in its linear elastic range. For example, for PP material, the strain must be less than 1.5% in the linear elastic range [73]. For the specimen, the maximum strain for PP is $|\Delta h^*|_{\max} = |\varepsilon^*|_{\max}\ h = 1.5\% \times 19.55 = 0.29mm$. For PC material, the strain must be less than 1.1% in the linear elastic range [73], so the maximum strain for PC is $|\Delta h^*|_{\max} = |\varepsilon^*|_{\max}\ h = 1.1\% \times 19.55 = 0.21mm$. During welding, the horn and the specimen have the deformation simultaneously, but the hardness of the horn is much bigger than the sample, so we can only consider the deformation of the specimen for this estimation. From Eq. (4.29), we can get the maximum velocity as $V_{\max} = |\Delta h^*|_{\max}\ \omega = 36.4m/s$ for PP material and $V_{\max} = |\Delta h^*|_{\max}\ \omega = 26.4m/s$ for PC material. According to the reference, the velocity of the horn output is $5m/s$ nearly when the machine is set to 100% amplitude, much less than $36.4m/s$ and $26.4m/s$,

so the strain is in its linear elastic range for both PP material and PC material. Therefore, Eq. (4.37) is applied to all conditions.

The measured voltage and current for PP and PC are shown in Fig. 4-12 and Fig. 4-17 respectively. From the voltage and current, the calculated real part and imaginary part of electrical impedance are shown in Fig. 4-13 and Fig. 4-18 respectively. By using Eq. (4.37), the calculated real part and imaginary part of the dynamic compliance with welding time are shown in Fig. 4-14 and Fig. 4-19 respectively, and the corresponding temperatures with welding time are shown in Fig. 4-15 and Fig. 4-20 respectively. Because there is some oscillation in the beginning period and end period of the process, we only use the middle period of the process from 60 ms to 680 ms. From the real time dynamic compliance and the corresponding temperature, the real part and the imaginary part of the dynamic compliance vs. temperature are plotted in Fig. 4-16 for PP and Fig. 4-21 for PC.

For this measurement, the temperature range for PP is below the melting temperature, and the temperature range for PC is below the glass transition temperature. Hence, there are no peaks in the dynamic compliance for both PP and PC. The storage compliance is high at low temperatures because the polymer is glassy. As the temperature increases, the polymer will soften and be rubbery, so the storage compliance is low at high temperatures. The loss compliance increases with the rising temperature because of the glassy to rubbery transition [74].

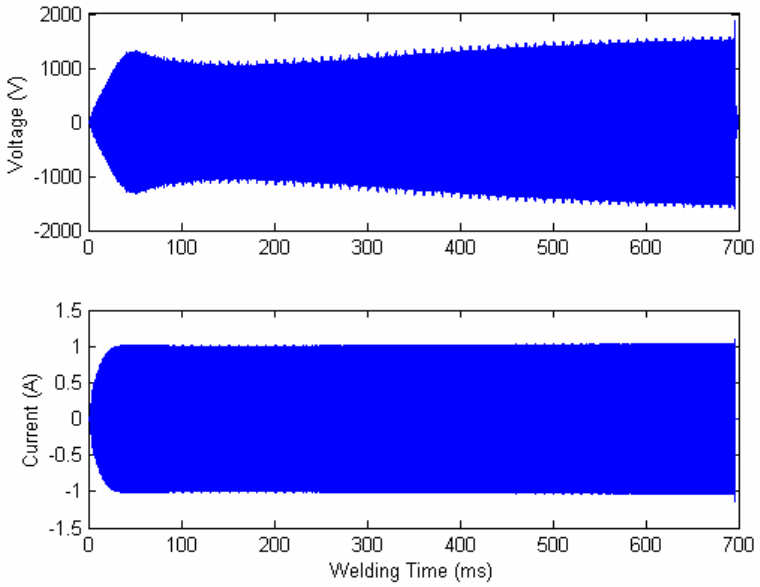

Fig. 4-12 Voltage and current for compliance measurement of PP

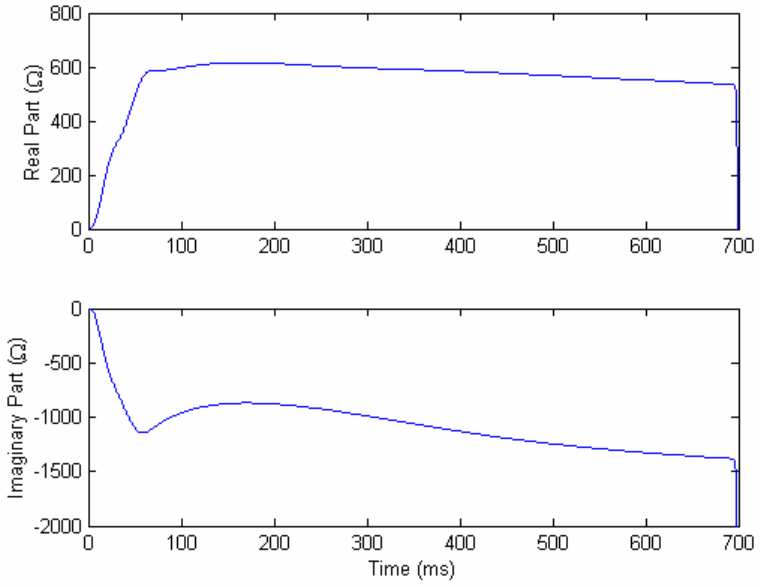

Fig. 4-13 Electrical impedance for compliance measurement of PP

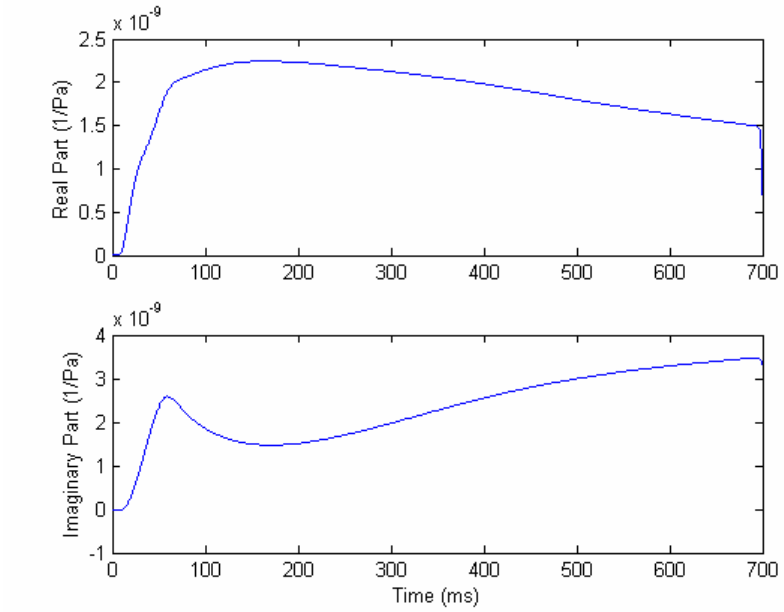

Fig. 4-14 Dynamic compliance with welding time for PP

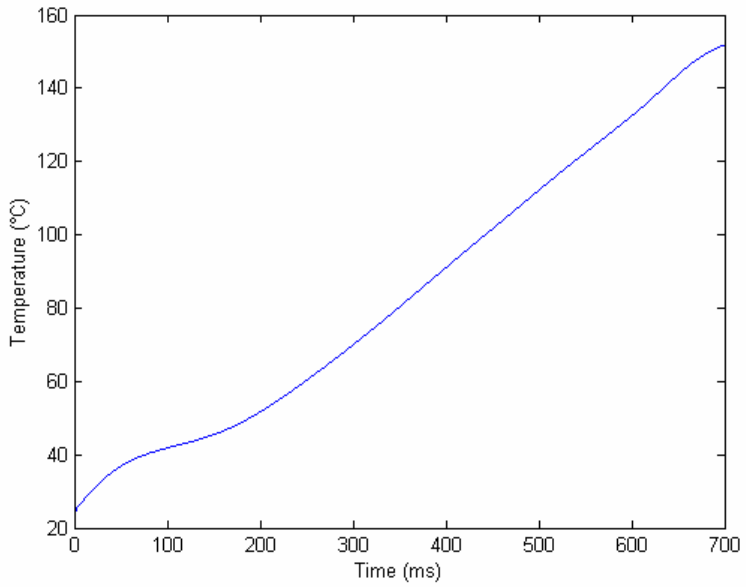

Fig. 4-15 Temperature variation with welding time for PP

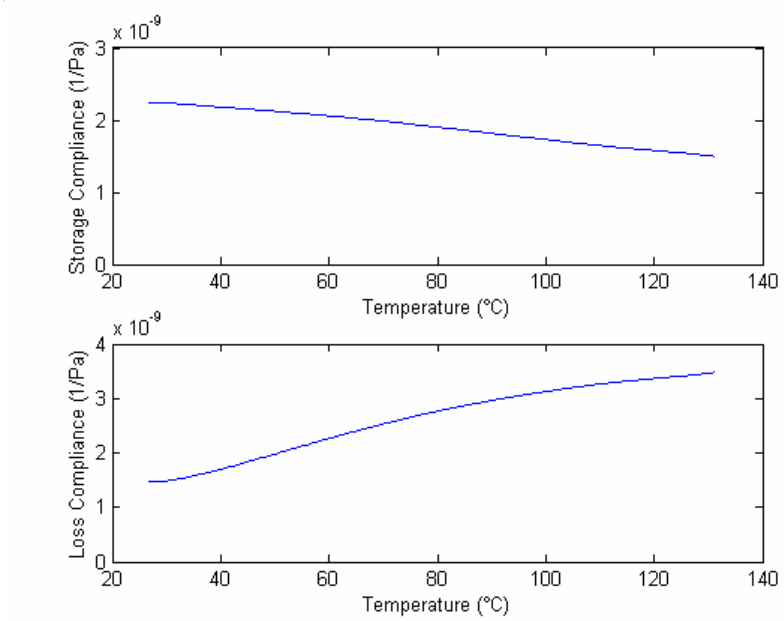

Fig. 4-16 Dynamic compliance vs. temperature for PP at 20 kHz

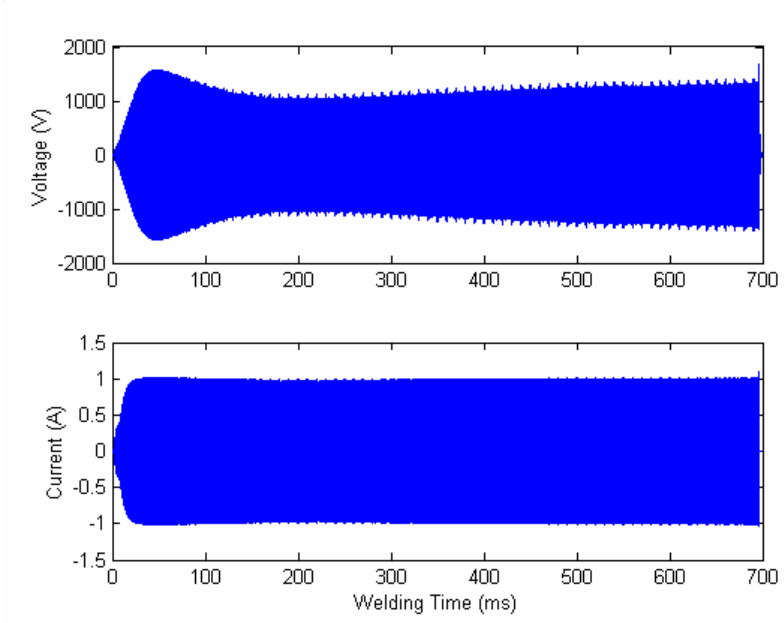

Fig. 4-17 Voltage and current for compliance measurement of PC

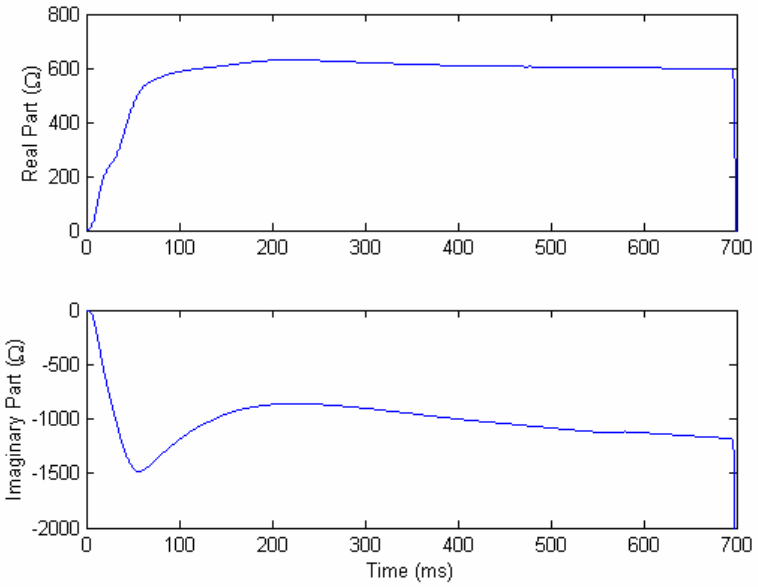

Fig. 4-18 Electrical impedance for compliance measurement of PC

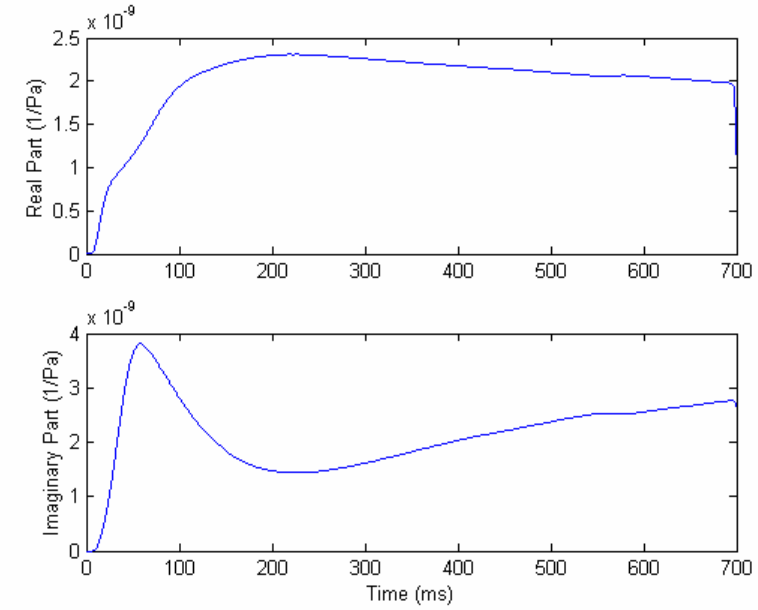

Fig. 4-19 Dynamic compliance with welding time for PC

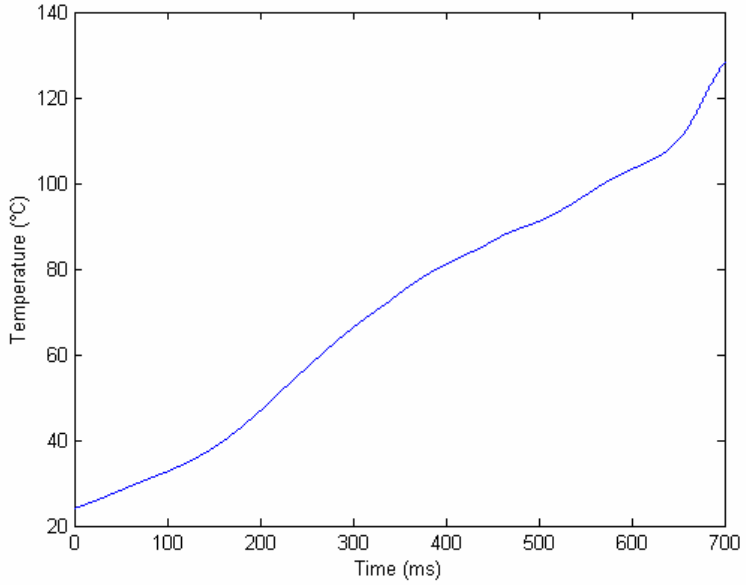

Fig. 4-20 Temperature variation with welding time for PC

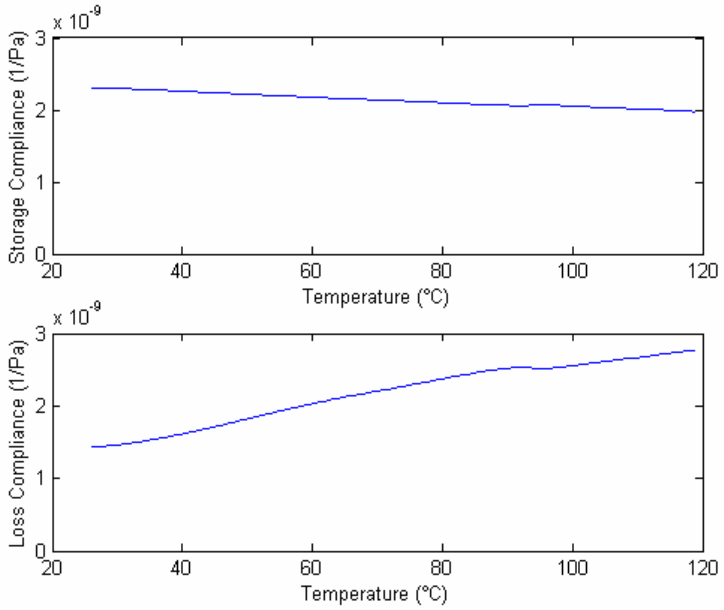

Fig. 4-21 Dynamic compliance vs. temperature for PC at 20 kHz

4.4 Finite Element Simulation of Heating Process

With the above evaluated force F during ultrasonic welding and the dynamic loss compliance of the welding materials, the time-varying temperature distributions in the welding sample during ultrasonic welding can be calculated by solving the governing equation the temperature for the transient heat transfer (Eq. (4.21)) with a step size of the welding time. However, it is difficult to solve the governing equation of analytically, so finite element method is used to solve this equation. By applying Galerkin weighted residual method, the governing equation is first expressed in the weighted residual form as follows:

$$\iint_A v\left[k\frac{\partial^2 T}{\partial x^2}+k\frac{\partial^2 T}{\partial y^2}+\frac{\omega F^2 J'' L}{2A}-\rho c\frac{\partial T}{\partial t}\right]dxdy=0 \tag{4.40}$$

where $v=v(x,y)$ is a weight function.

The first and second items in the left part of Eq. (4.40) can be rewritten using integration by parts as

$$kv\frac{\partial^2 T}{\partial x^2}=\frac{\partial}{\partial x}(kv\frac{\partial T}{\partial x})-k\frac{\partial T}{\partial x}\cdot\frac{\partial v}{\partial x} \tag{4.41}$$

$$kv\frac{\partial^2 T}{\partial y^2}=\frac{\partial}{\partial y}(kv\frac{\partial T}{\partial y})-k\frac{\partial T}{\partial y}\cdot\frac{\partial v}{\partial y} \tag{4.42}$$

Using the substitutions Eq. (4.41) and Eq. (4.42) in Eq. (4.40), we can get the following expression:

$$\iint_A\left[\frac{\partial}{\partial x}(kv\frac{\partial T}{\partial x})+\frac{\partial}{\partial y}(kv\frac{\partial T}{\partial y})\right]dxdy-\iint_A\left[k\frac{\partial T}{\partial x}\cdot\frac{\partial v}{\partial x}+k\frac{\partial T}{\partial y}\cdot\frac{\partial v}{\partial y}\right]dxdy$$

$$+\iint_A\frac{\omega F^2 J'' Lv}{2A}dxdy-\iint_A\rho cv\frac{\partial T}{\partial t}dxdy=0 \tag{4.43}$$

According to Green's theorem [75], there will have:

$$\iint_A (\frac{\partial F}{\partial x} + \frac{\partial G}{\partial y}) dxdy = \oint_S (Fn_x + Gn_y) dS \tag{4.44}$$

where dS is the differential length along the boundary curve, and n_x, n_y are defined as the components of the n vector along the x and y axes respectively. The Green's theorem can be used to rewrite the terms in the first integral of Eq. (4.43), then Eq. (4.43) becomes

$$\oint_S \left[(kv\frac{\partial T}{\partial x})n_x + (kv\frac{\partial T}{\partial y})n_y \right] dS - \iint_A \left[k\frac{\partial T}{\partial x}\cdot\frac{\partial v}{\partial x} + k\frac{\partial T}{\partial y}\cdot\frac{\partial v}{\partial y} \right] dxdy$$

$$+ \iint_A \frac{\omega F^2 J^{"} Lv}{2A} dxdy - \iint_A \rho cv\frac{\partial T}{\partial t} dxdy = 0 \tag{4.45}$$

Based on the contour integral over the flux boundary S, the first item in Eq. (4.45) can be also rewritten as

$$\oint_S \left[(kv\frac{\partial T}{\partial x})n_x + (kv\frac{\partial T}{\partial y})n_y \right] dS = \oint_S \left[-vq_x n_x - vq_y n_y \right] dS = -\oint_S vq_n dS \tag{4.46}$$

where q_n is the boundary heat flux to the surroundings. Therefore, Eq. (4.45) can be rewritten in the following form:

$$\iint_A \begin{bmatrix} \frac{\partial v}{\partial x} & \frac{\partial v}{\partial y} \end{bmatrix} \begin{bmatrix} k & 0 \\ 0 & k \end{bmatrix} \begin{Bmatrix} \frac{\partial T}{\partial x} \\ \frac{\partial T}{\partial y} \end{Bmatrix} dxdy = \iint_A \frac{\omega F^2 J^{''} Lv}{2A} dxdy - \iint_A \rho cv\frac{\partial T}{\partial t} dxdy - \oint_S vq_n dS \tag{4.47}$$

This equation is the matrix expression of the governing equation of the temperature in the weighted residual form.

The solution in the domain of the two dimensional model is divided into m elements of n nodes each. Considering the trial solution for T in terms of the shape functions, the nodal temperatures are in the form

$$T = [N]\{T(t)\} \tag{4.48}$$

where $\{T(t)\}$ is the nodal temperature vector, and $[N]$ is the shape function matrix, which should meet the requirements of the simulation.

Using Eq. (4.48), the temperature gradient vector can be written as

$$\begin{Bmatrix} \frac{\partial T}{\partial x} \\ \frac{\partial T}{\partial y} \end{Bmatrix} = [B]\{T(t)\} \tag{4.49}$$

where $[B]$ is the gradient matrix of the shape function [76].

In the Galerkin weighted residual method, the test function v, uses the same shape functions as the trial function. Therefore, it can be written in the form

$$v = [N]\{c\} \tag{4.50}$$

Since the test function can be chosen arbitrarily, the vector $\{c\}$ is arbitrary, i.e., its elements can take any arbitrary numerical values. Moreover, as v is one number and the transpose of a number is equal to the number itself, i.e. $v = v^T$, Eq. (4.50) can also be written as [75]

$$v = \{c\}^T [N]^T \tag{4.51}$$

Similar to Eq. (4.49), we can write

$$\begin{Bmatrix} \frac{\partial v}{\partial x} \\ \frac{\partial v}{\partial y} \end{Bmatrix} = [B]\{c\} \tag{4.52}$$

Using Eq. (4.48), Eq. (4.49), Eq. (4.51) and Eq. (4.52) in Eq. (4.47), we get the following expression:

$$\{c\}^T\left[\left(\iint_A k[B]^T[B]\{T(t)\}dxdy\right)-\iint_A[N]^T\frac{\omega F^2 J^{''}L}{2A}dxdy+\iint_A[N]^T\rho c\frac{\partial T}{\partial t}dxdy\right.$$

$$\left.+\oint_S[N]^T q_n dS\right]=0 \tag{4.53}$$

Since $\{c\}^T$ in Eq. (4.53) is arbitrary, we can get the following element matrix function:

$$\iint_A k[B]^T[B]\{T(t)\}dxdy=\iint_A[N]^T\frac{\omega F^2 J^{''}L}{2A}dxdy-\iint_A[N]^T\rho c\frac{\partial T}{\partial t}dxdy$$

$$-\oint_S[N]^T q_n dS \tag{4.54}$$

This equation is the governing function of the elements for finite element simulation. With the evaluated force during the heating process, the dynamic loss compliance and the other parameters of the welding materials, we can get the temperature variations with welding time by solving Eq. (4.54). One boundary condition for Eq. (4.54) is the temperature of the joint interface, and the other boundary condition is the heat flux to the surroundings Eq. (4.23), which remains with the following expression by using the shape function and the nodal temperature vector:

$$q_n=h([N]\{T(t)\}-T_\infty)+k_h([N]\{T(t)\}-T_\infty)/l_h+k_f([N]\{T(t)\}-T_\infty)/l_f \tag{4.55}$$

The model with the above governing element matrix function and the boundary conditions for finite element simulation is called the finite element model for the heating process. In the next section, for both PP and PC materials, the temperatures of the joint interface are measured as the boundary conditions, and the temperatures of the non-joint interface are also measured to validate the finite element model.

4.5 Measurement of Temperatures

4.5.1 Experimental Setup and Signal Processing

The experimental setup for measuring temperatures is shown in Fig. 4-22. In this experiment, one thermocouple (Type K, 36 AWG PFA [78]) is put at the joint interface of the welding sample, where Omegabond 100 (fast setting room temperature epoxy adhesive) is used to fix the thermocouple at the joint interface. The other thermocouple (Type K, 36 AWG PFA) is put near to the joint interface, where a 0.5 mm hole is drilled, and Omegatherm 201 (high thermal conductivity paste) is used to fill with the hole. The measured point near to the joint interface is called as "the point near joint", which is 5.20 mm away from the top surface of the sample for this case. For this investigation, the point near joint represents the non-joint interface. The two thermocouples are connected with an electric reference junction temperature compensator (Chino Model TO-K). Then, an analog filter (Krohn-Hite Model 3944) is used to cut down the noise to avoid aliasing, and a digital oscilloscope (Nicolet Integra 40) is used to collect the data. Finally, the data is transferred into a computer for processing.

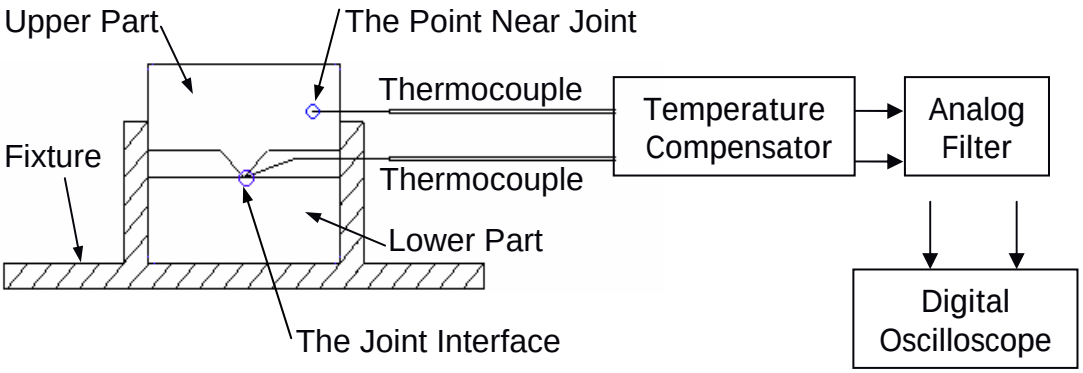

Fig. 4-22 Experimental setup for temperatures measurement

For the type K thermocouple, after calibration, the experimental results for the relationship between the output thermoelectric voltage and the measured temperature are shown in Fig. 4-23. From the figure, we can see that the relationship is nearly like a straight line. However, for more exacted results, we use a polynomial to fit the relationship as

$$T = c_0 + c_1 E + c_2 E^2 + c_3 E^3 + c_4 E^4 + c_5 E^5 \tag{4.56}$$

where E is the thermoelectric voltage in microvolts, and T is the temperature in Celsius degrees. The values of the polynomial coefficients are shown in Table 4-2. Using this polynomial, the fitting errors between the measured values of the temperature and the calculated values of the temperature are from $-0.5^o C$ to $0.4^o C$, which satisfies the engineering requirements for this application. Therefore, Eq. (4.56) can be used to calculate the temperatures from the output voltages of the thermocouples.

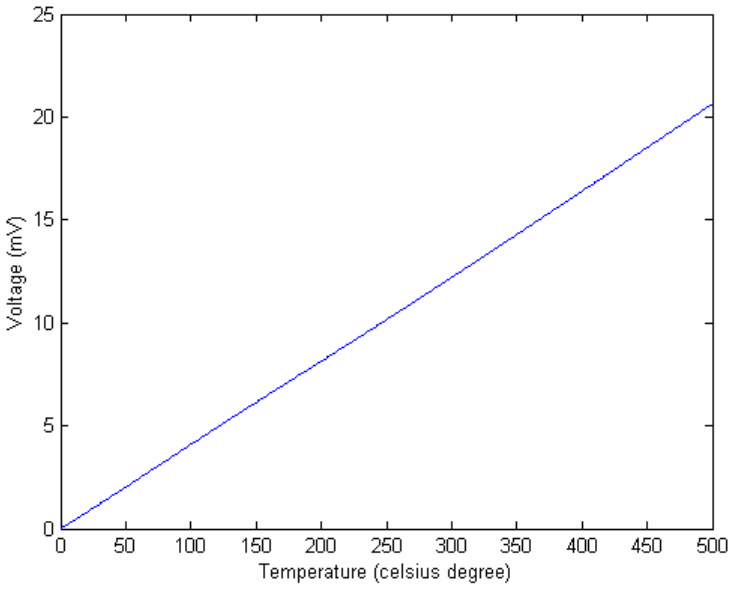

Fig. 4-23 Thermoelectric voltage as the function of the temperature for type K

Table 4-2 Coefficients of the fitting polynomial

Coefficient	Value	Coefficient	Value
c_0	0.000000	c_3	-2.503131×10^{-10}
c_1	2.508355×10^{-2}	c_4	8.315270×10^{-14}
c_2	7.860106×10^{-8}	c_5	-1.228034×10^{-17}

Using the fitting result, we can measure the temperature changes in the welding sample. However, the measured signals are always mixed with a lot of noise because of the small value of the thermoelectric voltage and the environment noise. The temperature signals are DC signals at low frequencies, but the noise is at the high frequencies. Fig. 4-24 shows the distribution of the measured temperature signals in the frequency domain. From the figure, we can see that the frequencies of the temperature signals are mainly less than 10 Hz. Therefore, we can use the 10 Hz Butterworth low-pass analog filter to cut off the noise. The frequency response of Butterworth 10 Hz low-pass analog filter is shown in Fig. 4-25. Because we only consider the amplitude of the signal for temperature, the Butterworth filter can condition the signal from the temperature compensator. In the following, using the experimental setup and signal processing, the temperature of the joint interface and the temperature of the point near joint in the heating process are investigated.

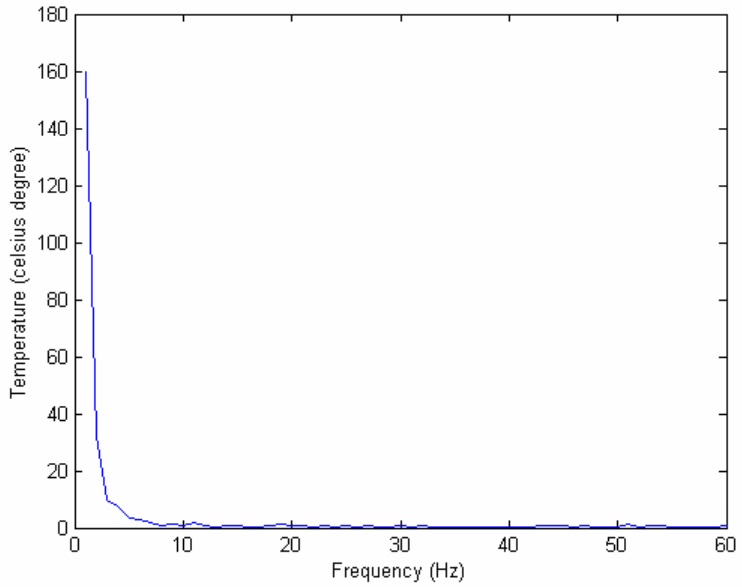

Fig. 4-24 Measured temperature signals distribution in frequency domain

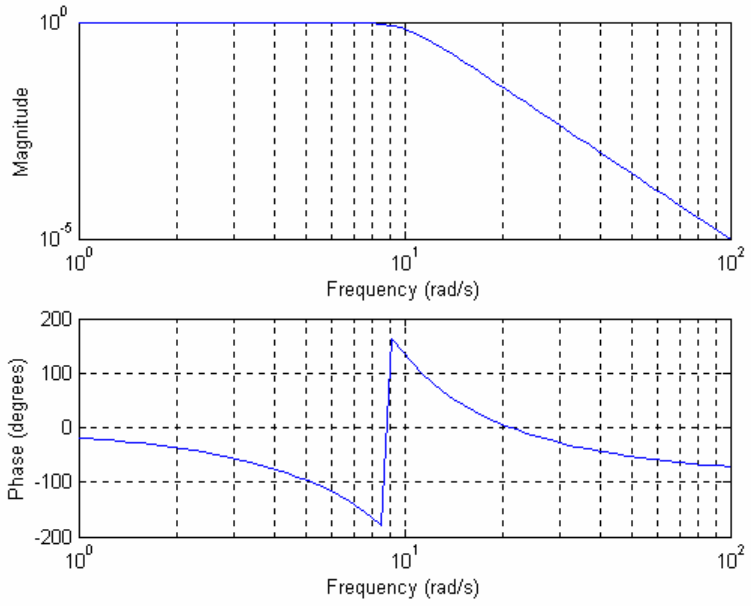

Fig. 4-25 Butterworth 10 Hz low-pass analog filter frequency response

4.5.2 Experimental Results

To study the heating process, the temperature of the joint interface and the temperature of the point near the joint in the welding samples are investigated. For PP materials, the typical results with weld time 700 ms are plotted in Fig. 4-26. For PC materials, the typical results with weld time 500 ms are plotted in Fig. 4-27. As shown in the two figures, in the initial period of the heating process (before melting occurs for PP or before glass transition for PC), the heat generation rates at the joint interface are very high, so the temperatures of the joint interface for both PP and PC increase rapidly, while the temperatures of the point near the joint increase slowly, which are similar with Tolunay and Tateishi's results. After the initial period, for PP material, the temperature of the joint interface will reach the melting temperature of PP (around 168°C), and stay for a period for melting, which is similar with Tateishi's results, while the temperature of the point near the joint continues to increase slowly because of the local heating and heat conduction from the joint interface. When the melting ends, both the two temperatures begin to increase rapidly. For PC material, when the temperature of the joint interface reaches the glass transition temperature of PC (around 145°C), the increase of the temperature has a lower rate because the dynamic loss compliance decreases, which is similar with Tolunay's results. The same change applies to the temperature of the point near joint because of the local heating and heat conduction from the joint interface. Finally, when the weld times end, all the temperatures for both PP and PC begin to decrease because of no input energy and heat loss, and the differences between the temperatures of the joint interface and the temperatures of the point near joint decrease due to the heat transfer.

From the above results, the temperature variations of the joint interface and the point near joint during the heating process reflect both the heat generation theory and the heat transfer theory. As shown in the experimental results, heating mainly occurs at the joint interface, and the temperature of the joint interface can reflect the discussed phase change, so it is a characteristic variable of the heating process, especially for PP.

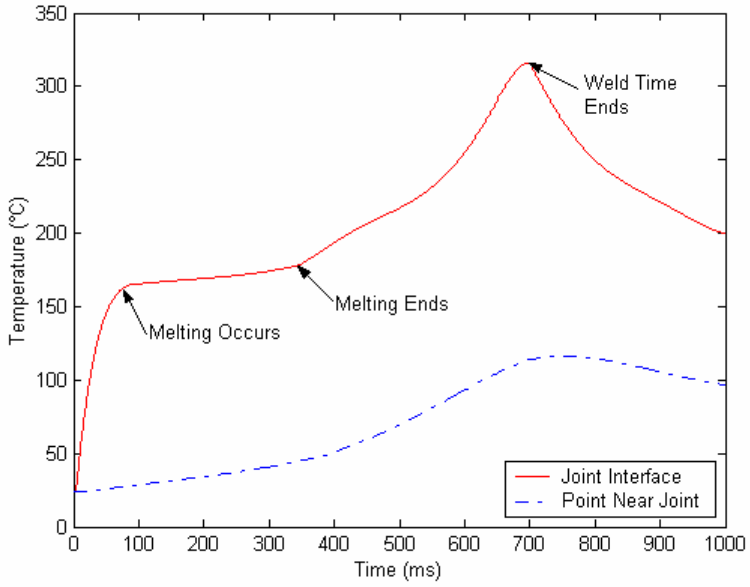

Fig. 4-26 Temperature variations for PP during the heating process

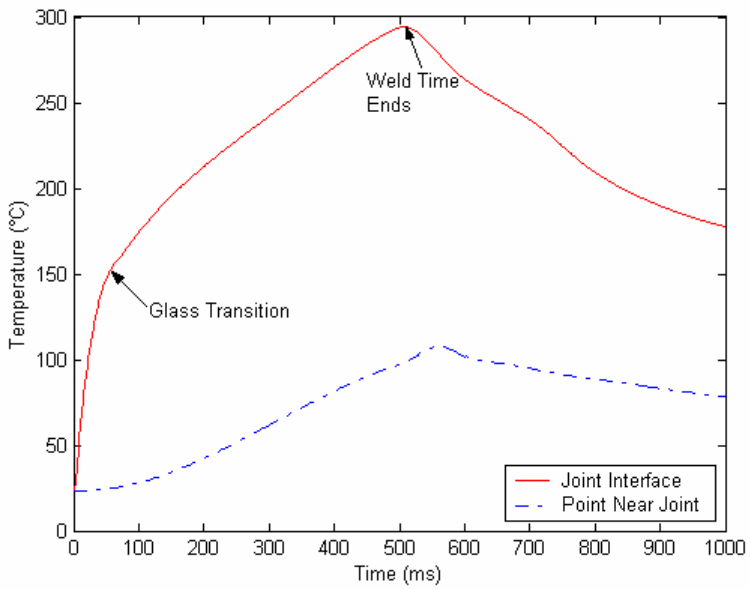

Fig. 4-27 Temperature variations for PC during the heating process

4.6 Validation of the Finite Element Model

For the developed finite element model using Eq. (4.54) and Eq. (4.55), in the present study, the Ansys 5.7 software package is used to simulate the heating process. The finite element model is meshed using Plane 77 [80-84], shown in Fig. 4-28. For Plane 77, the 8-node element has one degree of freedom, temperature, at each node, and has compatible temperature shapes, so it can meet the requirements of the simulation. For the boundary condition of this model, the top surface of the welding sample is in contact with the horn of the welding machine; the bottom surface and the side surface are in contact with the fixture; the other surfaces are in contact with air.

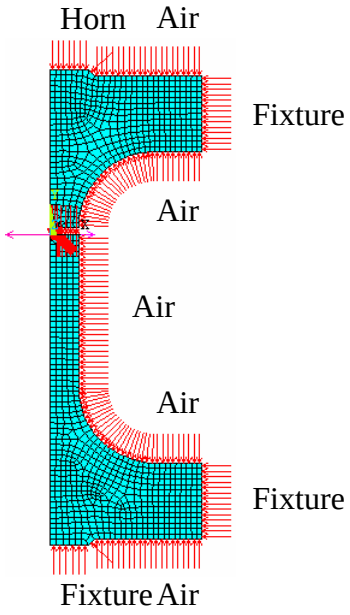

Fig. 4-28 Finite element model and boundary condition

The measured temperatures of the joint interface and the calculated heat generation rates of the non-joint interface parts for PP and PC will be used as the input load signals of the FE model to calculate the temperatures of the points near the joint with the step size 0.1 ms. The properties of PP and PC materials are listed in Table 4-3.

Table 4-3 Material properties of PP and PC materials

	PP	PC
Density	900 kg/m^3	1200 kg/m^3
Thermal Conductivity	0.2 $W/m^2 \cdot K$	0.22 $W/m^2 \cdot K$
Specific Heat	1930 $J/kg \cdot K$	1200 $J/kg \cdot K$
Convention Coefficient	5 $W/m^2 \cdot K$	5 $W/m^2 \cdot K$

Fig. 4-29 and Fig. 4-30 show the numerical results for the temperatures of the point near the joint for PP and PC respectively. The solid lines are the experimental results, and the dashed lines are the numerical results using the finite element model. As shown in the two figures, the numerical results are matched well with the experimental results. Therefore, the developed finite element model is effective to simulate the heating process. Furthermore, the numerical results also validate the experimental results of the loss compliance for PP and PC. From the finite element simulation, the temperature distributions in the welding samples during the heating process can also be derived from the model. Fig. 4-31 and Fig. 4-32 show the examples of temperature distributions for PP at 0.7 second and for PC at 0.5 second respectively, both of which are at the end of the weld time. Fig. 4-33 and Fig. 4-34 show the corresponding temperature distributions near to the joint interface for PP and PC respectively. Because the welding time of ultrasonic welding is very short, normally less than one second, no available thermal video system can record the dynamic temperature

distributions in such a short time. While, the dynamic temperature distributions are very important to study the heating behaviours during ultrasonic welding. Using this developed method, the dynamic temperature distributions are derived easily from the finite element model for the first time.

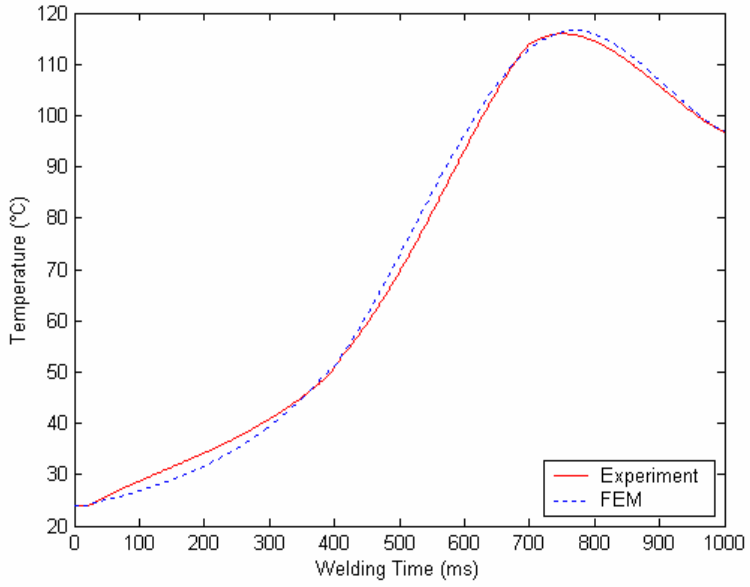

Fig. 4-29 Temperatures of the point near joint for PP material

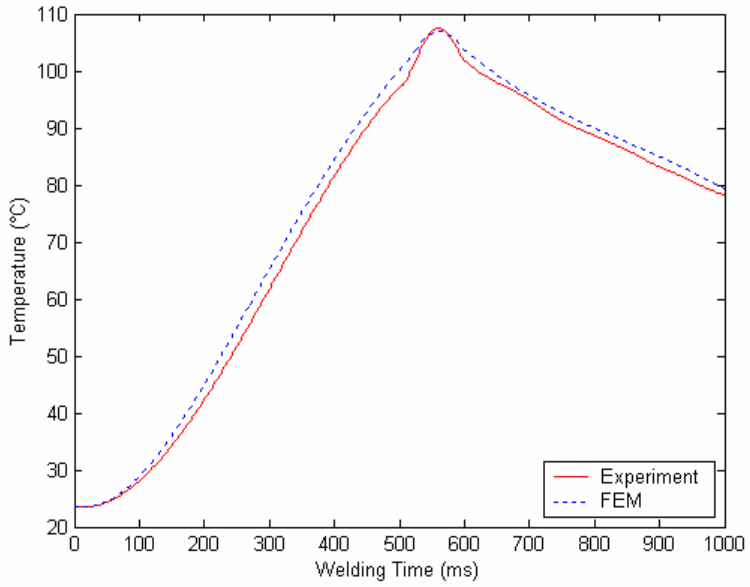

Fig. 4-30 Temperatures of the point near joint for PC material

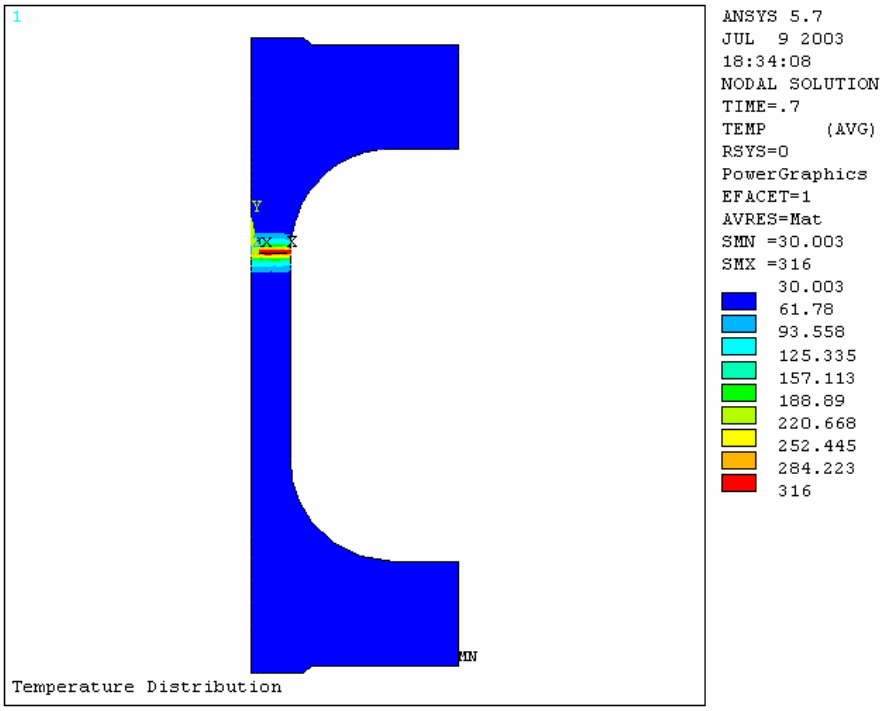

Fig. 4-31 Temperature distribution at 0.7 s for PP material

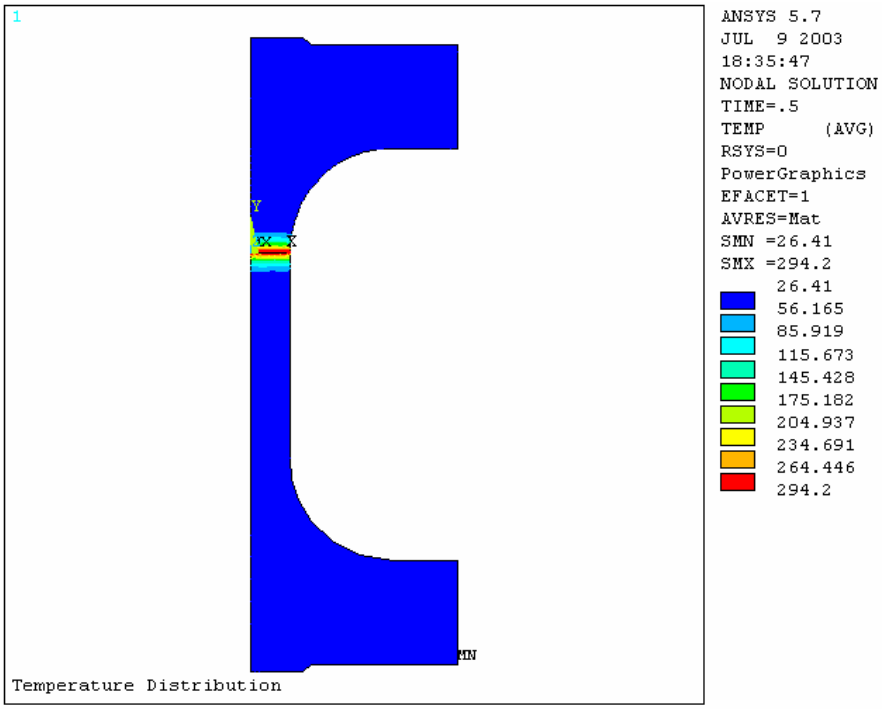

Fig. 4-32 Temperature distribution at 0.5 s for PC material

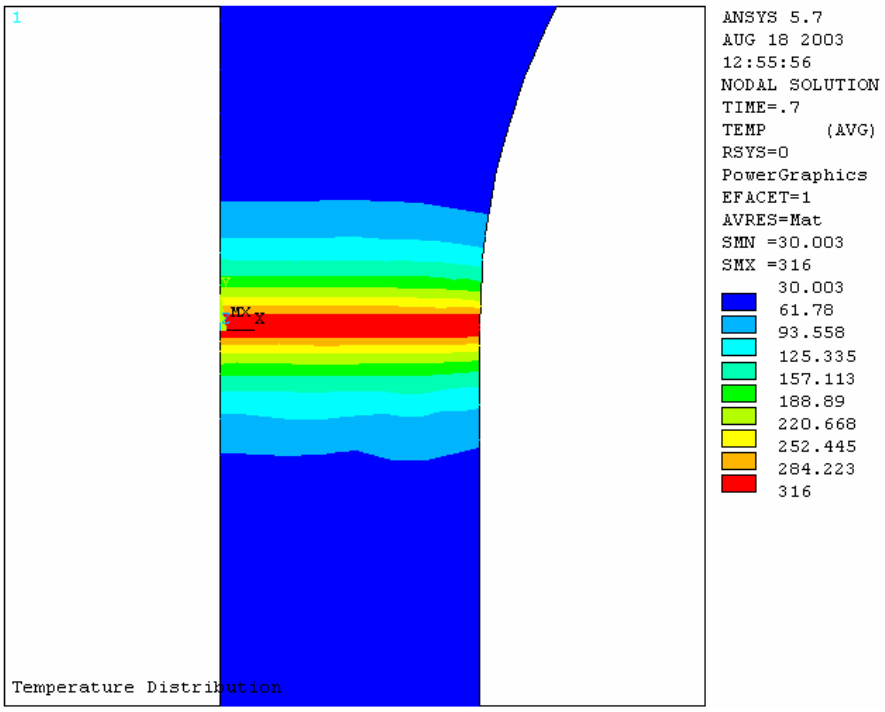

Fig. 4-33 Temperature distribution near to the joint interface at 0.7 s for PP

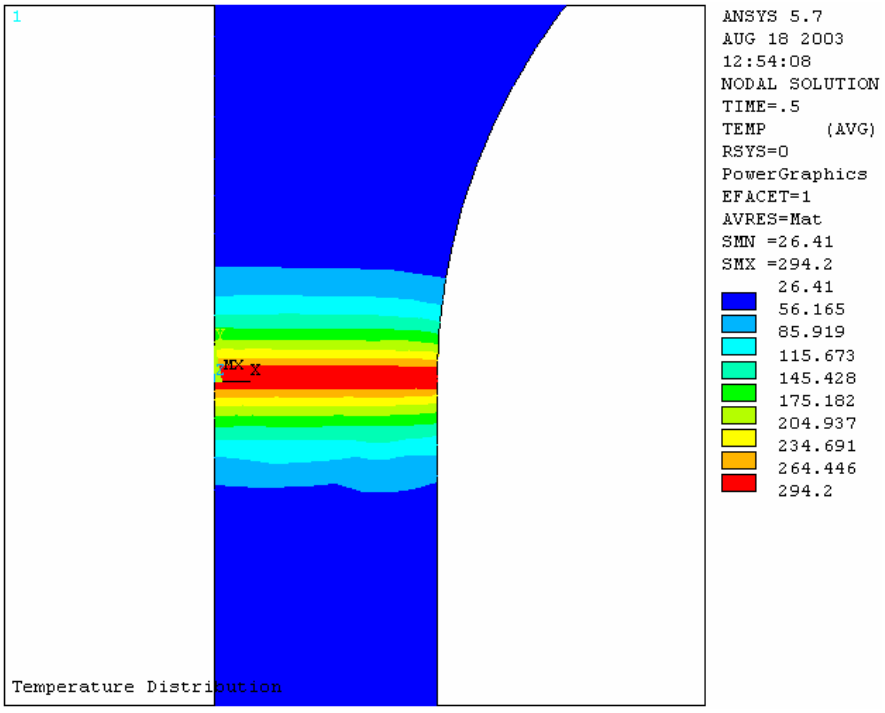

Fig. 4-34 Temperature distribution near to the joint interface at 0.5 s for PC

The total heating during the heating process can be divided into the volumetric heating of the non-joint interface parts and the localized heating at the joint interface. From the simulation results, the heating of the non-joint interface parts is the combination of the heat conduction from the joint interface and its own volumetric heating. For ultrasonic welding of thermoplastics, the thermal conductivities of materials are very small, and the weld times are also very short. Therefore, in the areas near to the joint interface, the heating of the non-joint interface parts mainly comes from the heat conduction of the joint interface, while the volumetric heating has less effect. In the areas far from the joint interface, the heating of the non-joint interface parts mainly comes from the volumetric heating, while the heat conduction has less effect.

Based on the simulation results, the boundary conditions are found that they do not affect the temperature distributions during the heating process in a significant way. In the areas far from the joint interface, the temperature increases very slowly. Thus, the temperatures of the surface are very low, and the heat loss can be nearly neglected. In the areas near to the joint interface, the convection coefficients of the air to thermoplastics are very small, and the weld times are very short, so the heat loss can also be nearly neglected. During the simulations, when we change the boundary conditions, the simulation results of the temperature distributions change very little. Therefore, the effects of the boundary conditions can be nearly neglected.

Chapter 5

Welding Mechanism in UWT

Based on the transduction matrix of the actuating mechanism, the output force and velocity can be detected by measuring the input voltage and current. The mechanical impedance can be derived from the force and velocity. Since ultrasonic welding system works at one single frequency, the force vs. displacement curve can be obtained. The mechanical impedance and the force vs. displacement curve reveal the mechanical behaviours of ultrasonic welding, which can be divided into four distinct phases. The temperatures of the joint interface, the SEM micrographs and the higher frequency signals can also reflect the phases.

A more detailed description about the welding mechanism of ultrasonic welding of thermoplastics is presented based on the above information. The results show that the mechanical impedance at the joint interface is the most characteristic variable of ultrasonic welding. The main machine settings are tested on deferent values to study their effects on the mechanical impedance. From the experimental results, it is found that the mechanical impedance can also reflect the main machine settings. Because the electrical impedance has the fixed relationship with the mechanical impedance, it can be used to monitor the weld quality of ultrasonic welding.

5.1 Mechanical Impedance during Ultrasonic Welding

The input voltage and current of the actuating mechanism can be easily measured with high sensitivities using a voltage probe system and a current probe system, which does not affect the welding process. Based on the transduction matrix of the actuating mechanism, the output force and velocity can be detected from the input voltage and current. The force and velocity are very important to study the welding process, which can reflect some important mechanical behaviours of the welding process.

For a typical welding process of PP material, Fig. 5-1 shows the amplitude of the detected force, and Fig. 5-2 shows the amplitude of the detected velocity. As shown in the two figures, ultrasonic welding can be divided into four phases based on the force and the velocity. In Phase I, the force and the velocity increase rapidly; then, in Phase II, the energy director begins to melt, so the force and the velocity are not stable; in Phase III, the energy director melts steadily, and the joint interface changes into face to face contact, so the force is stable, while the velocity continues to increase until the melting of the joint interface completes; in Phase IV, because some liquid will be squeezed out, the velocity begins to decrease, while the force is still stable. Therefore, the force and the velocity can reflect some phase changes during ultrasonic welding for PP material. The similar results are also applied to PC material. Fig. 5-3 and Fig. 5-4 show the amplitude of the detected force and the amplitude of the detected velocity respectively for PC material. In the four figures, Point '①' is the transition point from Phase I to Phase II; Point '②' is the transition point from Phase II to Phase III; Point '③' is the transition point from Phase III to Phase IV. The detailed description of each phase will be discussed later based on other information.

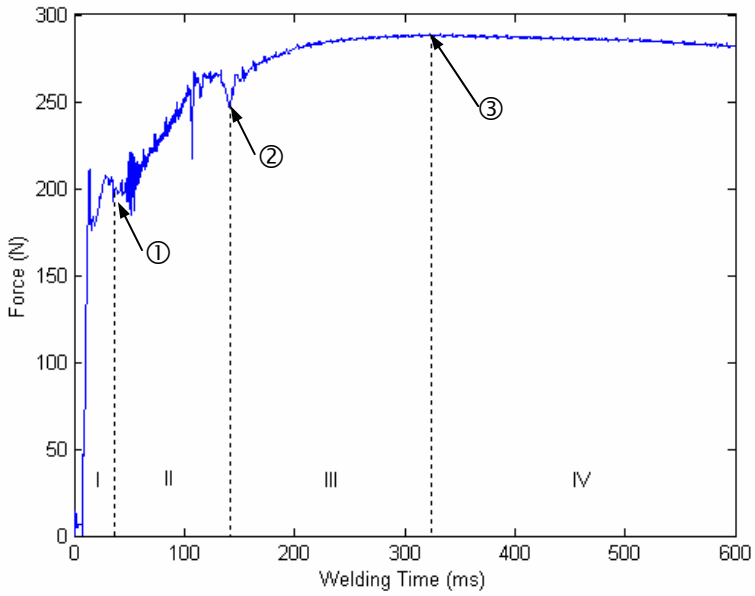

Fig. 5-1 Force amplitude for PP welding

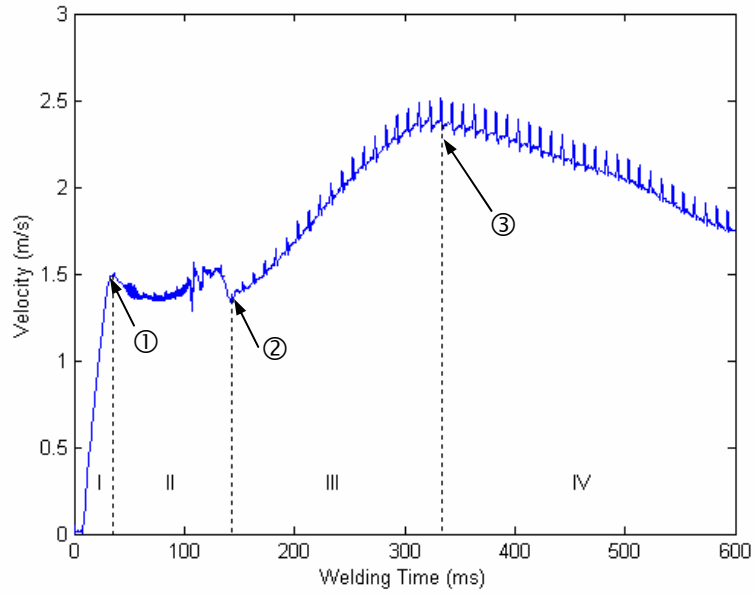

Fig. 5-2 Velocity amplitude for PP welding

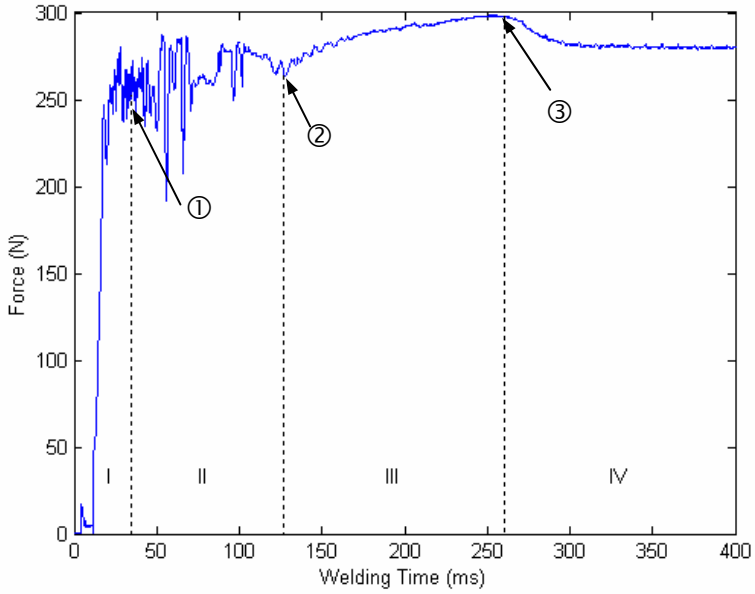

Fig. 5-3 Force amplitude for PC welding

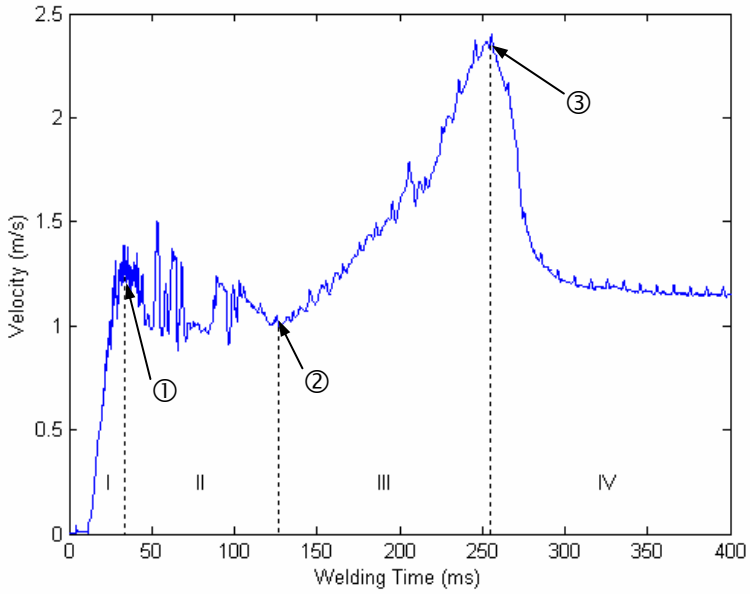

Fig. 5-4 Velocity amplitude for PC welding

Mechanical impedance is defined as the response of the velocity under the applied force, and determined by the mechanical properties of the welding process. Hence, the derived mechanical impedance from the force and velocity can reflect the mechanical behaviours of the welding process. Fig. 5-5 and Fig. 5-6 show the amplitudes of the mechanical impedance for PP and PC respectively. Because ultrasonic welding is very complicated, there is a lot of noise in the mechanical impedance. For this research, we only care about the main behaviours of ultrasonic welding. Therefore, a 30 kHz low-pass filter is used to cut off the noise. The filtered signals for the amplitudes of mechanical impedance are shown in Fig. 5-7 and Fig. 5-8 for PP and PC respectively. As shown in the two figures, the filtered signals can also reflect the main characteristics of the mechanical impedance. Therefore, they can be used as a substitute for the mechanical impedance to study ultrasonic welding.

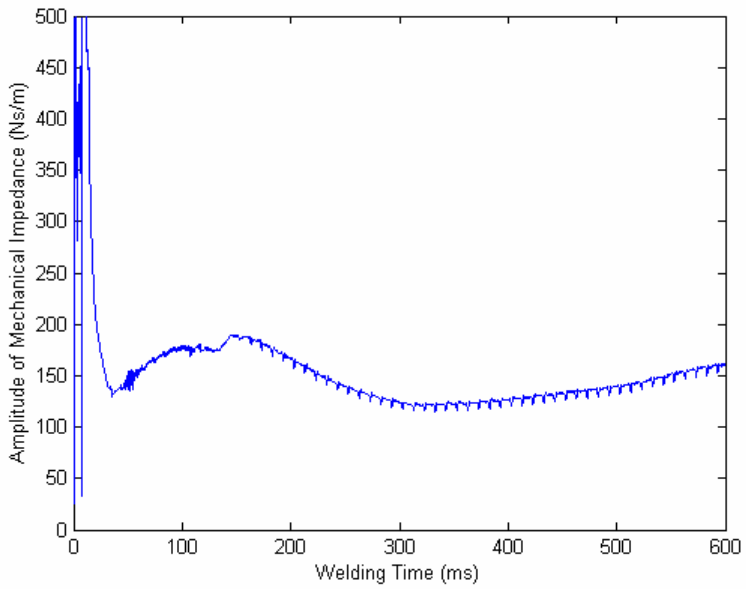

Fig. 5-5 Amplitude of mechanical impedance for PP

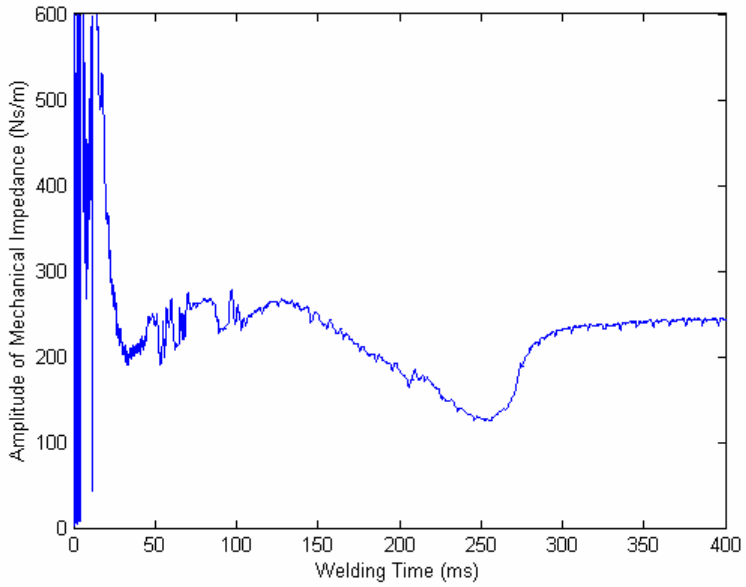

Fig. 5-6 Amplitude of mechanical impedance for PC

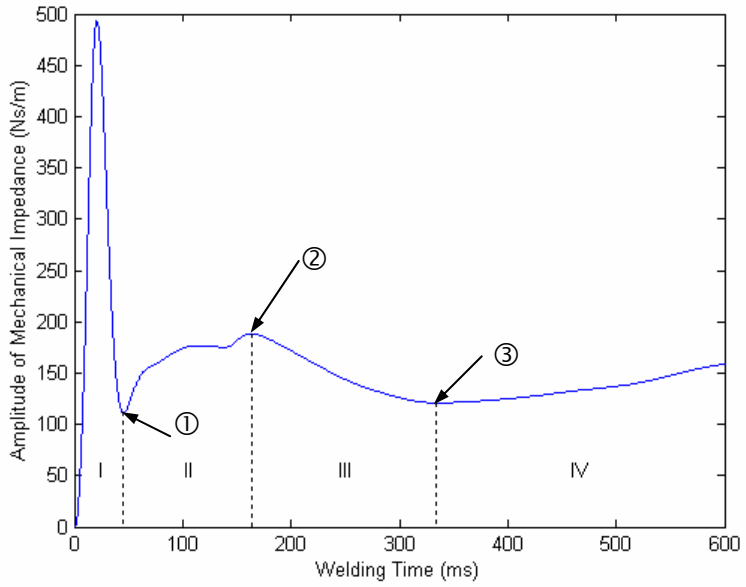

Fig. 5-7 Filtered amplitude of mechanical impedance for PP

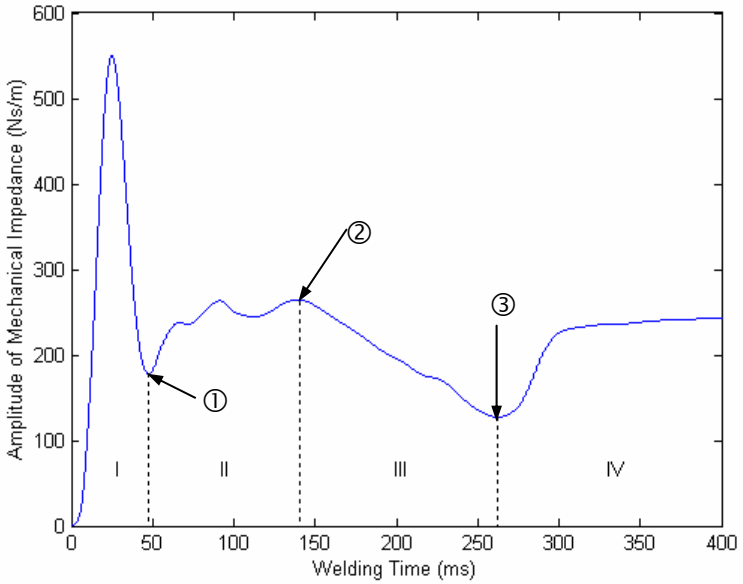

Fig. 5-8 Filtered amplitude of mechanical impedance for PC

As shown in Fig. 5-7 and Fig. 5-8, the four phases of ultrasonic welding in the force and the velocity can be reflected more clearly in the amplitudes of the mechanical impedance. In Phase I, the mechanical impedance increases first, then decreases. In Phase II, the mechanical impedance increases again with some small waves. In Phase III, the mechanical impedance decreases again. In Phase IV, the mechanical impedance increases finally. Because the ultrasonic welding machine stops working during the hold time, there are no voltage and current in this phase, so no mechanical impedance is obtained. However, according to the literature review, hold pressure and hold time have weak effects on the weld strength. Therefore, the hold phase is not important for ultrasonic welding. Even though the mechanical impedance can reflect the four phases of ultrasonic welding, the mechanism about each phase is not clear. In the next two sections, the force vs. displacement curve and the temperature of the joint interface will be used to study the behaviours of each phase.

5.2 Force vs. Displacement Curve during Ultrasonic Welding

Because ultrasonic welding system works at one single frequency, the corresponding displacement can also be derived from the velocity using Eq. (4.29). As we know, when the force is applied to the workpiece, the displacement is the response of the workpiece under the applied force. Hence, we can draw the force vs. displacement curve to describe the mechanical relationships between them, shown in Fig. 5-9 for PP material and in Fig. 5-10 for PC material.

According to the correspondence of the sampling points, the four phases of ultrasonic welding are indicted in the force vs. displacement curves for PP and PC materials. As we can see from the two figures, the mechanical behaviours in ultrasonic welding are shown clearly from force vs. displacement curves. Phase I is linear viscoelastic process first, then enter a yield process, and finally is a linear strain softening post-yield process. During Phase II, the force and the displacement are not stable. The force continues to go up, while the displacement has a little increase. In Phase III and Phase IV, the displacement continues to go up because the molten material is squeezed outside, while the force has little increase.

From Fig. 5-9 and Fig. 5-10, we cannot see clearly the transition Point '③' between Phase III and Phase IV in the force vs. displacement curves. However, if we plot Phase III and Phase IV separately, we can see Point '③', which is shown in Fig. 5-11 and Fig. 5-12. Therefore, the mechanical behaviours of the four phases during ultrasonic welding are revealed well by the force vs. displacement curve, which is a good tool to study the welding mechanism.

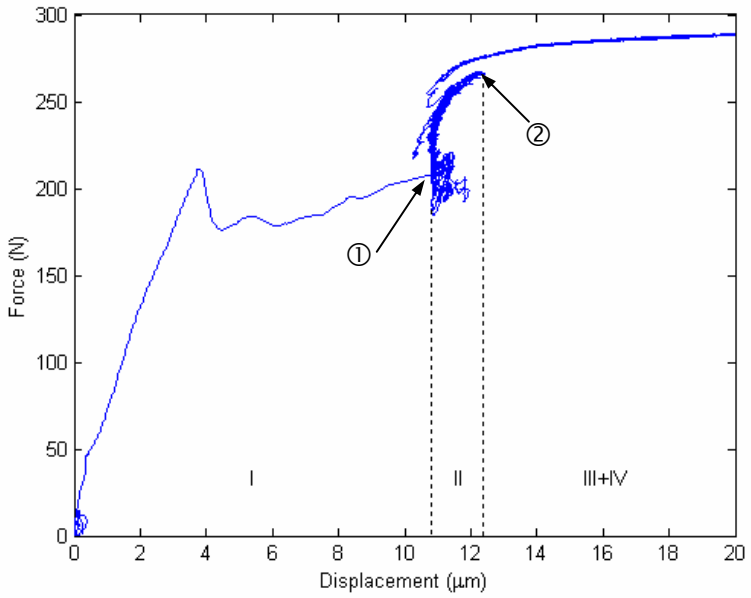

Fig. 5-9 Force vs. displacement curve for PP

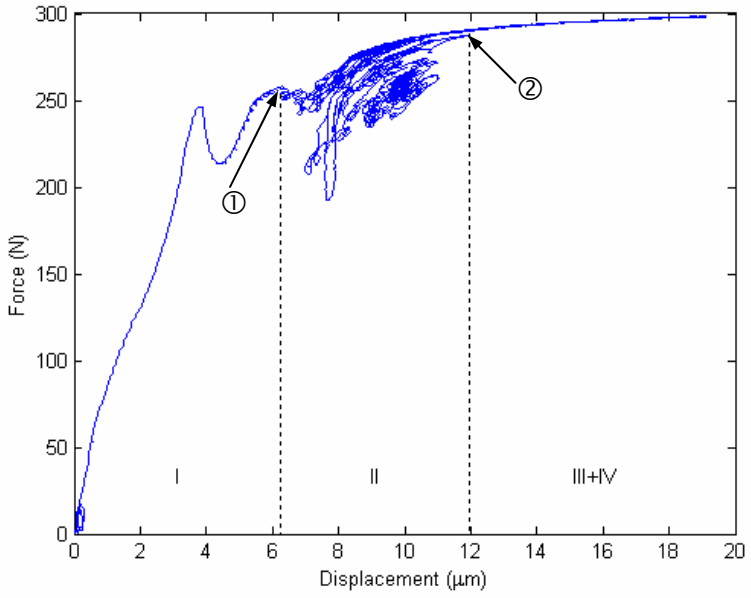

Fig. 5-10 Force vs. displacement curve for PC

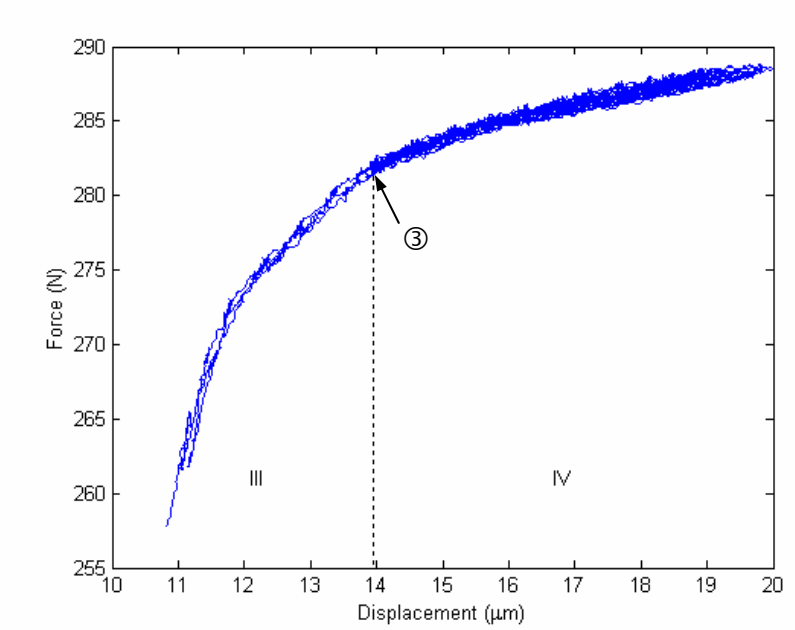

Fig. 5-11 Force vs. displacement curve for PP during Phase III and Phase IV

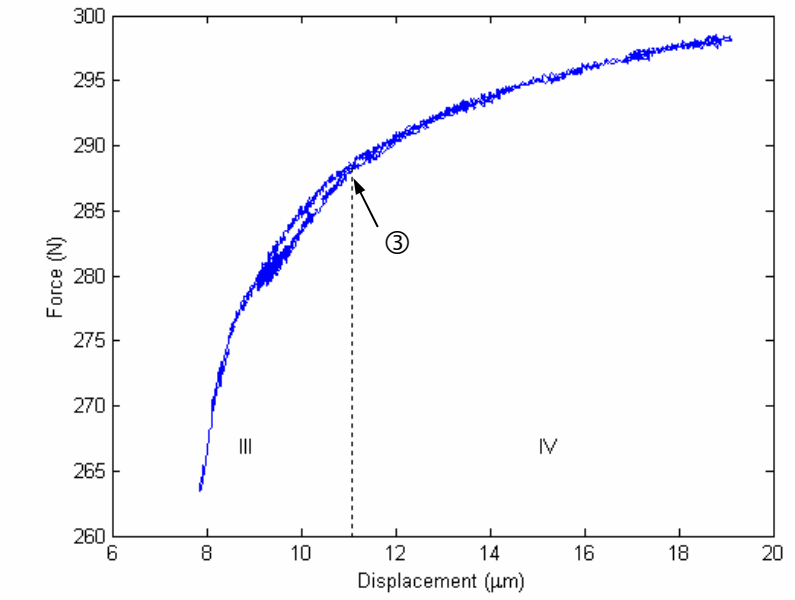

Fig. 5-12 Force vs. displacement curve for PC during Phase III and Phase IV

5.3 Temperature at Joint Interface during Ultrasonic Welding

As discussed in the last chapter, the temperature of the joint interface is a characteristic variable to reflect ultrasonic welding. The temperatures of the joint interface are shown in Fig. 5-13 and Fig. 5-14 for PP material and PC material respectively. According to the comparisons between the welding times, the phase changes during ultrasonic welding can be reflected in the temperatures. For PP material, the temperature can reflect Phase I and Phase IV clearly. In Fig. 5-13, Point '①' is the end of Phase I, and Point '③' is the beginning of Phase IV. The temperature cannot reflect Point '②' between Phase II and Phase III because the melting of the joint interface does not stop. For PC material, it does not have an obvious melting phase, so the temperature can only reflect Phase I. In Fig. 5-14, Point '①' is the end of Phase I. During Phase I, for PP and PC, the temperatures increase continuously, and they will reach T_m for PP (around 168°C) or T_g for PC (around 145°C) at the end. After Phase I, for PP, the temperature will stay a period for melting, and then increases again when the melting completes. While, for PC, the temperature increases all along, which cannot reflect the phase change well.

Even though the temperature of the joint interface can reflect some information of the phase changes during ultrasonic welding, it is not a good variable to reveal the welding process. Furthermore, there are three disadvantages to limit the wide usage of the temperature: 1) the thermocouples that are used to measure the temperatures should be embedded in the parts before welding, which is complicated and might affect the practical welding process; 2) the temperature of the joint interface changes much more quickly than that of the other areas. However, it cannot be measured accurately

because it is too difficult to put the thermocouples in the small energy director or the surface nearby it without any influence on the welding process; 3) the thermocouples are not sensitive enough under such high temperature change rates. Therefore, the temperature of the joint interface is not a good variable to detect the phase changes of ultrasonic welding in practice.

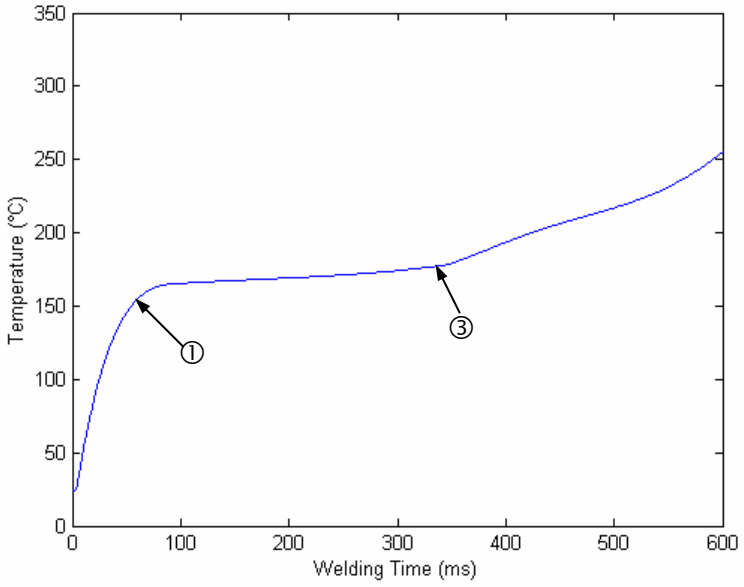

Fig. 5-13 Temperature of the joint interface for PP

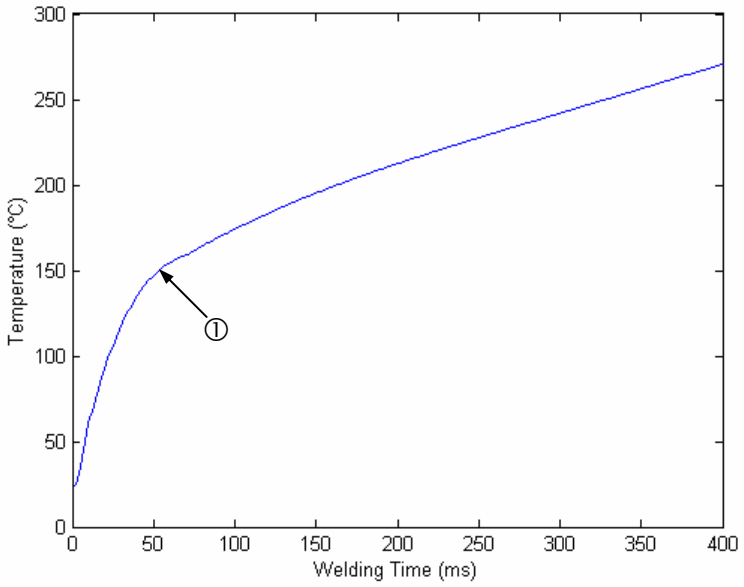

Fig. 5-14 Temperature of the joint interface for PC

5.4 Welding Mechanism in Ultrasonic Welding of Thermoplastics

Based on the above discussions, ultrasonic welding is divided into four phases according to the force, the velocity and the mechanical impedance. The force vs. displacement curve and the temperature at the joint interface can reveal some phase changes of the four phases. Referring to these pieces of information and the descriptions in the literature, a more accurate description of the welding mechanism in ultrasonic welding of thermoplastics is attempted. In the following, the details about each phase are discussed.

Phase I: Viscoelastic-plastic Phase For this phase, there are three distinct stages. During the first stage, the temperature of the joint interface is very low, so the energy director exhibits nearly linear viscoelastic behaviour. Heat is produced from the viscoelastic hehaviour, so the temperature of the joint interface increases, and the yield strength of the energy director decreases. When the applied force reaches the yield strength, the energy director begins to yield. The second stage is the yield process, where plastic deformation happens. There are two main factors affecting the stage: the temperature and the contact area of the joint interface. The increasing temperature is helpful to the yield process, while the increasing contact area increases the yield strength. Because the contact area changes more sharply than the temperature, after the yield process, it will enter the third stage: post-yield process. The third stage is a linear strain softening post-yield process. During this stage, the mechanical impedance decreases. The temperature of the joint interface increases continuously, and it will reach T_m for PP or T_g for PC in the end. Fig. 5-15 shows the original shape of the joint interface. Fig. 5-16 shows the shape of the joint interface after Phase I.

Fig. 5-15 SEM micrograph of original shape of the joint interface

Fig. 5-16 SEM micrograph of the joint interface after plastic deformation

Phase II: Energy Director Melting Phase When the temperature of the joint interface reaches T_m for PP or T_g for PC, the energy director begins to melt. During this phase, the energy director melts little by little. The molten energy director starts to flow after melting, so the contact area will increase, until a thin melting layer is formed, shown in Fig. 5-17. The force vs. displacement curve and the mechanical impedance change drastically because of the melting of the energy director. Comparing PP with PC, PP

has a more ordered structure, so the mechanical impedance of PP changes more softly, which is also reflected in the force vs. displacement curve.

Fig. 5-17 SEM micrograph of the joint interface after energy director melting

There are two factors affecting the mechanical impedance. One is the increase of the contact area of the energy director, which causes the increase of the mechanical impedance. The other is the increasing temperature, which decreases the mechanical impedance. Between them, the contact area is the main factor. Therefore, the main trend of the mechanical impedance is increasing. However, the energy director melting process is not continuous. During the process, there is an equilibrium point at first. After the equilibrium point, the material at the tip of the energy director softens and melts. When the molten material is squeezed out, it will reach a new equilibrium point. The procedure is repeated till the melting layer is formed. The small waves of the mechanical impedance reflect the discontinuousity of the energy director melting process. After Phase II, the contact area of the joint interface does not change much, so the mechanical impedance does not change drastically after this point, and it will enter a more stable decreasing period.

Phase III: Melting Completing Phase When the melting layer is formed, the melting does not completes because there are still some small gaps between the upper part and the lower part along the weld line. During this phase, it will take some time to melt the melting layer and the contact faces of the upper and lower parts. The molten material fills in the gaps and wets the weld line, and then, the melting of the joint interface completes. For PP, as shown in Fig. 5-13, at about 330 ms, the temperature does not keep at the melting temperature of PP, and begins to increase sharply, which means the melting completes and the coupling happens. Once the melting layer is formed, the contact area of the joint interface does not change much. The increasing temperatures of the upper and lower parts decrease the mechanical impedance during this phase. During Phase III, the melting of the joint interface has not completed, the temperature of the joint interface for PP still stays at T_m of PP. For PC, the temperature increases continuously, which also causes the mechanical impedance decrease. Therefore, the transition of the mechanical impedance for PP is smoother than that for PC.

Phase IV: Upper & Lower Parts Coupling Phase When the melting of the joint interface completes, intermolecular diffusion and entanglement are needed to couple the upper and lower parts together to form a strong weld strength. Autohesion is the phenomenon describing the intermolecular diffusion and chain entanglement across a thermoplastic polymer interface to form a strong bond (See Fig. 5-18). Autohesion relies on chain entanglement and secondary bonds for polymer chains of similar materials. The diffusion of long polymer chains across the bond interface and entanglement of these chains gives the ultrasonic bond its strength. The diffusion is complete when the interface is no longer discernible from the bulk. During this phase, some liquid is squeezed out. The squeeze and the autohesion will increase the

mechanical impedance. The shape of the joint interface after Phase IV is shown in Fig. 5-19, where the welding process completes successfully.

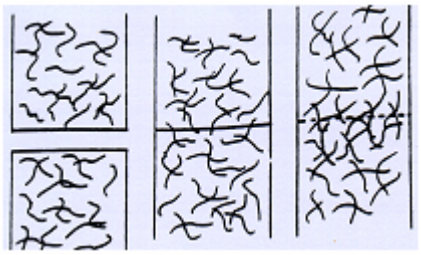

Fig. 5-18 Intermolecular diffusion process for a polymer-to-polymer interface [17]

Fig. 5-19 SEM micrograph of the joint interface after coupling

Compared with the temperature of the joint interface and the force vs. displacement curve, the mechanical impedance is the best variable to reflect the main mechanical behaviours of the welding process because it is sensitive and easy to measure, and can reflect the four phases clearly for both PP and PC. Compared with Tolunay and Tateishi's results in the literature, the welding mechanism can also be better revealed by the mechanical impedance. Therefore, the mechanical impedance at the joint interface is the most characteristic variable of ultrasonic welding.

The phenomena observed by Benatar and Land are easy to understand from the mechanical impedance changes. The first decrease of the gap between the two parts for a short time is due to the plastic deformation in Phase I. Remaining constant is because of the melting of the energy director in Phase II. The final decrease is because some liquid at the joint interface is squeezed out in Phase IV.

There are some higher frequency harmonic noises in the input voltage and current, shown in Fig. 3-12. The higher frequency signals can also reflect some phase changes of ultrasonic welding. Fig. 5-20 and Fig. 5-21 show the higher frequency signals for PP and PC respectively. According to the transition points shown in the two figures, the four phases in the force vs. displacement curves are also shown in the higher frequency signals.

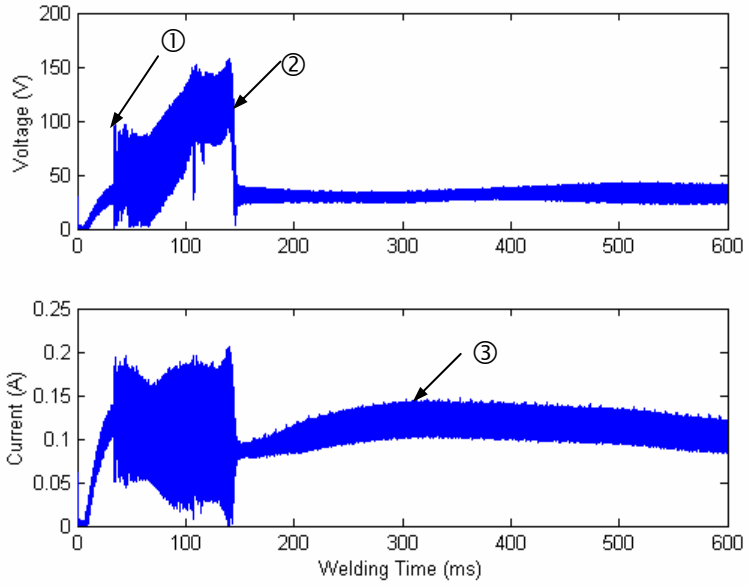

Fig. 5-20 Higher frequency signals for PP

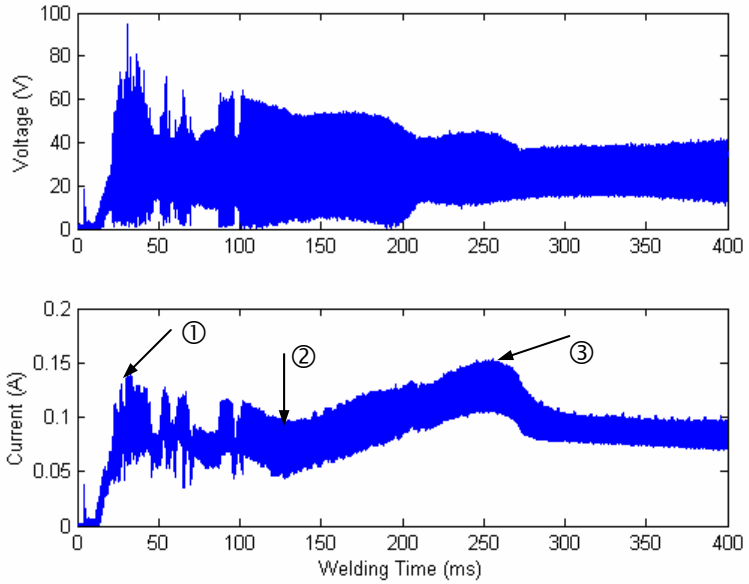

Fig. 5-21 Higher frequency signals for PC

5.5 Effects of Vibration Amplitude and Static Pressure

The mechanical impedance is the most characteristic variable of ultrasonic welding, which can reflect the welding conditions of the welding process. In this section, we will check the influences of the main machine settings, vibration amplitude and static pressure, on the mechanical impedance via experiments for PP material and PC material. When evaluating one machine setting at different levels, all the other machine settings are kept constant. The corresponding tensile strengths are also tested to investigate the effects of the machine settings on the tensile strengths. Fig. 5-22 shows the effects of the vibration amplitude (30% ~ 70%) on the mechanical impedance for PP material. Fig. 5-23 shows the effects of the vibration amplitude on the corresponding tensile strength for PP material. Fig. 5-24 shows the effects of the vibration amplitude (20% ~ 60%) on the mechanical impedance for PC material. Fig. 5-25 shows the effects of the vibration amplitude on the corresponding tensile strength

for PC material. Fig. 5-26 shows the effects the static pressure (40 PSI ~ 80 PSI) on the mechanical impedance for PP material. Fig. 5-27 shows the effects of the static pressure on the corresponding tensile strength for PP material. Fig. 5-28 shows the effects of the static pressure (30 PSI ~ 70 PSI) on the mechanical impedance for PC material. Fig. 5-29 shows the effects of the static pressure on the corresponding tensile strength for PC material.

Comparing these curves under the different settings, the mechanical impedance can reflect the variations of vibration amplitude and static pressure well. Both vibration amplitude and static pressure have significant effects on the mechanical impedance. For the transition points of the four phases in the mechanical impedance, because Phase I need very short time in the whole welding time, the increase of vibration amplitude or static pressure does not affect the '①' transition point much; after Phase I, the increase of vibration amplitude causes the more power generated, and the increase of static pressure causes the more flow of the liquid at the joint interface, so the '②' transition point and the '③' transition point are forward with the increase of vibration amplitude or static pressure, which means the time for phase change decreases. Therefore, the mechanical impedance changes faster with the increase of the setting. Given the same weld time, for the higher setting, the first three phases of the welding process complete in less time, so the Phase IV will have more time. As we know, the intermolecular diffusion and entanglement in Phase IV is important to form a strong weld strength. With the more time of Phase IV, it will have a better intermolecular diffusion of long polymer chains across the bond interface and an entanglement of these chains. So the joint strength increases with the settings in their lower values.

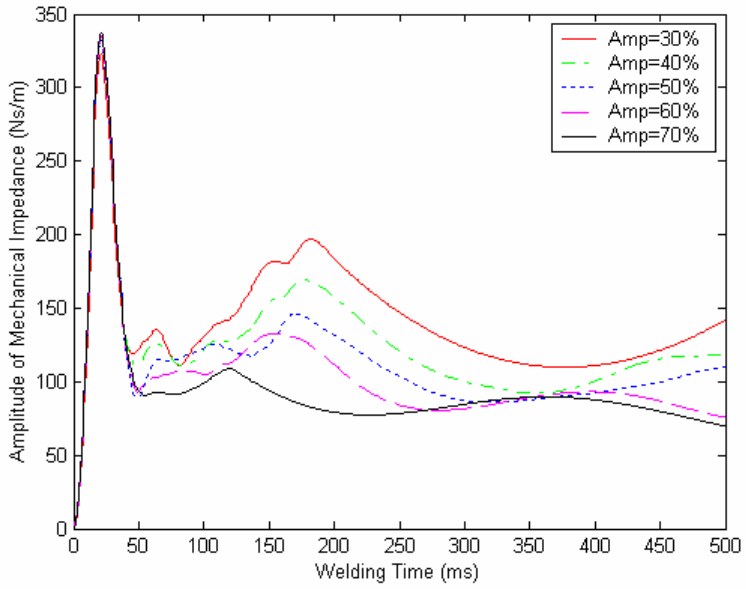

Fig. 5-22 Mechanical impedances under deferent amplitudes for PP

(Pressure 35 PSI, Trigger Force 10 PSI, Weld Time 500 ms)

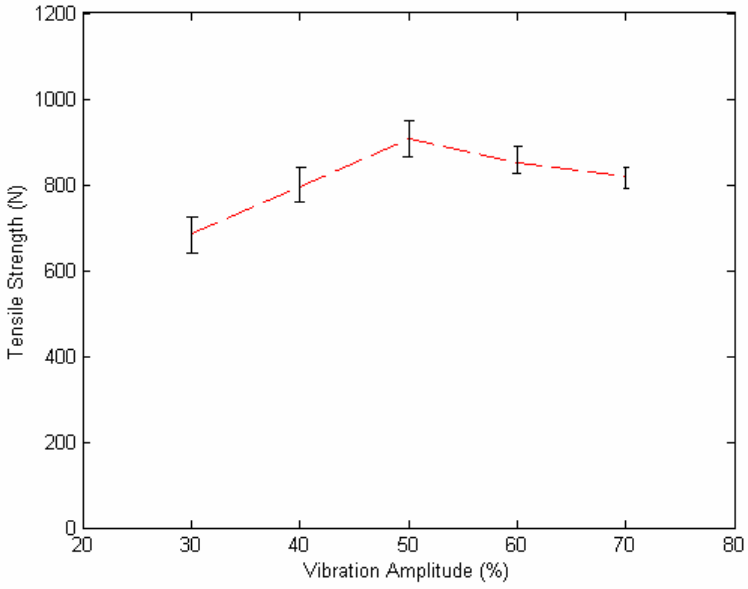

Fig. 5-23 Tensile strength under deferent amplitudes for PP

(Pressure 35 PSI, Trigger Force 10 PSI, Weld Time 500 ms)

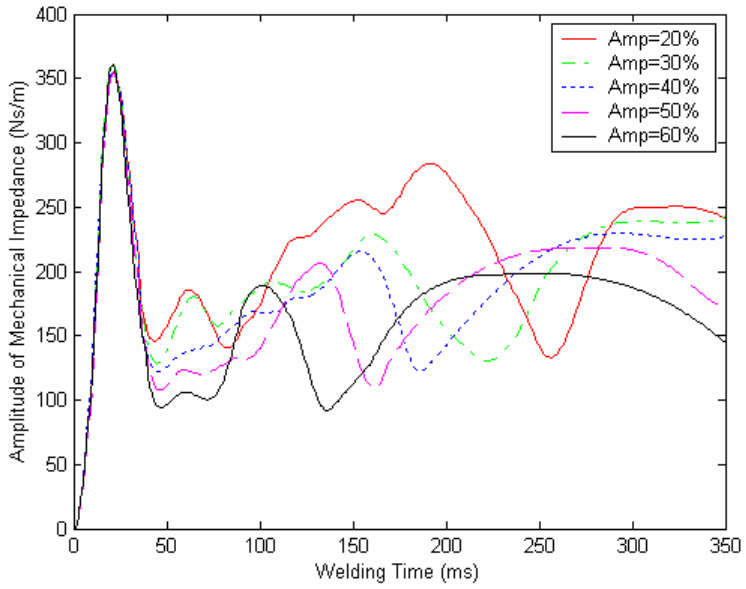

Fig. 5-24 Mechanical impedance under deferent amplitudes for PC

(Pressure 35 PSI, Trigger Force 10 PSI, Weld Time 350 ms)

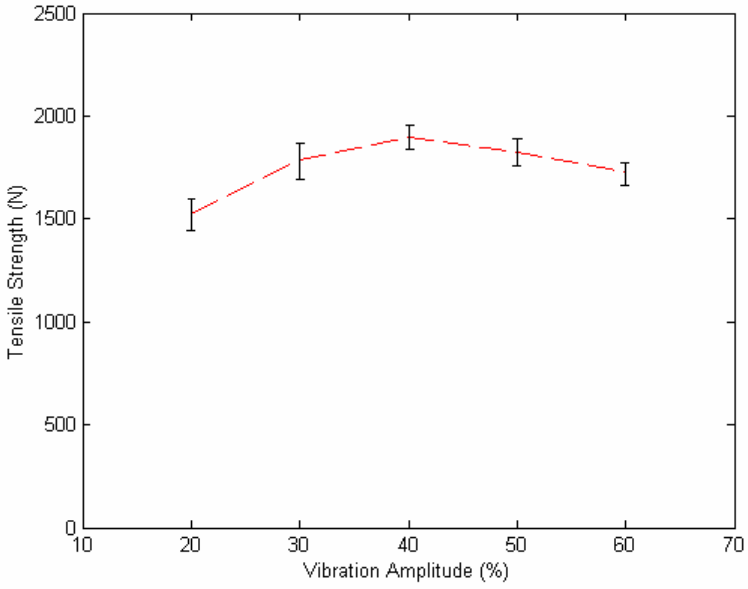

Fig. 5-25 Tensile strength under deferent amplitudes for PC

(Pressure 35 PSI, Trigger Force 10 PSI, Weld Time 350 ms)

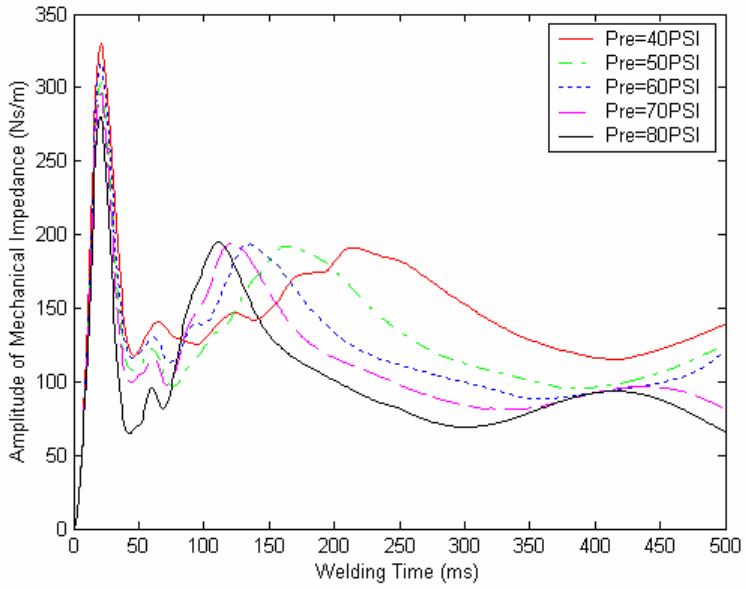

Fig. 5-26 Mechanical impedance under deferent pressures for PP

(Amplitude 35%, Trigger Force 10 PSI, Weld Time 500 ms)

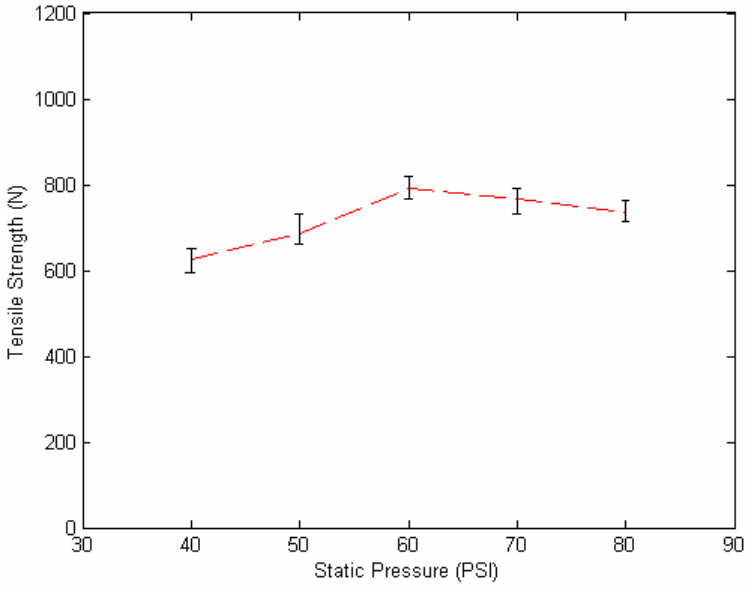

Fig. 5-27 Tensile strength under deferent pressures for PP

(Amplitude 35%, Trigger Force 10 PSI, Weld Time 500 ms)

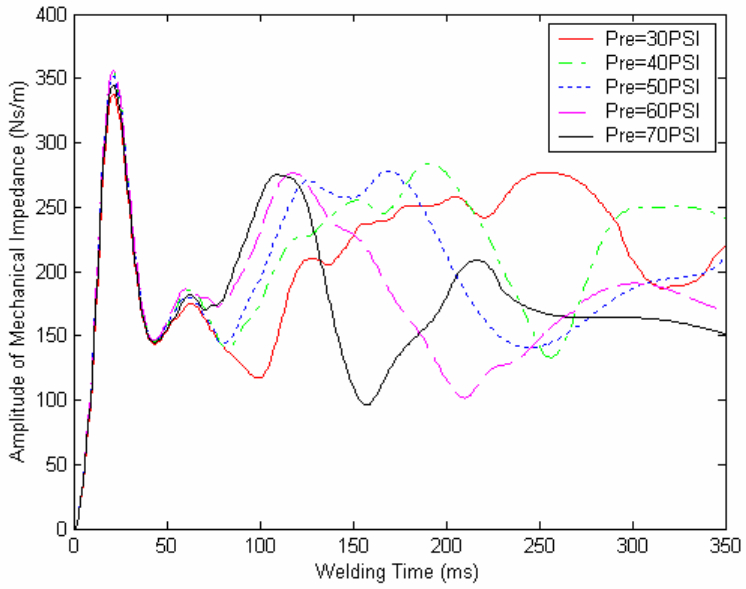

Fig. 5-28 Mechanical impedance under deferent pressures for PC

(Amplitude 25%, Trigger Force 10 PSI, Weld Time 350 ms)

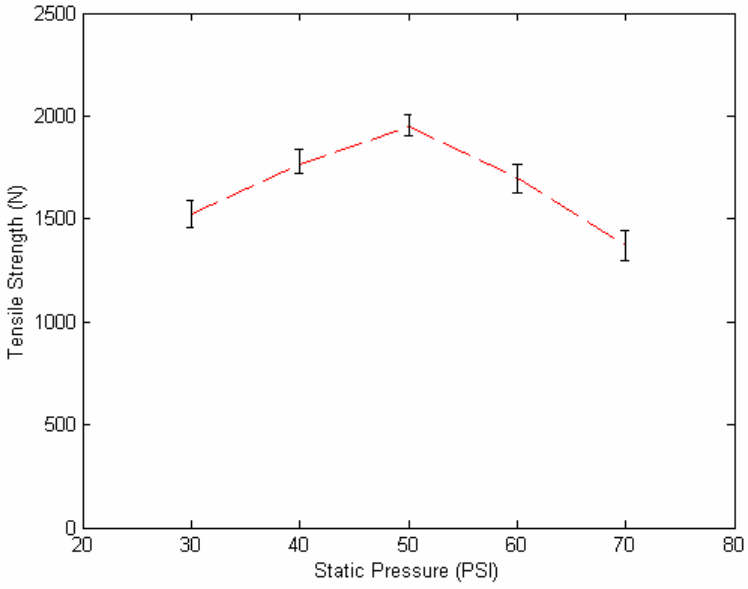

Fig. 5-29 Tensile strength under deferent pressures for PC

(Amplitude 25%, Trigger Force 10 PSI, Weld Time 350 ms)

In Chapter 1, it has been mentioned there is an optimal range for the setting. Beyond the optimal range, the welding process will enter another phase after Phase IV, called as the over-welding phase. In the over-welding phase, much liquid in the joint interface will be squeezed out, shown in Fig. 5-30, and less liquid can have autohesion to form a joint strength, which will make a bad joint. Therefore, the joint strength increases with the settings first, and then decreases with settings after the optimal range of the settings, which agrees with Shi's results [85]. The mechanical impedance decreases during the over-welding phase. To optimize the welding process, the welding process must have the optimal four phases and cannot let the over-welding phase happen. It is reasonable that the mechanical impedance can be regarded as a variable to identify the welding parameters. Therefore, the mechanical impedance can reflect the characteristics of ultrasonic welding and welding parameters.

Fig. 5-30 SEM micrograph of the joint interface after over-welding

In addition, for PP material and PC material, as we know, PP material belongs to semi-crystalline, while PC material belongs to amorphous. PP material has more orderly molecular arrangement, so the mechanical impedance for PP material is more stable than that of PC. For the above discussions, the effects of vibration amplitude and static pressure on PP material are more significant than that on PC material.

5.6 Electrical Impedance during Ultrasonic Welding

Because the mechanical impedance is derived from the input electrical impedance, and the transduction matrix is constant for a given ultrasonic welding system, the amplitude of the electrical impedance should also be a characteristic variable of ultrasonic welding. Since it is very easy to be calculated from the measured voltage and current, it can be used to monitor the weld quality of ultrasonic welding. Fig. 5-31 and Fig. 5-32 show the electrical impedances for PP and PC respectively during typical good welding process. As shown in the two figures, the electrical impedance also reflects the four distinct phases of ultrasonic welding. Fig. 5-33 and Fig. 5-34 show the electrical impedances for PP and PC respectively during typical bad welding process, which cannot produce a good weld and do not have the distinct four phases of ultrasonic welding.

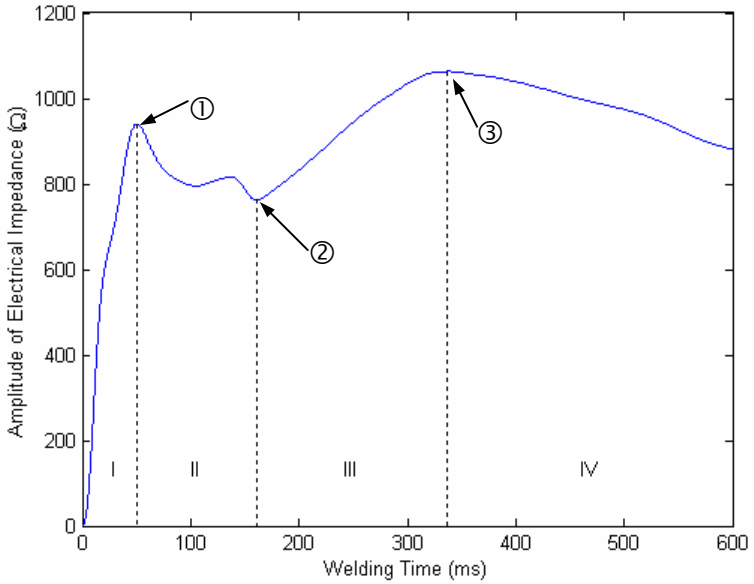

Fig. 5-31 Electrical impedance for typical good PP welding

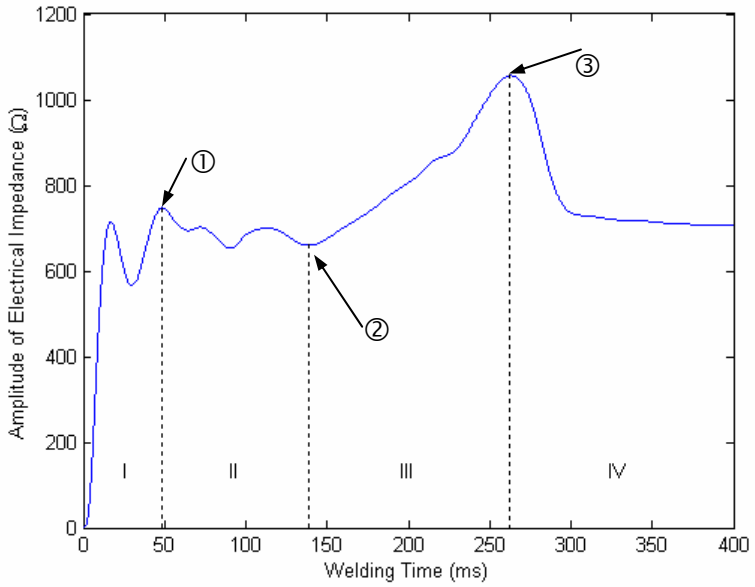

Fig. 5-32 Electrical impedance for typical good PC welding

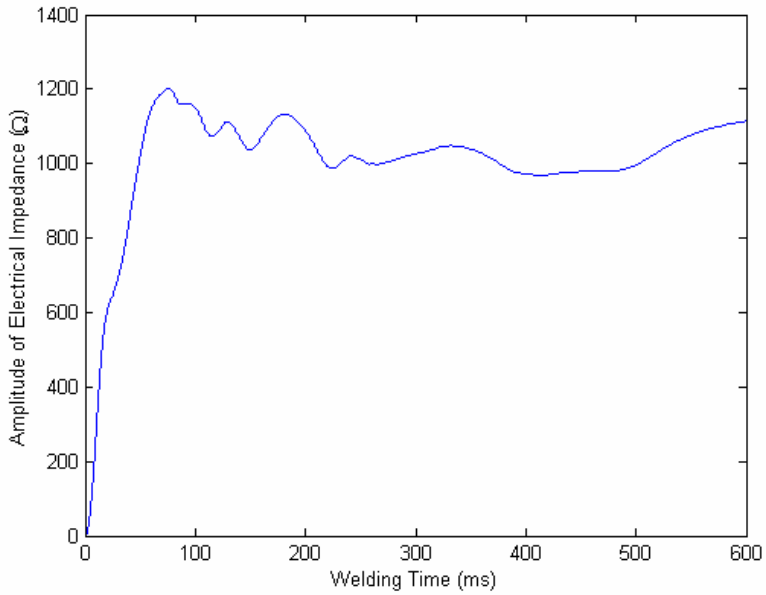

Fig. 5-33 Electrical impedance for typical bad PP welding

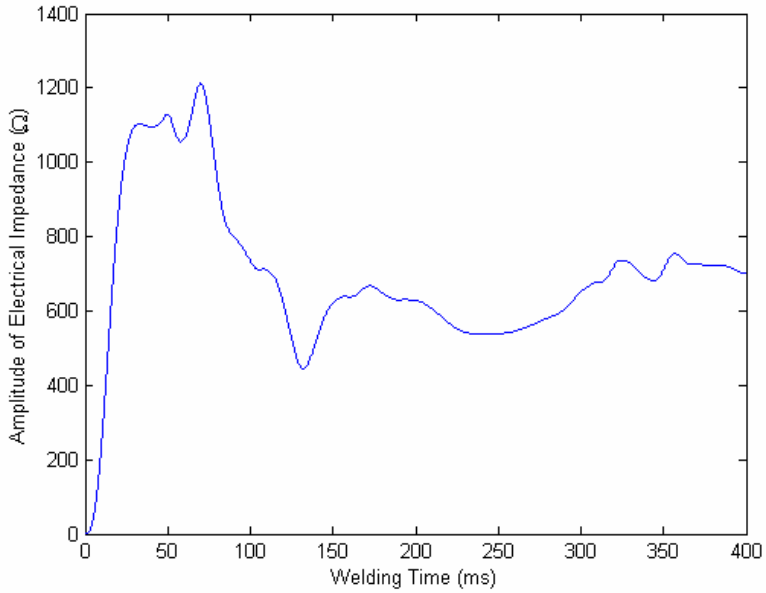

Fig. 5-34 Electrical impedance for typical bad PC welding

For this application, Artificial Intelligence is introduced for statistical calculation. In order to reduce the input vector and render the features more suitable for the decision process, we sample the electrical impedance at a fixed frequency so that we can get the curve shape of the input electrical impedance that is one of the most important characteristics. We get 60 values from the impedance curve of PP, shown in Fig. 5-35, and 40 values from the impedance curve of PC, shown in Fig. 5-36. Compared Fig. 5-35, Fig. 5-36 with Fig. 5-31, Fig. 5-32, the extracted features should be capable of representing the original waveform of the electrical impedance.

One of the newest technologies emerging within Artificial Intelligence is neural network. Neural network, also known as machine learning algorithms, is trained to perform complex functions in various fields of applications like pattern recognition, which requires knowledge that is difficult to specify but is available in the form of

examples. Luan [31] and Wendy Ang [86] used neural network to predict the machine setting and weld quality from the electrical impedance.

The neural network constructed for machine setting recognition contains 4 layers. The first layer, input layer, consists of inputs are the selected features. The two hidden layers have 30 and 10 nodes and the output layer gives the classification of the machine settings. Hence, the impedance value and the classified value form input/target pairs. Fig. 5-37 shows the result of the machine setting recognition. The neural network construction used for weld quality prediction is similar to that of the machine setting recognition. Fig. 5-38 shows the result of prediction of weld tensile strength. The results show that the unique characteristics of the electrical impedance are the features that can be used to train the neural network for machine setting recognition and weld strength prediction. Therefore, the electrical impedance is also the characteristic variable for ultrasonic welding.

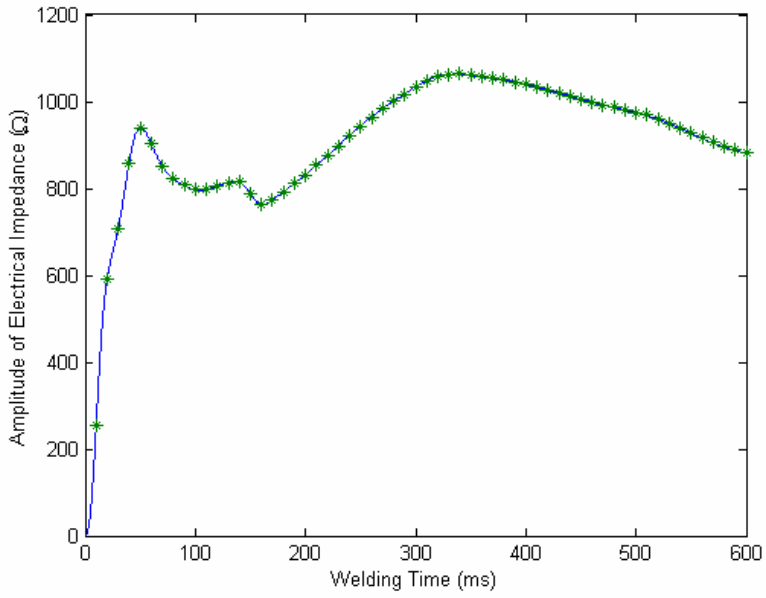

Fig. 5-35 Feature extraction from electrical impedance for typical good PP welding

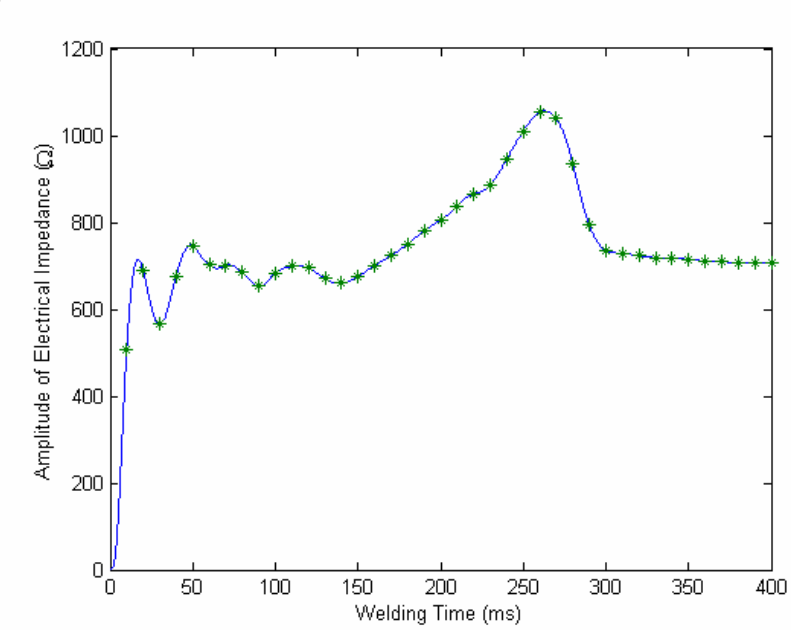

Fig. 5-36 Feature extraction from electrical impedance for typical good PC welding

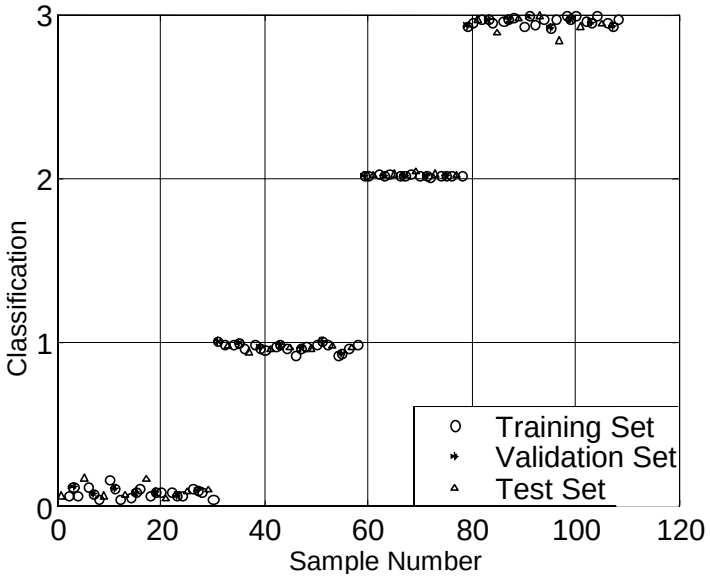

Fig. 5-37 Machine setting recognition [86]

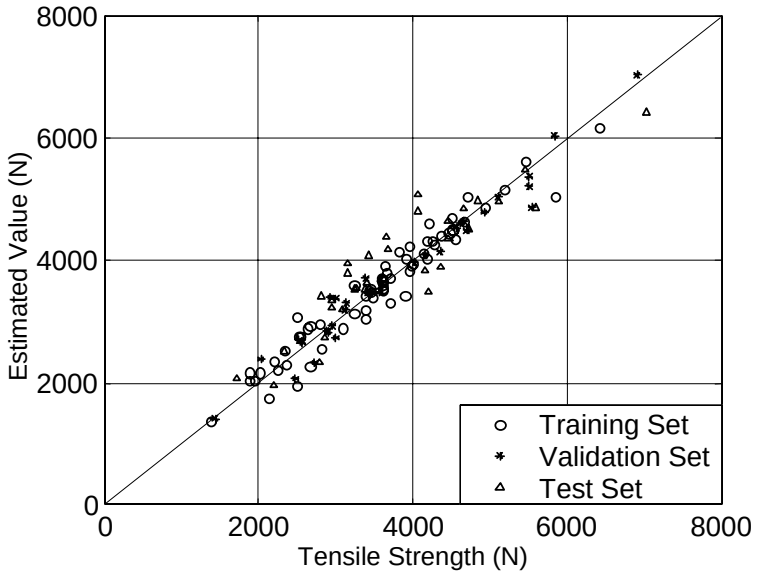

Fig. 5-38 Prediction of weld tensile strength [86]

Chapter 6

Mechanical Behaviours of Thermoplastics during UW

From the last chapter, ultrasonic welding can be divided into four phases: viscoelastic-plastic phase (Phase I), energy director melting phase (Phase II), melting completing phase (Phase III), and upper and lower parts coupling phase (Phase IV). In this chapter, based on viscoelasticity and plasticity and liquid property of the materials, the mechanical behaviours of thermoplastics during each phase of ultrasonic welding are modeled through optimization to minimize the discrepancies between the mechanical relationships obtained from the models and the measurement.

Three models, viscoelastic-plastic model, melting model and coupling model, are developed according to the phases of ultrasonic welding. The overall model is integrated based on time varying. The mechanical relationships calculated using the overall model are matched well with the experimental results, so the overall model is effective to model the mechanical behaviours of thermoplastics during ultrasonic welding of thermoplastics. The parameters of the models can further reveal the detailed characteristics of ultrasonic welding. Through these models, a tool was obtained for better understanding the welding process.

6.1 Introduction of Viscoelasticity and Plasticity of Thermoplastics

Thermoplastics are made up of long molecules, and each molecule contains a chain of atoms held together by covalent bonds. Thermoplastics are produced through a process known as polymerization whereby monomer molecules react together chemically to form either linear chains or a three-dimensional network of polymer chains. The main characteristic of the chain is that the chemical bonding is strong and directional along the chains, but they are only bonded sideways by weak secondary van der Waals bonding or occasionally with hydrogen bonding.

Elastic deformation poses a limit on the motion of the atoms. All atoms remain in equilibrium positions determined by internal energy. In terms of the potential energy surface, the deformation remains elastic, as long as the molecules do not move out of their valleys. Elastic deformation is totally recoverable, and material has perfect memory of its original shape.

Viscous deformation occurs when an atom on the potential surface exchanges its position with neighboring atom or with vacancy because of thermally activated atomic jumps biased in direction of applied stress. Net movement of atoms is the viscous flow. Viscous deformation is not recoverable, and it stops when stress is equal to zero. During viscous deformation, no energy is stored, and work of deformation is totally dissipated. Viscosity η is related to temperature T by Arrhenius-type equation [87]:

$$\eta = A_m e^{-E_a / R_g T} \tag{6.1}$$

where A_m is the constant related to molecular motion, and R_g is the gas constant

8.314 J mol^{-1} K^{-1}. E_a is the activation energy for viscous flow, and it is determined mainly by localized segmental motion of polymer chains.

The main mechanical behaviours of thermoplastics can be thought of as being somewhere between that of elastic solids and viscous liquids. At low temperatures and high rates of strain, they display elastic behaviour, whereas at high temperatures and low rates of strain they behave in a viscous manner, flowing like a liquid. Thermoplastics are therefore termed viscoelastic as they display aspects of both viscous and elastic types of behaviour.

Plastic deformation begins where elastic deformation ends, and it involves large scale cooperative motions of atoms by means of defects. During plastic deformation, some molecular chain segments will change over from low-energy conformations to high-energy conformations. During plastic deformation, no strain energy is stored, and work of deformation is transformed into heat. The average amount of internal energy in a material is proportional to absolute temperature. The fraction of atoms with plastic capability increases rapidly with temperature.

The general stress-strain curve for a thermoplastic demonstrating various elements of tensile behaviour is shown in Fig. 6-1 [87]. Initially the modulus is high, until a point is reached where the thermoplastic yields. Prior to the yield point, the strain is reversible. At the yield point, enough stress has been applied to cause the molecules to untangle and flow over one another, and further strain is irreversible. Eventually the sample breaks. The behavior of the thermoplastic beyond the yield point depends to a large degree on the thermoplastic's initial morphology. If the thermoplastic is

amorhpus or of low crystallinity, application of stress may increase the crystallinity, which in turn increases the modulus. This is the principle behind drawing. Highly crystalline thermoplastics exhibit little change in morphology on drawing and break soon after the yield point.

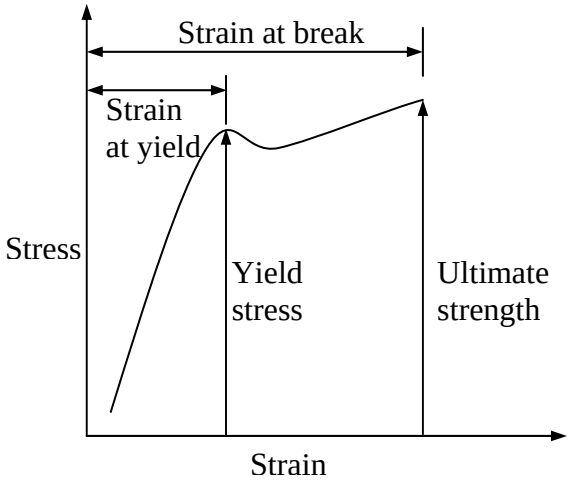

Fig. 6-1 General tensile stress-strain curve for a typical thermoplastic [87]

6.2 Modeling of Phase I (Viscoelastic-plastic Phase)

6.2.1 General Description of Phase I

Fig. 6-2 and Fig. 6-4 show the force vs. displacement curves for PP and PC respectively during Phase I. As shown in the two curves, there are two yield points: upper yield point and lower yield point. According to the two yield points, Phase I is divided into three stages: pre-yield stage, yield process and post-yield stage. Prior to the upper yield point, the pre-yield stage is linear viscoelastic, and the phase almost keeps constant (shown in Fig. 6-3 and Fig. 6-5 for PP and PC respectively). During the yield process, the force decreases while the displacement increases, and the phase decreases. After the lower yield point, the post-yield stage shows a linear strain

softening, with the phase increasing. The three stages are the characteristics of Phase I, only existing in Phase I and not existing in the other phases. The following models for Phase I will be developed based on the three stages.

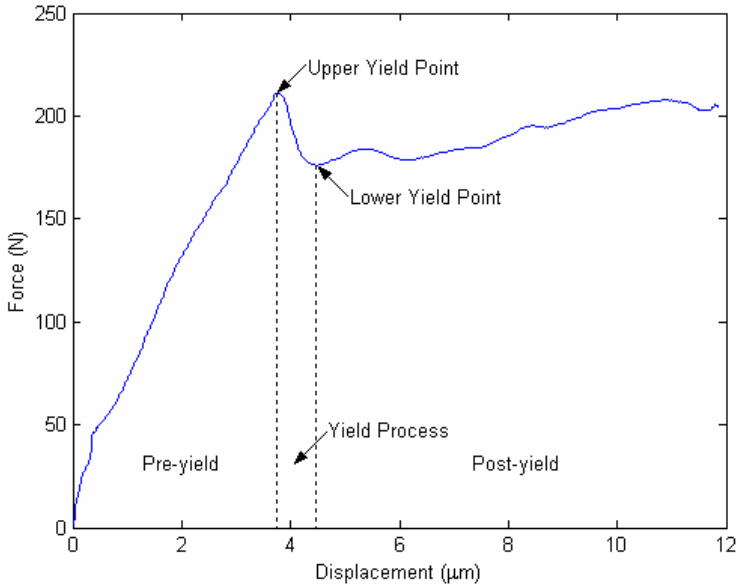

Fig. 6-2 Force vs. displacement curve for PP during Phase I

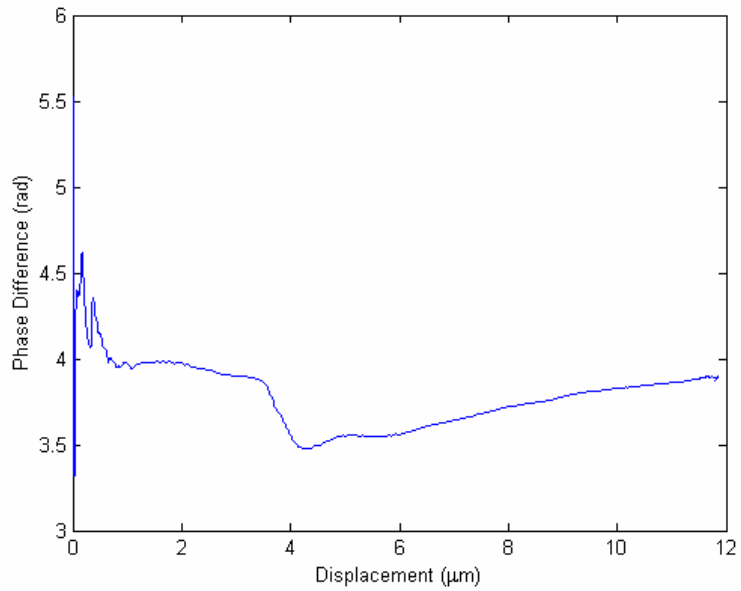

Fig. 6-3 Corresponding phase change for PP during Phase I

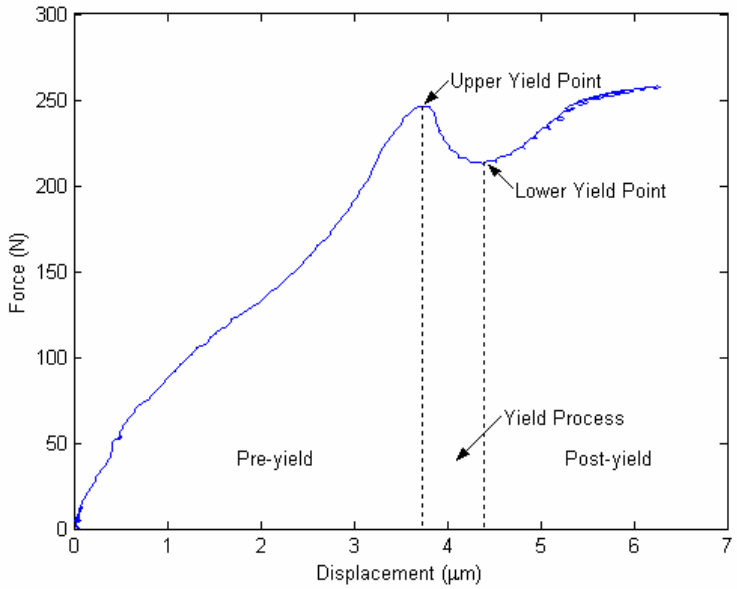

Fig. 6-4 Force vs. displacement curve for PC during Phase I

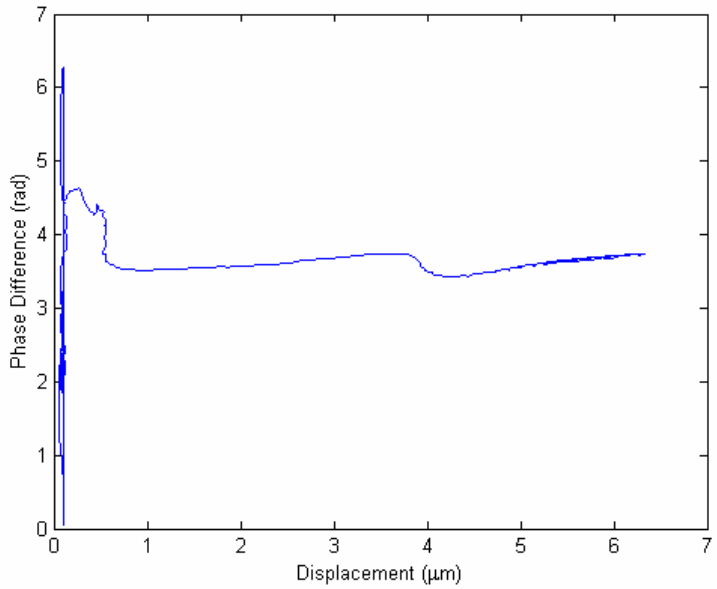

Fig. 6-5 Corresponding phase change for PC during Phase I

6.2.2 Pre-yield Mechanism

In the pre-yield stage, the linear viscoelastic behaviour can be modeled using a viscoelastic model. Normally, the viscoelasticity can be reflected by the real time force-velocity curve. Fig. 6-6 and Fig. 6-7 show the real time force-velocity curves for PP and PC respectively during the pre-yield stage. The relationships between the real time force and the real time velocity have many loops like ellipses, which become larger and larger from the center with the time. Each loop has an incline angle to the horizontal axis, and the angle becomes larger and larger with the time. Normally, if the angle is more than 45 degree, the process is more viscous than elastic [90].

Because the Maxwell model is often used to model more viscous process, the pre-yield stage can be modeled using Maxwell model, which is shown in Fig. 6-8. In this model, k_1 is the coefficient of the spring, and c_1 is the coefficient of the damper. F_1 is the applied force during the pre-yield stage, and x is the corresponding displacement.

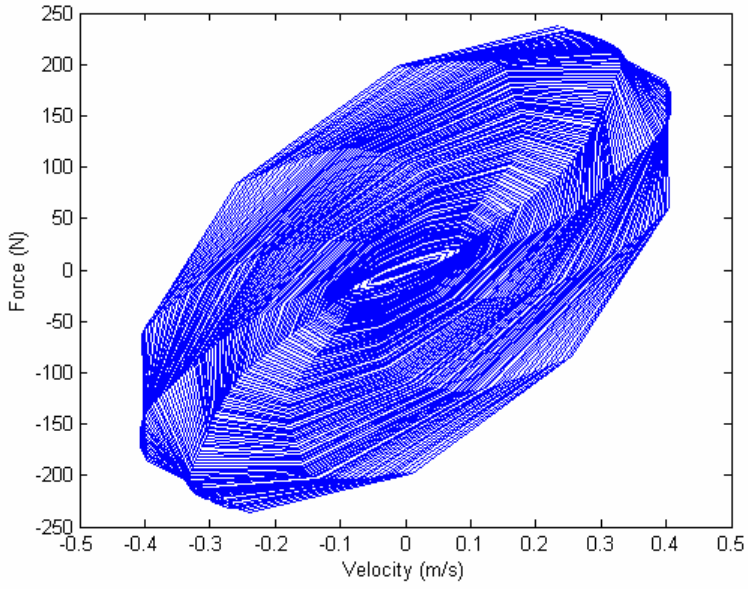

Fig. 6-6 Real time force vs. velocity curve during pre-yield stage in Phase I for PP

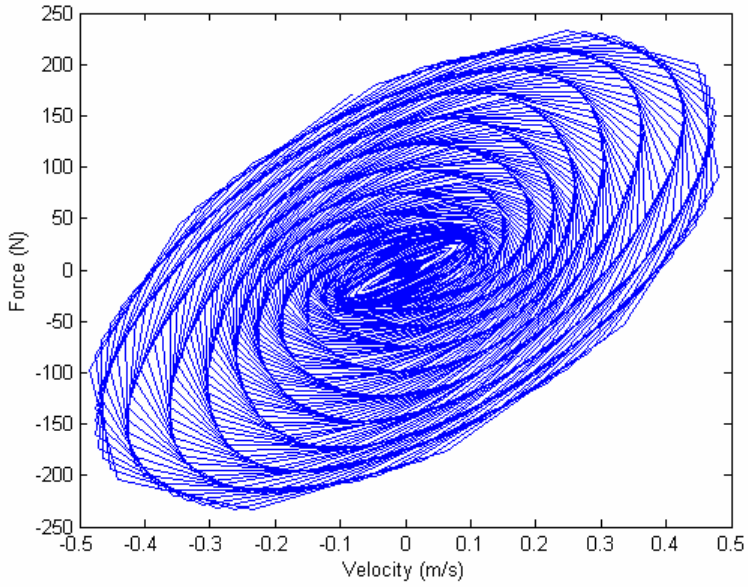

Fig. 6-7 Real time force vs. velocity curve during pre-yield stage in Phase I for PC

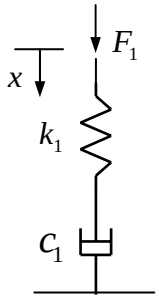

Fig. 6-8 Pre-yield mechanism

For this model, we can get the governing equation as

$$\dot{x} = \frac{\dot{F}_1}{k_1} + \frac{F_1}{c_1} \tag{6.2}$$

Because the welding system only works at one single frequency, from Eq. (4.29), there will be the following relationships:

$$\dot{x} = j\omega x \tag{6.3}$$

$$\dot{F} = j\omega F \tag{6.4}$$

Let the complex viscoelastic force be expressed as

$$F_1 = G^* x = (G' + jG'')x \tag{6.5}$$

where G^* is the complex compressive coefficients, and G', G'' are real and imaginary components respectively. Substituting Eq. (6.3) and Eq. (6.4) into Eq. (6.2) in complex variables, G', G'' can be solved as

$$G' = \frac{\omega^2 k_1 c_1^2}{k_1^2 + \omega^2 c_1^2} \tag{6.6}$$

$$G'' = \frac{\omega k_1^2 c_1}{k_1^2 + \omega^2 c_1^2} \tag{6.7}$$

From Eq. (6.6) and Eq. (6.7), we can also get the relationships as

$$k_1 = \frac{|G^*|}{\cos\theta} \tag{6.8}$$

$$c_1 = \frac{|G^*|}{\omega \sin\theta} \tag{6.9}$$

where $\theta = \tan^{-1}(G''/G') = \tan^{-1}(k_1/\omega c_1)$ is the phase difference between the force and the displacement.

6.2.3 Yield Mechanism

From the upper yield point to the lower yield point, the welding process performs in the yield stage. The drop of the force has been attributed either to adiabatic heating of the workpiece or to the geometrical change of the contact area caused by the deformation of the energy director. During the yield process, both the material viscous residence and the upper yield force contribute to the yield process, so the Bingham model is adopted, as shown in Fig. 6-9. In this model, Y_u is the upper yield force,

which depends on both the material property and the welding condition, and c_y is the viscous damping coefficient of the damper.

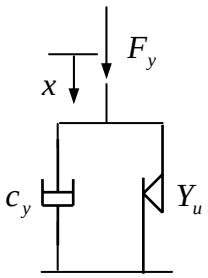

Fig. 6-9 Yield mechanism

From this model, the welding response in the yield process can be represented as the following governing equation:

$$F_y = Y_u + c_y \dot{x} sign(\dot{F}_y) \tag{6.10}$$

where, F_y is the applied force during the yield stage.

6.2.4 Post-yield Mechanism

When the welding process reaches the lower yield point, the process performs in the post-yield stage with linear strain softening. With the lower yield force, both the material viscosity and elasticity contribute to the force applied in the post-yield stage. The post-yield process can be modeled as a spring in serial with a Bingham model, which is shown in Fig. 6-10 [92]. In this model, Y_l is the lower yield force, which depends on the material property and the welding condition, k_2 is the coefficient of the spring, and c_2 is the coefficient of the damper. F_2 is the applied force in the post-yield stage.

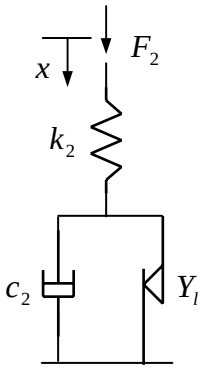

Fig. 6-10 Post-yield mechanism

The governing equation of this model can be represented as

$$\dot{x} = \frac{\dot{F}_2}{k_2} + \frac{F_2 - Y_l}{c_2} \tag{6.11}$$

6.2.5 Validation of the Viscoelastic-plastic Model

During the viscoelastic-plastic phase, the inertial force contributes to the applied force. The inertial force can be expressed as

$$F_i = m_0 \ddot{x} \tag{6.12}$$

where m_0 is a equivalent inertial mass.

Therefore, the applied force can be described by the following equation, which considers the pre-yield mechanism, the yield mechanism, the post-yield mechanism and the inertial effect.

$$F = F_1 h(Y_u - F) + F_y h(Y_u - F) h(F - Y_l) + F_2 h(F - Y_l) + F_i \tag{6.13}$$

where F_1, F_y, F_2 and F_i are defined by Eq. (6.2), Eq. (6.10), Eq. (6.11) and Eq. (6.12) respectively. $h(x)$ is a step function, which is defined by

$$h(x)=\begin{cases}1 & x\geq 0\\ 0 & x<0\end{cases} \tag{6.14}$$

The combined viscoelastic-plastic model is shown in Fig. 6-11. In this combined model, there are six parameters k_1, c_1, c_y, k_2, c_2 and m_0. Using the displacement as the input, the velocity and the acceleration are calculated with finite difference method [95]. The force can then determined using Eq. (6.13). The six parameters are estimated using the least squares method on the basis of minimizing the error between the model predicted force F_m and the experimental results of F. The error in the model is represented by the objective function J give by

$$J=\sum_{i=1}^{N}(F_i-F_{mi})^2 \tag{6.15}$$

where N is the number of the sampling data at the end of the viscoelastic-plastic phase. The results of the calculated six model parameters (SI unit) are listed in Table 6-1, which can reflect the characteristics of the welding process.

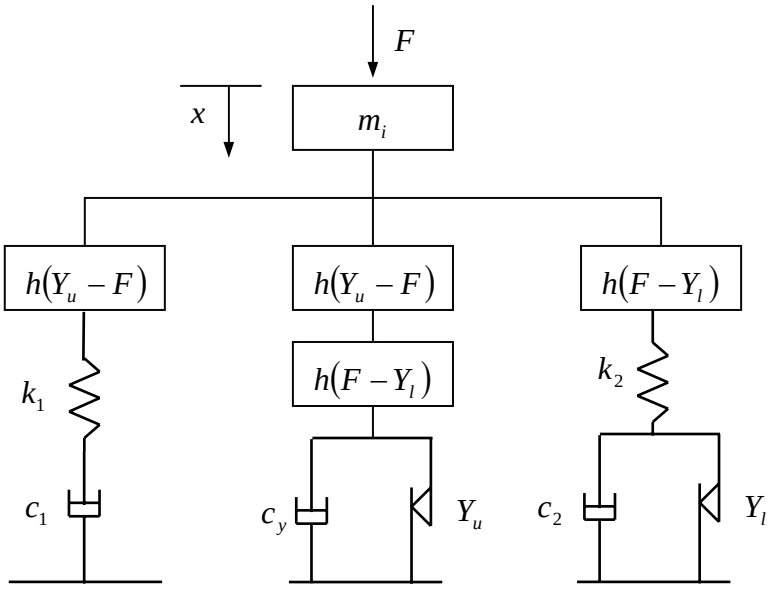

Fig. 6-11 Combined viscoelastic-plastic model

Table 6-1 Results of the calculated six model parameters

Parameters	PP	PC
k_1	75.1	66.3
c_1	6.94×10^{-4}	9.56×10^{-2}
Y_u	201	247
c_y	6.56×10^{9}	7.02×10^{9}
Y_l	166	213
k_2	4.40	27.8
c_2	1.2×10^{-3}	7.21×10^{-4}
m_0	0	0

Using the parameters estimated from the system identification process, the force vs. displacement curve is reconstructed and compared with the experimental data. Fig. 6-12 shows the reconstructed curve of the force vs. displacement curve compared with the experimental data for PP. Fig. 6-13 shows the validation of the viscoelastic-plastic model for PC. In the two figures, the solid lines are the experimental results. The dashed lines are the model results. It can be seen from the plots the combined viscoelastic-plastic model can simulate well the mechanical relationships during the viscoelastic-plastic phase.

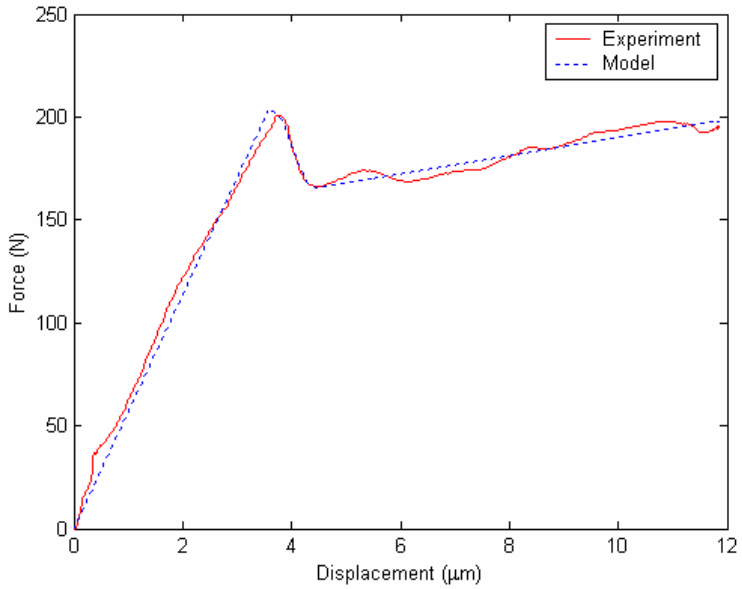

Fig. 6-12 Validation of the viscoelastic-plastic model for PP

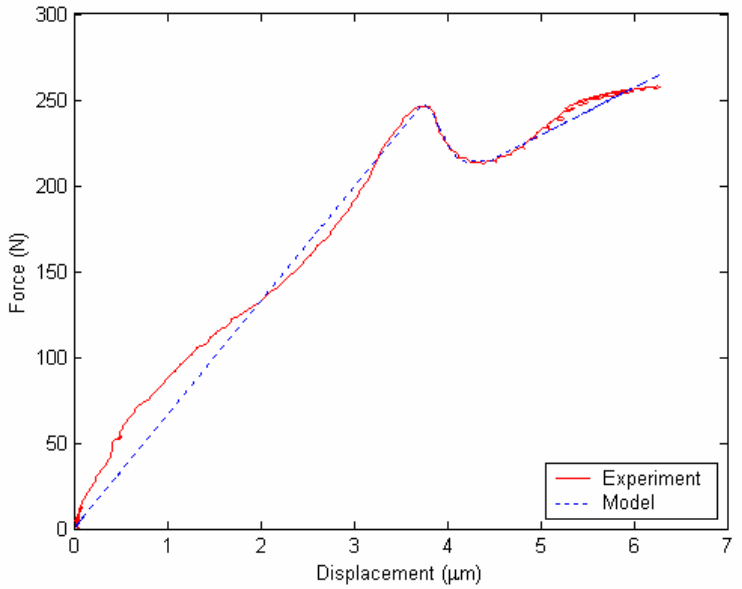

Fig. 6-13 Validation of the viscoelastic-plastic model for PC

6.3 Modeling of Phase II (Energy Director Melting Phase)

Phase II is the most complicated phase in ultrasonic welding. During the phase, the energy director begins to melt, and the contact area of the energy director increases with the melting. Therefore, the mechanical behaviours during the phase change very drastically. Fig. 6-14 and Fig. 6-15 show the force vs. displacement curves for PP and PC respectively during Phase II. As shown in the two figures, there are many loops in the force vs. displacement curves because the melting needs to consume much energy. Each loop has a yield force, and the yield force become larger and larger with the time because of the increase of the contact area. For PP, there is a melting region. For PC, there is a glass transition region. Therefore, The force vs. displacement relationship of PP is more stable than that of PC. The mechanical impedance can reflect the time-varying mechanical relationships between the force and its response for both PP and PC, which is shown in Fig. 6-16 and Fig. 6-17 for PP and PC respectively.

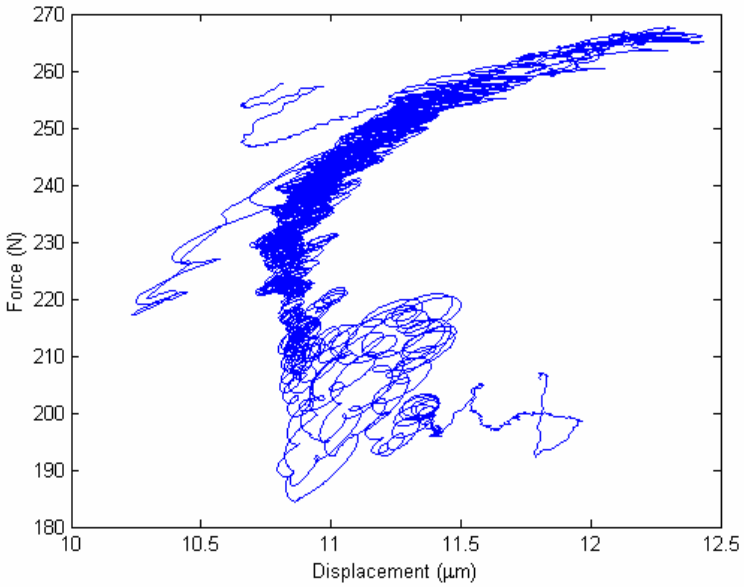

Fig. 6-14 Force vs. displacement curve for PP during Phase II

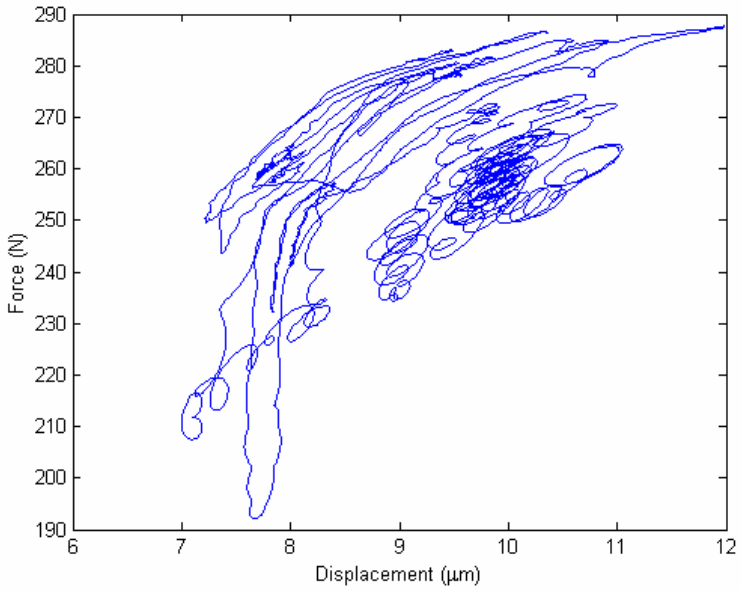

Fig. 6-15 Force vs. displacement curve for PC during Phase II

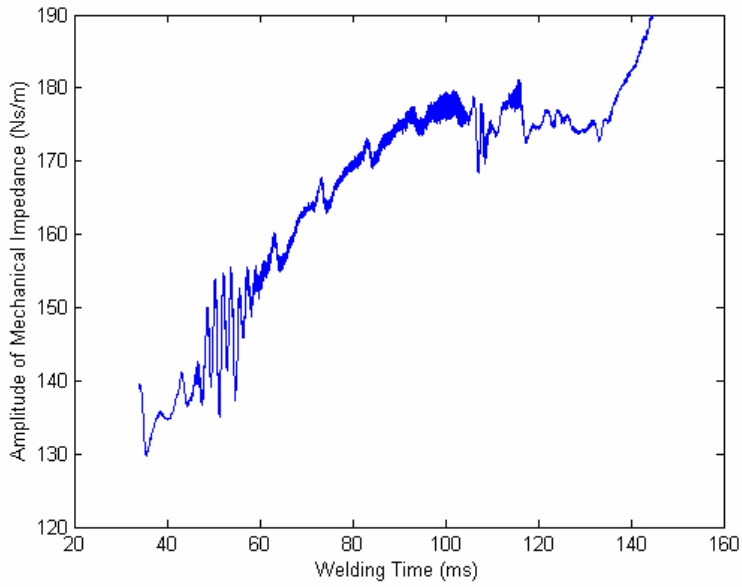

Fig. 6-16 Amplitude of the mechanical impedance for PP during Phase II

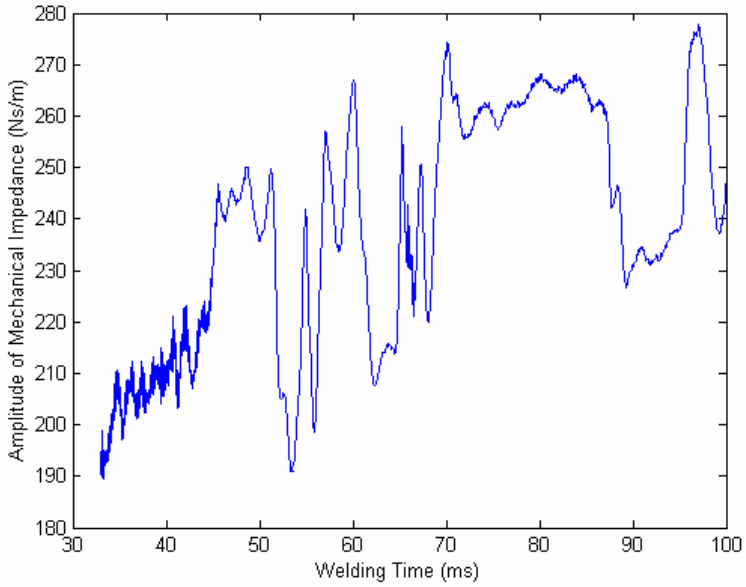

Fig. 6-17 Amplitude of the mechanical impedance for PC during Phase II

The energy director melting phase can be modeled as a time-varying spring in serial with a time-varying Bingham model, called as melting model, shown in Fig. 6-18. The governing equation of the melting model is:

$$\dot{x} = \frac{\dot{F}}{K_m(t)} + \frac{F - Y_m(t)}{C_m(t)} \tag{6.16}$$

where $K_m(t)$ is the time-varying coefficient of the spring, $C_m(t)$ is the time-varying coefficient of the damper, and $Y_m(t)$ is the time-varying yield force.

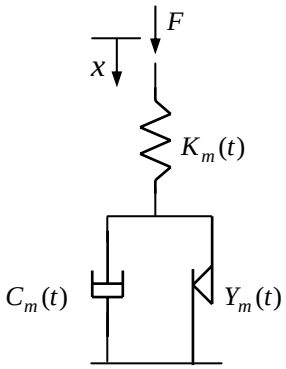

Fig. 6-18 Melting model: model of Phase II

In this model, there are three parameters $K_m(t)$, $C_m(t)$ and $Y_m(t)$. Using the displacement as the input, the velocity and the acceleration are calculated with finite difference method. The force can then determined using Eq. (6.16). The three parameters are estimated using least square method on the basis of minimizing the error between the model predicted force F_m and the experimental results of F. The error in the model is represented by the objective function J give by

$$J = \sum_{i=N+1}^{M} (F_i - F_{mi})^2 \tag{6.17}$$

where N is the number of the sampling data at the end of Phase I, and M is the number of the sampling data at the end of Phase II. Fig. 6-19, Fig. 6-20 and Fig. 6-21 show the results of the calculated three model parameters for PP material. Fig. 6-22, Fig. 6-23 and Fig. 6-24 show the results of the calculated three model parameters for PC material. The characteristics (such as viscosity, elasticity, and plasticity), and the welding conditions of the welding process can be revealed from the parameters.

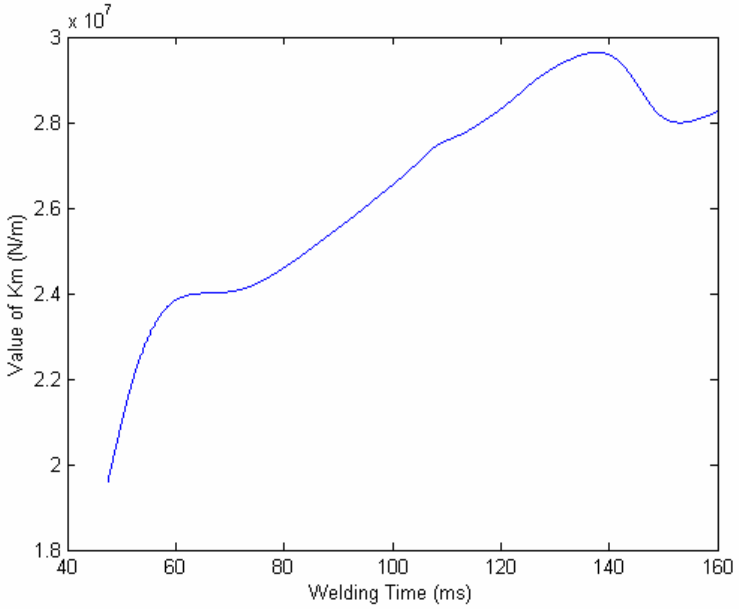

Fig. 6-19 Coefficient of the spring in the melting model for PP

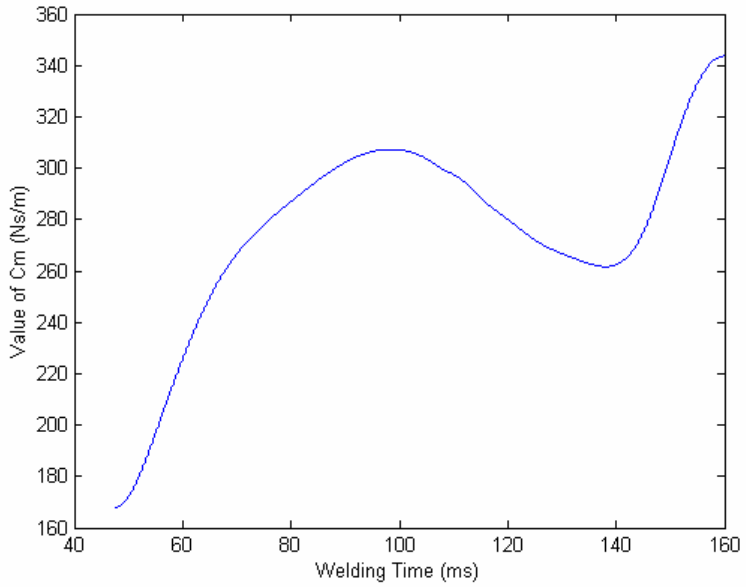

Fig. 6-20 Coefficient of the damper in the melting model for PP

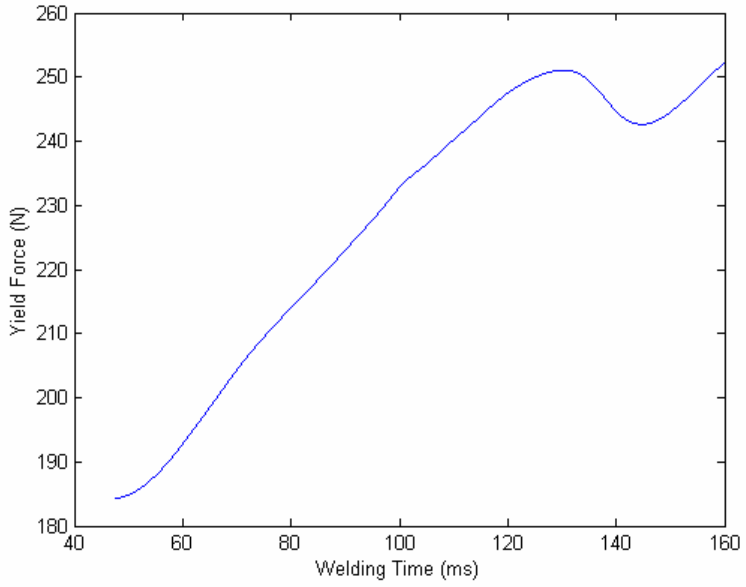

Fig. 6-21 Yield force in the melting model for PP

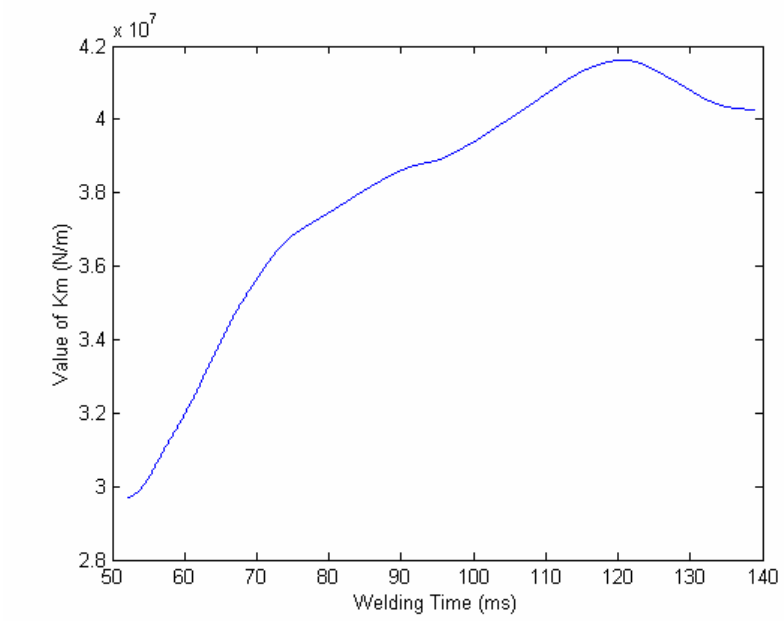

Fig. 6-22 Coefficient of the spring in the melting model for PC

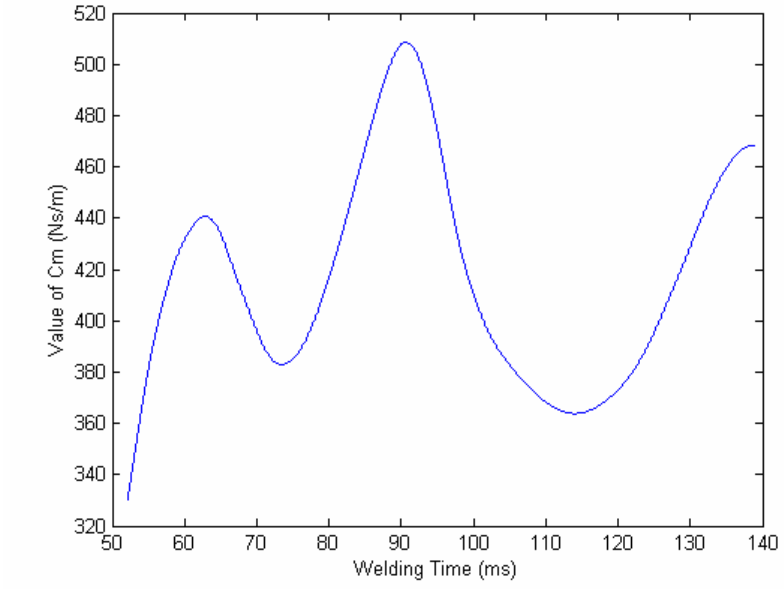

Fig. 6-23 Coefficient of the damper in the melting model for PC

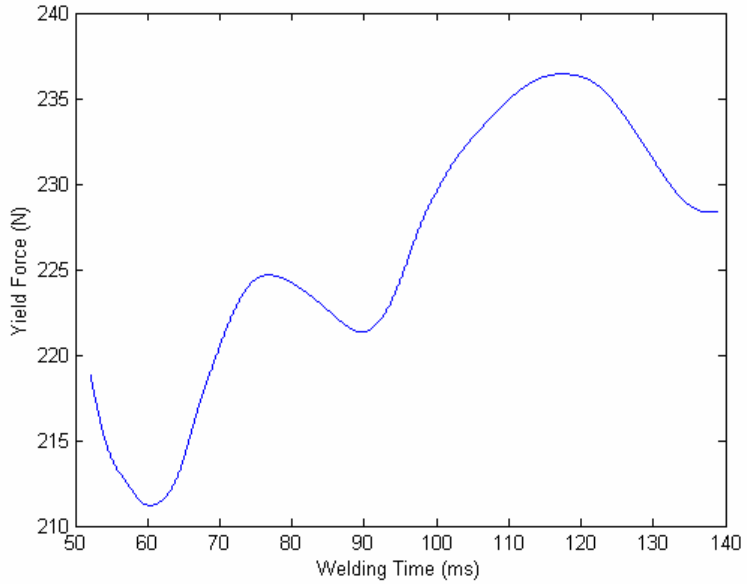

Fig. 6-24 Yield force in the melting model for PC

Using the parameters estimated from the system identification process, the mechanical impedance curves are reconstructed and compared with the experimental data. For PP, as we can see from Fig. 6-25, the reconstructed curve of the mechanical impedance using the melting model can simulate well the mechanical behaviours in Phase II.

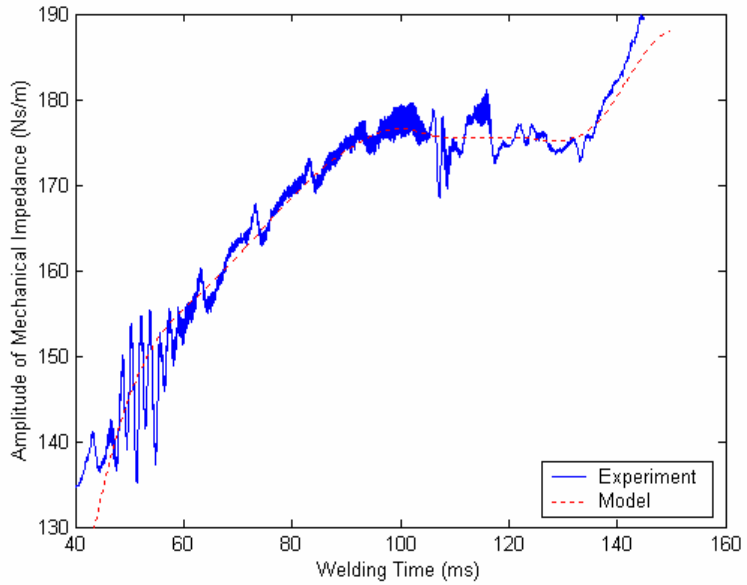

Fig. 6-25 Validation of the melting model for PP

For PC, because the amorphous material does not have orderly molecular arrangement, the melting of the energy director is not smooth. Thus the mechanical behaviours in Phase II for PC are very complex, with some big oscillations, as shown in the solid lines of Fig. 6-26. The mechanical behaviours in Phase II of the other welding processes for PC are not exactly same because of the complexity of the welding processes but similar with those in Fig. 6-26. Fig. 6-27 shows another example of the mechanical behaviours for PC in Phase II of ultrasonic welding. The mechanical behaviours in Fig. 6-27 have the similar main trend with those in Fig. 6-26, increasing with some oscillations. As we can see from the figures, the melting model can simulate the main trend of the mechanical behaviours in Phase II for PC.

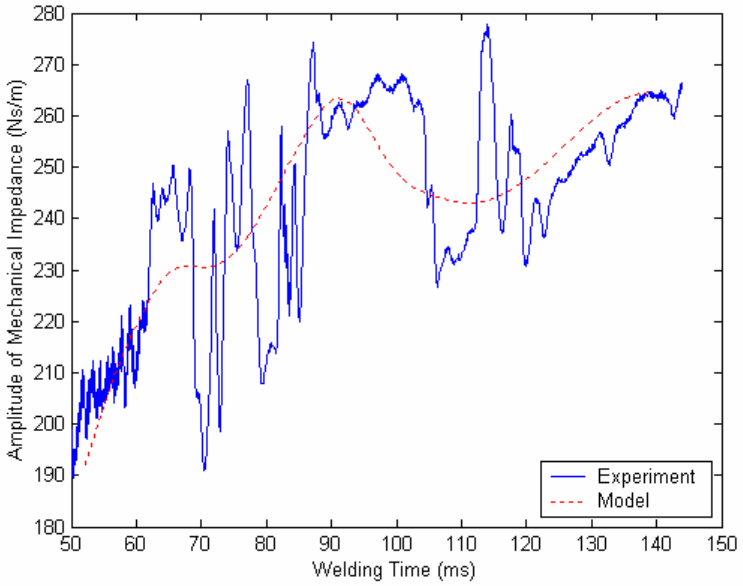

Fig. 6-26 Validation of the melting model for PC

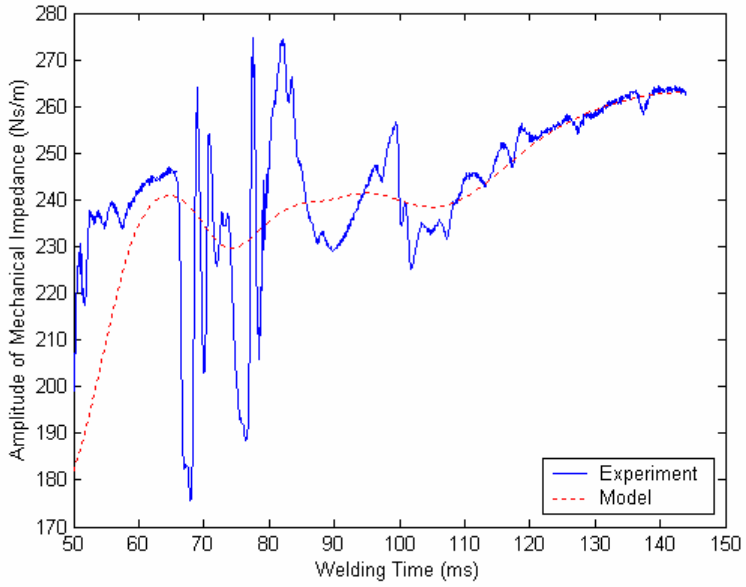

Fig. 6-27 Another example of the mechanical behaviours for PC in Phase II

6.4 Modeling of Phase III (Melting Completing Phase) and Phase IV (Upper and Lower Parts Coupling Phase)

Phase III and Phase IV include the melting of the melting layer and the coupling of the upper part and lower part. Compared with the melting of the energy director, the melting condition during Phase III remains constant for a certain period of time. After that, a constant liquid layer thickness forms in weld, and the upper part and lower part are coupled together via intermolecular diffusion and entanglement of the polymer chains. Because the contact area does not change much during the two phases, the mechanical behaviours are similar, so they can be modeled together.

Fig. 5-11 and Fig. 5-12 show the force vs. displacement curves for PP and PC respectively during Phase III and Phase IV. Fig. 6-28 and Fig. 6-29 show the amplitude of the mechanical impedance for PP and PC respectively. During the two

phases, the mechanical impedance can reflect the time-varying mechanical relationships between the force and its response.

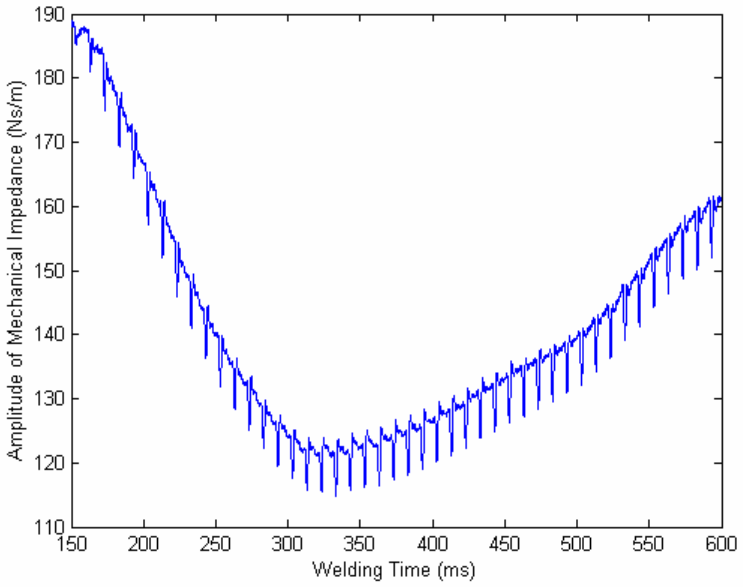

Fig. 6-28 Mechanical impedance for PP during Phase III and Phase IV

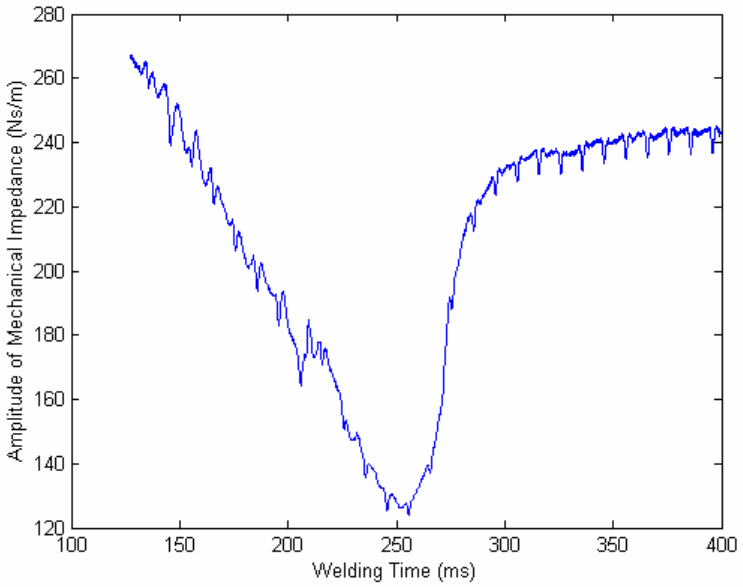

Fig. 6-29 Mechanical impedance for PC during Phase III and Phase IV

Because the real time force-velocity curves are very viscous, which is determined by the liquid joint interface, the two phases can be modeled as a time-varying Maxwell model, called as coupling model, shown in Fig. 6-30. The governing equation of the coupling model is represented as:

$$\dot{x} = \frac{\dot{F}}{K_c(t)} + \frac{F}{C_c(t)} \tag{6.18}$$

where, $K_c(t)$ is the time-varying coefficient of the spring, and $C_c(t)$ is the time-varying coefficient of the damper.

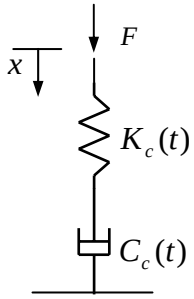

Fig. 6-30 Coupling model: model of Phase III and Phase IV

In this model, there are two parameters $K_c(t)$ and $C_c(t)$. Using the displacement as the input, the velocity and the acceleration are calculated with finite difference method. The force can then determined using Eq. (6.18). The two parameters are estimated using least square method on the basis of minimizing the error between the model predicted force F_m and the experimental results of F. The error in the model is represented by the objective function J give by

$$J = \sum_{i=M+1}^{K} (F_i - F_{mi})^2 \tag{6.19}$$

where M is the number of the sampling data at the end of Phase II, and K is the number of the sampling data at the end of Phase IV. Fig. 6-31 and Fig. 6-32 show the

results of the calculated two model parameters for PP material, and Fig. 6-33 and Fig. 6-34 show the results of the calculated two model parameters for PC material. The characteristics (such as viscoelasticity and liquid property) and the welding conditions of the welding process can be revealed from the parameters.

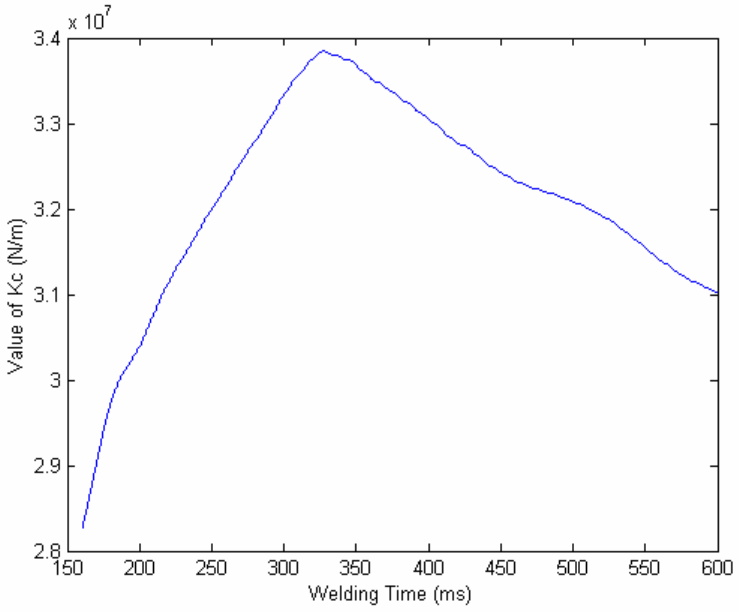

Fig. 6-31 Coefficient of the spring in the coupling model for PP

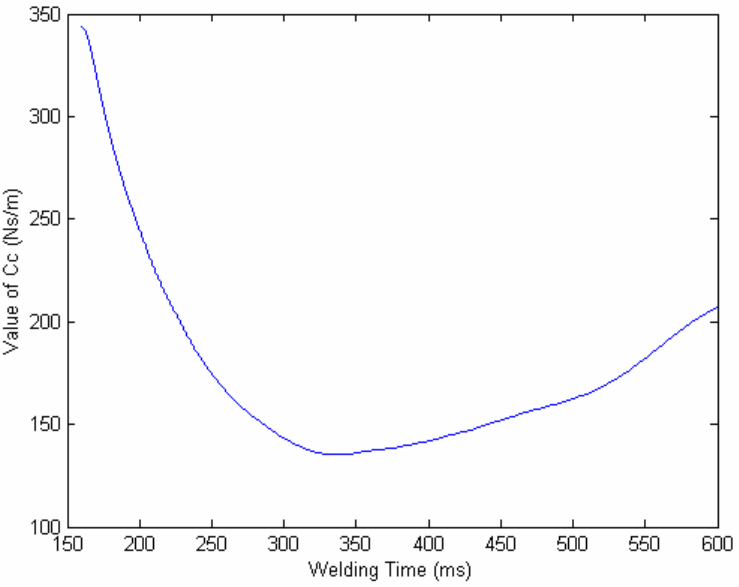

Fig. 6-32 Coefficient of the damper in the coupling model for PP

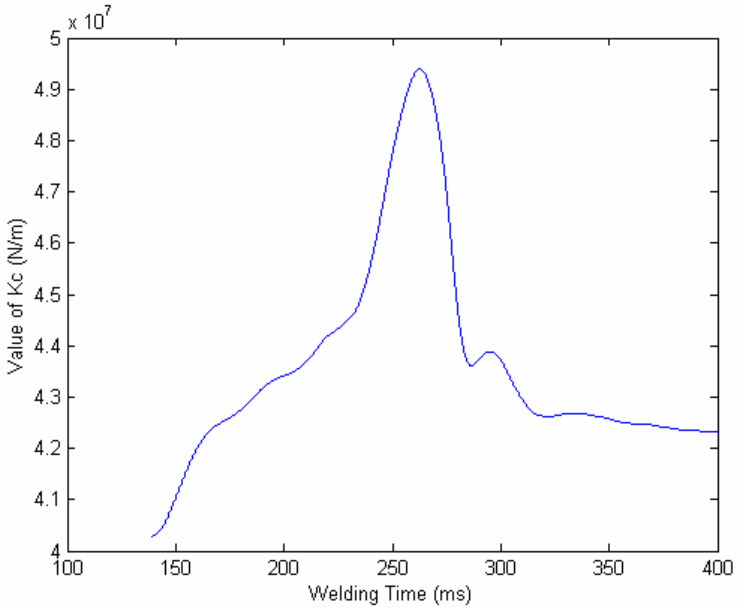

Fig. 6-33 Coefficient of the spring in the coupling model for PC

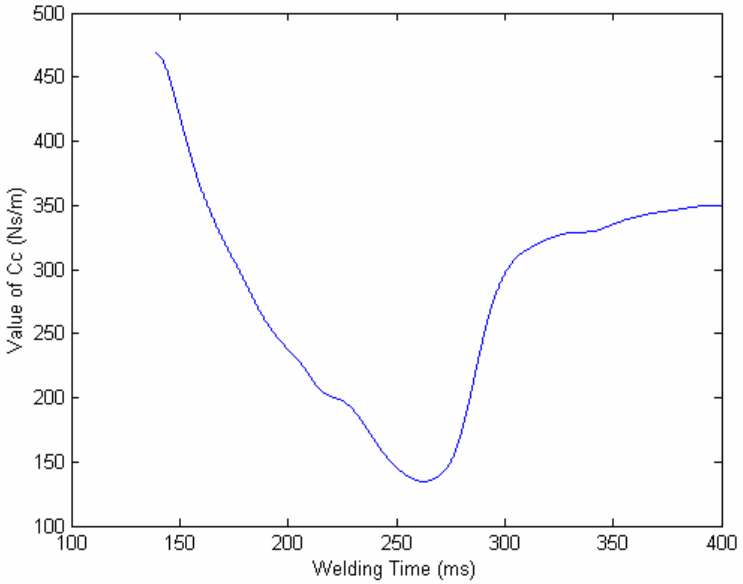

Fig. 6-34 Coefficient of the damper in the coupling model for PC

Using the parameters estimated from the system identification process, the mechanical impedance curves are reconstructed and compared with the experimental data. Fig. 6-

35 and Fig. 6-36 show the reconstructed curves of the mechanical impedance compared with the experimental data for PP and PC respectively. It can be seen from the plots the coupling model can simulate well the mechanical relationships during Phase III and Phase IV.

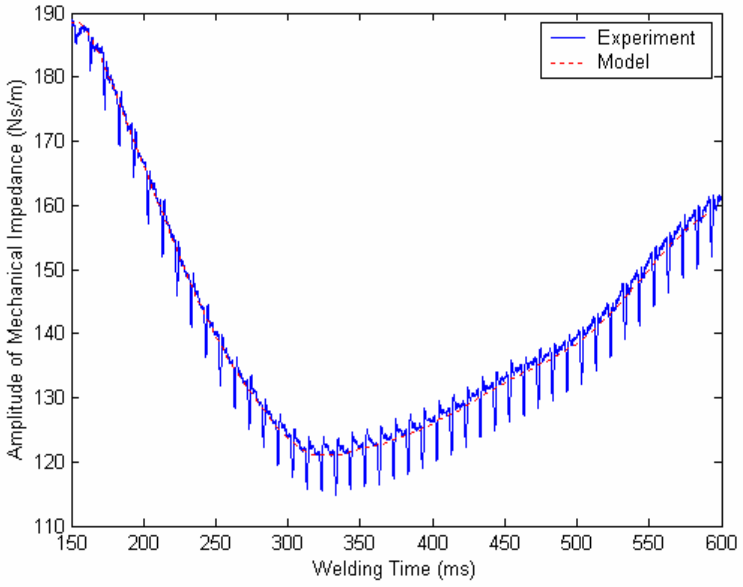

Fig. 6-35 Validation of the coupling model for PP

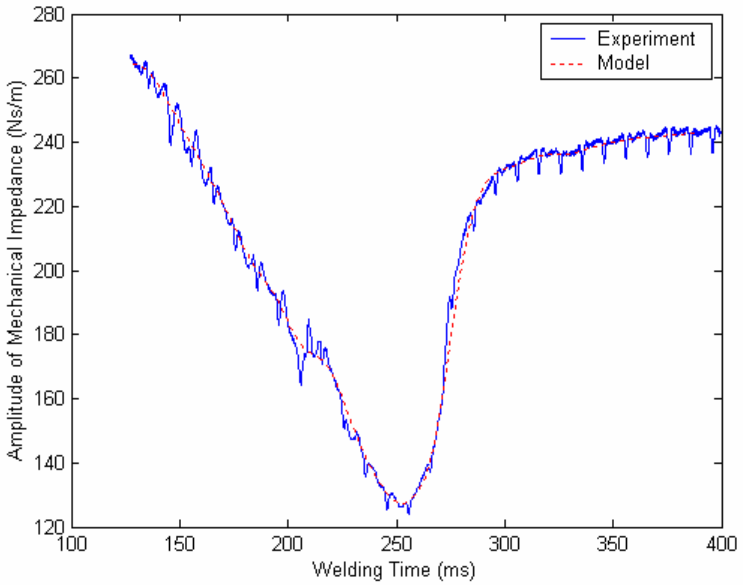

Fig. 6-36 Validation of the coupling model for PC

Chapter 7

Conclusions and Recommendations

In this thesis, measurement of the mechanical forces and motions at the joint interface is reported first. Then, based on the measured mechanical variables, the thermo-mechanical interaction, the welding process and the transitions of the mechanical behaviours of thermoplastics during ultrasonic welding of thermoplastics are investigated. In this chapter, the main conclusions are first summarized, and then future research directions are outlined.

7.1 Conclusions

To measure the mechanical forces and motions at the joint interface, the actuating mechanism of an ultrasonic welding machine is modeled as a transduction matrix using simultaneous sensing and actuating. The transduction matrix relates the mechanical force and velocity with the input electrical voltage and current to the actuator. For a given ultrasonic welding machine, the transduction matrix is an intrinsic property, which does not change with the input and output variables, and the determinant of the transduction matrix is equal to one. By using experimental methods, the transduction matrix was calculated using the least squares method after digital filtering and the Hilbert transform. Based on the validation of the transduction matrix

of the actuating mechanism, the force and velocity at the joint interface can be easily detected by measuring the input voltage and current of the actuating mechanism. The mechanical impedance can also be deduced from the electrical impedance.

In order to investigate the thermal-mechanical interaction in ultrasonic welding of thermoplastics, the equation governing the thermo-mechanical behaviour during ultrasonic welding was derived. In the equations, the applied mechanical force can be detected from the input voltage and current, and the dynamic compliance of thermoplastics at the working frequency is measured from the mechanical impedance using a new proposed method. The finite element method was then employed to solve the governing equation with appropriate boundary and initial conditions. The experimental results match the numerical results well, which validate the developed model. The model can be used to obtain the time varying temperature distributions in welding samples during ultrasonic welding, so the model provides an effective way for detailed understanding of the dynamic thermal behaviours.

The mechanism in ultrasonic welding of thermoplastics was investigated by using the detected mechanical variables at the joint interface. The study using the mechanical impedances and the force vs. displacement curves show that ultrasonic welding can be divided into four distinct phases: viscoelastic-plastic phase, energy director melting phase, melting completing phase, and upper and lower parts coupling phase. Comparing with other variables, the mechanical impedance is the most characteristic variable of ultrasonic welding. The effects of amplitude and pressure on the mechanical impedance show that the mechanical impedance can also reflect the machine settings.

Based on the main characteristics of thermoplastics during ultrasonic welding, the viscoelastic-plastic model, the melting model and the coupling model are proposed to model the mechanical behaviours of thermoplastics for each phase of ultrasonic welding. The validations of the three models show that they are effective to model the mechanical behaviours. The parameters of the models can further reveal the detailed characteristics of ultrasonic welding.

7.2 Recommendations

The mechanical impedance at the joint interface is the most characteristic variable of the welding process, which reflects the weld quality of ultrasonic welding. The proposed four phases of ultrasonic welding are the important indicators of the welding process. With the proper trend of the mechanical impedance, such as the increase in Phase II, the decrease in Phase III and the final increase in Phase IV, the welding process can produce a good weld. Otherwise, a bad weld will be formed. For a better weld quality, the welding process must have the optimal four phases and cannot have the over-welding phase. Thus the mechanical impedance can be used to monitor the welding condition and control the weld quality of ultrasonic welding. By using the mechanical impedance, the process parameters in ultrasonic welding can be optimized for a better performance of the mechanical impedance to produce a better weld. In addition, the lower mechanical impedance causes the more power transition during the welding process. When designing the horn or the workpiece for ultrasonic welding, we can optimize the horn or the workpiece for the lower mechanical impedance.

The electrical impedance is one characteristic variable of ultrasonic welding. For a given ultrasonic welding machine, the electrical impedance has the fixed relationship with the mechanical impedance, and they both can determine the welding condition and the weld quality. Because the mechanical impedance is difficult to be controlled directly, the electrical impedance can be used a control variable to better optimize the welding process for obtaining improved weld strength.

Since the mechanical impedance is the most characteristic variable of ultrasonic welding, it can be used for designing ultrasonic welding machine. Impedance is an important variable for power transmission, and the mechanical impedance changes with the welding time. The actuating mechanism of ultrasonic welding machine should be designed for maximizing the power transmission for the whole welding process through optimizing the output impedance of the actuating mechanism.

References

[1] Janet Devine, Ultrasonic Plastics Welding Basics, *Welding Journal*, Volume 80, January 2001, p 29-33.

[2] Plastics Design Library, Handbook of Plastics Joining, The Library, Norwich, New York, 1999, p 37-66.

[3] American Welding Society, Welding Handbook, Eighth Edition, 1991.

[4] Branson Ultrasonics Corporation, 900AES/AOS Series Advanced 20 kHz Power Supplies, Instruction Manuals, 1998.

[5] Branson Ultrasonics Corporation, 900AES/AOS Series Actuators Instruction Manuals, 1993.

[6] Branson Ultrasonics Corporation, Boosters, Technical Information, PW-2, 2000.

[7] Branson Ultrasonics Corporation, Ultrasonic Plastics Assembly, 2000.

[8] Branson Ultrasonics Corporation, Characteristics and Compatibility of Thermoplastics for Ultrasonic Assembly, Technical Information, PW-1, 2000.

[9] American National Standards Institute, Specification for Standardized Ultrasonic Welding Test Specimen for Thermoplastics, American Welding Society, 1999.

[10] G. Menges and H. Potente, Study on the Weldability of Thermoplastic Materials by Ultrasound, *Welding in the World*, Vol.9, No.1/2, 1971, p 46-59.

[11] C. J. Aliosio, D.G. Wahl and E. E. Whetsel, A Simplified Thermoviscoelastic

Analysis of Ultrasonic Bonding, *SPE Technical Papers*, Brookfield, CT, 1972.

[12] E. Mori, S. Kaneko, M. Gakumazawa and Y. Okawa, Ultrasonic Welding of Plastics, Conference Proceedings, *Ultrasonics International*, London, UK, 1973, p 16-19.

[13] Ng Wing-Chak, Study of Vibration and Viscoelastic Heating of Thermoplastic Parts Subjected to Ultrasonic Excitation, Ph. D Thesis, Ohio State University, UMI, 1996.

[14] M. N. Tolunay, P. R. Dawson and K. K. Wang, Heating and Bonding Mechanisms in Ultrasonic Welding of Thermoplastics, *Polymer Engineering and Science*, Vol. 23, No. 13, 1983, p 726-733.

[15] N. Tateishi, T. H. North and R. T. Woodhams, Ultrasonic Welding Using Tie-Layer Materials. Part I: Analysis of Process Operation, *Polymer Engineering and Science,* Vol. 32, No. 9, 1992, p 600-611.

[16] G. Ramarathnam, T. H. North, and R. T. Woodhams, Ultrasonic Welding Using Tie-Layer Materials. Part II: Factors Affecting the Lap-Shear Strength of Ultrasonic Welds, *Polymer Engineering and Science,* Vol. 32, No.9, Mid-May 1992, p 612-619.

[17] Avraham Benatar, Ultrasonic Welding of Advanced Thermoplastic Composites, Ph. D Thesis, Massachusetts Institute of Technology, UMI, 1987.

[18] Avraham Benatar and Timothy G. Gutowski, Ultrasonic Welding of Peek Graphite APC-2 Composites, *Polymer Engineering and Science*, Vol. 29, No. 23, Mid-December 1989, p 1705-1721.

[19] Avraham Benatar, Raman V. Eswaran, and Satinder K. Nayar, Ultrasonic Welding of Thermoplastics in the Near-field, *Polymer Engineering and Science*, Vol. 29, No. 23, Mid-December 1989, p 1689-1698.

[20] Avraham Benatar and Zhang Cheng, Ultrasonic Welding of Thermoplastics in the Far-field, *Polymer Engineering and Science,* Vol. 29, No. 23, Mid-December 1989, p 1699-1704.

[21] W. Land, and Leverkusen, Investigations into the Process of Ultrasonic Welding, *Kunststoffe*, Vol. 68, No.4, 1978, p 233-237.

[22] C. J. Nonhof and G. A. Luiten, Estimates for Processing Conditions During the Ultrasonic Welding of Thermoplastics, *Polymer Engineering and Science,* Vol.36, No.9, Mid-May 1996, p 1177-1183.

[23] H. Van Wijk, G. A. Luiten, P. G. Van Engen and C. J. Nonhof, Process Optimization of Ultrasonic Welding, *Polymer Engineering and Science*, Vol. 36, No.9, Mid-May 1996, p 1165-1176.

[24] C. N. Netze, Ultraschallschweissen von hochtemperaturbestandigen, unverstarkten, kurzglasfaser- und end-losfaserverstarkten Thermoplasten, ABK Band 13, Verlag der Augustinus Buchhandlung, Aachen, Germany, 1993.

[25] W. Michaeli and W. Korte, Quality Assurance in Ultrasonic Welding Using Statistical Process Models – Predication of Weld Strength, *Annual Technical Conference – ANTEC, Conference Proceedings,* Society of Plastics Engineers, Brookfield, CT, USA, 1995, p 1290-1295.

[26] Shih-Jung Liu, Yew-Khoy Chuah, Bo-Chien Chang, Liang-Han Chien, and Gwomei Wu, Development of Weldability Diagrams for Ultrasonic Welding of Thermoplastics in Far Field, Plastics, *Rubber and Composites Processing and Applications*, Vol. 27, No. 6, 1998, p 279-286.

[27] Yew-Khoy Chuah, Liang-Han Chien, B. C. Chang, and Shih-Jung Liu, Effects of the Shape of the Energy Director on Far-Field Ultrasonic Welding of Thermoplastics, *Polymer Engineering and Science,* Vol.40, No.1, January 2000, p 157-167.

[28] Weihua Shi and Trevor Little, Mechanisms of Ultrasonic Joining of Textile Materials, *International Journal of Clothing Science and Technology*, Vol. 12, No.5, 2000, p 331-350.

[29] He Fugui, Modeling and Process Control of Ultrasonic Welding of Plastics, Ph. D Thesis, Ohio State University, UMI, 1992.

[30] Fu Si and Masao IDE, Measurement on Specimen Acoustic Impedance in Ultrasonic Plastics Welding, *Japanese Journal of Applied Physics*, Vol. 35, Part 1, No. 5B, 1995, p 2740-2744.

[31] Luan Jingen, Modeling and Monitoring of Ultrasonic Welding of Thermoplastics, Ph. D Thesis, Nanyang Technological University, 2002.

[32] J. L. Doyle, Heating of Rectangular Energy Directors during Ultrasonic welding, SB Thesis, Dept. of Mechanical Engineering, Massachusetts Institute of Technology, Cambridge, MA, 1996.

[33] H. Potente, "Untersuchung Der Schweissbarkeit Thermoplasticher Kuntstoffe Mit Ultraschall", Dissertation, RWTH, Aachen, Germany, 1971.

[34] N. E. Barbari and G. Menges, "SPE ANTEC Tech. Papers", 33, 1021, 1987.

[35] Yi Xie & Shih-Fu Ling, Study on Turning Mechanical Impedance of Inertial Actuator with Passive Shunt Circuits, *Asia-Pacific Vibration Conference'99*, Singapore, 1999, p 129-133.

[36] Dong Zhang & Shih-Fu Ling, Monitoring Wire Bonding via Time-frequency Analysis of Horn Vibration, *1st International Workshop on Electronics Materials and Packaging (EMAP '99)*, Singapore, September 1999, p 216-220.

[37] Shih-Fu Ling & Wan Lixue, Monitoring and Diagnosing a Spot Welding Process via Electrical Input Impedance, *SEM IX International Congress*, Orlando,

Florida, June 2000.

[38] Ling Shih-Fu & Xie Yi, Mechanical Impedance Detection Utilizing Sensing Capability of Piezo-ceramic Inertial Actuators, *Proceedings of the International Modal Analysis Conference – IMAX-XVII*, San Antonio, Texas, USA, 2000, p 1901-1905.

[39] Ling Shih-Fu & Yongjie Tang, A New Modal Testing Technique for Miniature Structures, *Proceedings of the International Modal Analysis Conference – IMAC-XIX*, Kissimmee, USA, 2001, p 1478-1482.

[40] Yi Xie & Shih-Fu Ling, Material Characterization by Depth Sensing Impedance Measurement, *Proceedings of 2001 SEM Annual Conference*, Portland, Oregon, USA, June 2001, p 215-218.

[41] S. F. Ling & Y. Xie, Modeling and Identification of a Piezoceramic Sensor Cum Actuator, *Proceedings of 2001 SEM Annual Conference*, Portland, Oregon, USA, June 2001, p 145-148.

[42] Ling Shih-Fu & Xie Yi, Monitoring Structural Integrity Using a Piezoceramic Inertial Actuator cum Sensor, *Journal of Sound and Vibration*, volume 247, 2001, p 731-737.

[43] Ling Shih-Fu & Xie Yi, Detecting Mechanical Impedance of structures Using the Sensing Capability of a Piezoceramic Inertial Actuator, *Sensors and Actuators A*, Volume 93, 2001, p 243-249.

[44] Zhang Dong, Study of Mechanism of Ultrasonic Wire Bonding Process, Ph.D Thesis, Nanyang Technological University, Singapore, 2002.

[45] Fu L. Y., Ling S. -F. and Liang F. G., Application of Wavelet and Hilbert Transform in Sensing cum Actuating Technology, *ICITA 2002*, Australia, 2002, p 369-371.

[46] Ling Shih-Fu & Lu Bei, Modeling of a PZT-driven Cantilever Actuator, *Proceedings of SPIE – The International Society for Optical Engineering*, Vol. 4753, 2002, p 724-730.

[47] Yin Yanling, A Novel Method for Testing Mechanical Properties of Viscoelastic Materials, First Year Report in fulfillment for the requirement of Ph.D., Nanyang Technological University, Singapore, 2002.

[48] Wang Deyang, Sensing Capability of an Actuating Cantilever, First Year Report in fulfillment for the requirement of Ph.D., Nanyang Technological University, Singapore, 2003.

[49] Hou Xianyan, & Ling Shih-Fu, A Sensing cum Actuating Transducer for Detecting Rotational Mechanical Impedance of Structures, *First International Conference on Structural Health Monitoring and Intelligent Infrastructure*, Tokyo, Japan, Nov 2003, p 893-897.

[50] Yanling Yin, Shih-Fu Ling and Yong Liu, A Dynamic Indentation Method for Characterizing Soft Incompressible Viscoelastic Materials, *Materials Science and Engineering A*, Vol. 379, 2004, p 334-340.

[51] Ilene J. Busch-Vishniac, Electromechanical Sensors and Actuators, Springer-Verlag, New York, 1999.

[52] John P. Bentley, Principles of Measurement Systems, 3rd Edition, Longman, 1995.

[53] Stefan Niewiadomshi, Filter Handbook: A practical design guide, Heinemann Newnes, Oxford, 1989.

[54] H. Baher, Analog & Digital Signal Processing, John Wiley & Sons, New York, 1990.

[55] Ashok Ambardar, Analog and Digital Signal Processing, 2nd edition, Brooks/Cole, 1999.

[56] Alan V. Oppenheim & Ronald W. Schafer, Discrete-Time Signal Processing, Prentice-Hall, 1989.

[57] Stefan L. Hahn, Hilbert Transforms in Signal Processing, Artech House, 1996.

[58] Julius S. Bendat and Allan G. Piersol, Random Data: Analysis and Measurement Procedures, Wiley-Interscience, Third Edition, 2001.

[59] Michael McBrearty, Lee H. Kim and Nihat M. Bilgutay, Analysis of Impedance Loading in Ultrasonic Transducer Systems, *IEEE Ultrasonics Symposium*, 1998, p 497-502.

[60] IEEE Standard 177, Standard Definitions and Methods of Measurement for Piezoelectric Vibrators, 1996.

[61] Gordon S. Kino, Acoustic Waves: Devices, Imaging, and Analog Signal Processing, Prentice-Hall, 1987.

[62] Morten Willatzen, Ultrasound Transducer Modeling – General Theory and Applications to Ultrasound Reciprocal Systems, *IEEE Transactions on Ultrasonics, Ferroelectrics, and Frequency Control*, Vol. 48, No. 1, 2001, p 100-112.

[63] Glenn Whitworth, Discussion of One-D Piezoelectric Transducer Models with Loss, *IEEE Transactions on Ultrasonics, Ferroelectrics, and Frequency Control*, Vol. 48, No. 3, 2001, p 844-846.

[64] J. H. Hu, G. R. Li, H. L. Chan and C. L. Choy, An Improved Method for Analyzing the Performance of Multilayer Piezoelectric Transformers, IEEE Ultrasonics Symposium, 1999, p 943-946.

[65] Lorenzo Parrini, Design of Advanced Ultrasonic Transducers for Welding Devices, *IEEE Transactions on Ultrasonics, Ferroelectrics, and Frequency Control*, Vol. 48, No. 6, 2001, p 1632-1639.

[66] J. A. Oliver, R. Prieto, M. Sanz, J. A. Cobos and J. Uceda, 1D Modeling of Multi-layer Piezoelectric Transformers, IEEE, 2001, p 2097-2102.

[67] Raymond A. Decarlo and Pen-Min Lin, Linear Circuit Analysis: Time domain, Phasor, and Laplace Transform Approaches, Prentice Hall, 1995.

[68] A. A. Shabana, Theory of Vibration, Volume 1: An Introduction, Springer-Verlag, 1991.

[69] John D. Ferry, Viscoelastic Properties of Polymers, Wiley, New York, 1980.

[70] T. Hatakeyama and F. X. Quinn, Thermal Analysis: Fundamentals and Applications to Polymer Science, John Wiley & Sons, 1994.

[71] Kurt C. Rolle, Introduction to Thermodynamics, C.E. Merrill Pub. Co., Columbus, Ohio, 1980.

[72] Frank P. Incropera & David P. Dewitt, Fundamentals of Heat and Mass Transfer, Third Edition, John Wiley & Sons, New York, 1990.

[73] Robert J. Young, Introduction to Polymers, Second Edition, Chapman and Hall, 1991.

[74] Paul C. Painter and Michael M. Coleman, Fundamentals of Polymer Science: An Introductory Text, Technomic Pub. Co., Lancaster, PA, 1997.

[75] Niels Saabye Ottosen & Hans Petersson, Introduction to the Finite Element Method, Prentice Hall, 1992.

[76] Kenneth H. Huebner, Earl A. Thornton and Ted G. Byrom, The Finite Element Method for Engineers, Third Edition, John Wiley & Sons, 1995.

[77] Singiresu S. Rao, Mechanical Vibrations, Third Edition, Addison-Wesley Publishing Company, 1995.

[78] ASTM Committee E-20 on Temperature Measurement and Subcommittee E20.04 on Thermocouples, Manual on the Use of Thermocouples in Temperature Measurement, American Society for Testing and Materials, 1981.

[79] Richard S. Figliola and Donald E. Beasley, Theory and Design for Mechanical Measurements, Second Edition, John Wiley and Sons, 1995.

[80] Peter Kohnke, ANSYS: Theory Reference Release 5.6, ANSYS Inc., Canonsburg, PA, 1999.

[81] ANSYS, Inc, ANSYS Basic Analysis Procedures Guide: ANSYS Release 5.7, ANSYS Inc., Canonsburg, PA, 2000.

[82] ANSYS, Inc, ANSYS Elements Reference: ANSYS Release 5.7, ANSYS Inc., Canonsburg, PA, 2000.

[83] ANSYS, Inc, ANSYS Modeling and Meshing Guide: ANSYS Release 5.7, ANSYS Inc., Canonsburg, PA, 2000.

[84] ANSYS, Inc, ANSYS Thermal Analysis Guide: ANSYS Release 5.7, ANSYS Inc., Canonsburg, PA, 2000.

[85] Shi Aiguo, Effect of Ultrasonic Welding Variables on Weld Strength of Thermoplastics, Master Thesis, University of Massachusetts Lowell, UMI, 1995.

[86] Wendy Ang, Studies on Monitoring and Diagnosing Ultrasonic Welding of Plastics, Final Year Project Report, Nanyang Technological University, 2001.

[87] Malcolm P. Stevens, Polymer Chemistry (An Introduction), Third Edition, Oxford University Press, 1999.

[88] Z. H. Stachurski, Engineering Science of Polymeric Materials, Polymer Division of Royal Chemical Institute, 1987.

[89] John J. Aklonis and William J. MacKnight, Introduction to Polymer Viscoelasticity, Wiley, New York, 1983.

[90] Yang Tingqing, Theory of Viscoelasticity, Huazhong University of Science and China Press, 1988.

[91] Jacek J. Skrzypek and Richard B. Hetnarski., Plasticity and Creep: Theory, Examples, and Problems, CRC Press, Begell House, Boca Raton, Fla., 1993.

[92] Takashi Ariyama, Viscoelastic-plastic Deformation Behavior of Polypropylene After Cyclic Preloadings, *Polymer Engineering and Science*, Vol. 34, No. 17, Mid-September 1994, p 1319-1326.

[93] Irving H. Shames and Francis A. Cozzarelli, Elastic and Inelastic Stress Analysis, Revised Printing, Taylor and Francis, 1997.

[94] Li Weihua, Rheology of MR Fluids and MR Damper Dynamic Response: Experimental and Modeling Approaches, Ph. D Thesis, Nanyang Technological University, 2001.

[95] James V Beck and Keith A Woodbury, Inverse Problems and Parameter Estimation: Integration of Measurements and Analysis, *Measurement Science and Technology*, 1998, p 839-847.

[96] A Gavrus, E Massoni and J L Chenot, The Analysis of Inelastic Behaviour Formulated as an Inverse Rheological Approach, *Measurement Science and Technology*, 1998, p 848-863.

[97] I. M. Ward, Mechanical Properties of Solid Polymers, Second Edition, Chapman and Hall, 1996.

[98] Matthew Cartmell, Introduction to Linear, Parametric and Nonlinear Vibrations, Chapman and Hall, 1990.

[99] Christian Bonten and Ernst Schmachtenberg, A New Hypothesis to Describe the Mechanisms Acting in a Welded Joint of Semicrystalline Thermoplastics, *Polymer Engineering and Science,* Vol. 41, No. 3, March 2001, p 475-483.

[100] Aleksey D. Drozdov, Modeling the Viscoelastoplastic Behavior of Amorphous Glassy Polymers, *Polymer Engineering and Science,* Vol. 41, No. 10, October 2001, p 1762-1770.

[101] Xiangchao Li, Shih-Fu Ling and Zheng Sun, Heating Mechanism in Ultrasonic Welding of Thermoplastics, *International Journal for the Joining of Materials*, Vol. 16, No.2, June 2004, p 37-42.

[102] Xiangchao Li, Shih-Fu Ling and Zheng Sun, Dynamic Modulus Measurement of Thermoplastics Using a Ultrasonic Welding System, I-7-5, Symposium I, *International Conference on Materials for Advanced Technologies*, Singapore, December 07-12, 2003.

[103] Ying M, Ling S-F, Sun Z, Yang Q and Li X, Horn Design for Minimal Input Impedance of Ultrasonic Welding Systems, *The IIW Asian Pacific International Congress*, Singapore, 2002.

[104] M. Ying, S. -F. Ling, Z. Sun and X. Li, Enhancement of Converter Design for Ultrasonic Welding Systems, *The International Conferences on the Joining of Materials*, Helsingor, Denmark, 2003.

Appendix A

For the reciprocity theorem in this report, suppose the system is passive where energy can flow in either direction, such a system can be regarded as a reciprocal system. As we know, for the linear system, the relationships between the input variables e_{in} and f_{in} and the output variables e_{out} and f_{out} can be written as

$$\begin{bmatrix} e_{out} \\ f_{out} \end{bmatrix} = \begin{bmatrix} a_{11} & a_{12} \\ a_{21} & a_{22} \end{bmatrix} \cdot \begin{bmatrix} e_{in} \\ f_{in} \end{bmatrix}$$

where, the matrix containing a_{11}, a_{12}, a_{21}, and a_{22} is the transduction matrix of the system.

Selecting the output port of the system as the input port and the input port as the output port, and then rewriting the above equation, we have the following equations:

$$\begin{bmatrix} e_{in} \\ f_{in} \end{bmatrix} = \begin{bmatrix} b_{11} & b_{12} \\ b_{21} & b_{22} \end{bmatrix} \cdot \begin{bmatrix} e_{out} \\ f_{out} \end{bmatrix}$$

$$= \begin{bmatrix} a_{11} & a_{12} \\ a_{21} & a_{22} \end{bmatrix} \cdot \begin{bmatrix} b_{11} & b_{12} \\ b_{21} & b_{22} \end{bmatrix} \cdot \begin{bmatrix} e_{in} \\ f_{in} \end{bmatrix}$$

$$= \begin{bmatrix} a_{11}b_{11} + a_{12}b_{21} & a_{11}b_{12} + a_{12}b_{22} \\ a_{21}b_{11} + a_{22}b_{21} & a_{21}b_{12} + a_{22}b_{22} \end{bmatrix} \cdot \begin{bmatrix} e_{in} \\ f_{in} \end{bmatrix}$$

Identify the last matrix in the above equation as the identity matrix leads to the following relations:

$$a_{11}b_{11} + a_{12}b_{21} = 1$$

$$a_{11}b_{12} + a_{12}b_{22} = 0$$

$$a_{21}b_{11} + a_{22}b_{21} = 0$$

$$a_{21}b_{12} + a_{22}b_{22} = 1$$

The relations might seem difficult to solve, being a set of four nonlinear algebraic equations in eight unknowns. However, there is a unique, easily verified solution, which is given below:

$$a_{11} = b_{22}$$

$$a_{12} = -b_{22}$$

$$a_{21} = -b_{21}$$

$$a_{22} = b_{11}$$

According to the above relations, the elements of the transduction matrix are not independent, and related by the following equation:

$$a_{11}a_{22} - a_{12}a_{21} = 1$$

Appendix B

For the least square method proposed in this report, two things must be verified:

1) Show that the actuating mechanism has a unique solution T_{21}^{*} and T_{22}^{*}.

2) Show that this unique solution indeed minimizes $\prod$.

To show that the actuating mechanism has a unique solution:

This is equivalent to show that the homogeneous system

$$\begin{cases} \sum_{i=1}^{n} E_i V_i = T_{21} \sum_{i=1}^{n} E_i^{\,2} + T_{22} \sum_{i=1}^{n} E_i I_i \\ \sum_{i=1}^{n} I_i V_i = T_{21} \sum_{i=1}^{n} E_i I_i + T_{22} \sum_{i=1}^{n} I_i^{\,2} \end{cases}$$

has only the trivial solution, i.e.,

$$\begin{vmatrix} \sum_{i=1}^{n} E_i^{\,2} & \sum_{i=1}^{n} E_i I_i \\ \sum_{i=1}^{n} E_i I_i & \sum_{i=1}^{n} I_i^{\,2} \end{vmatrix} \neq 0$$

Suppose that

$$\begin{vmatrix} \sum_{i=1}^{n} E_i^{\,2} & \sum_{i=1}^{n} E_i I_i \\ \sum_{i=1}^{n} E_i I_i & \sum_{i=1}^{n} I_i^{\,2} \end{vmatrix} = 0$$

We can get,

$$\sum_{i=1}^{n} E_i^{\,2} \sum_{i=1}^{n} I_i^{\,2} = \left(\sum_{i=1}^{n} E_i I_i \right)^2$$

Expand the above equation, we can get

$$E_1^{\,2}I_1^{\,2} + E_1^{\,2}I_2^{\,2} + \ldots + E_1^{\,2}I_n^{\,2} + E_2^{\,2}I_1^{\,2} + E_2^{\,2}I_2^{\,2} + \ldots + E_2^{\,2}I_n^{\,2} + \ldots + E_n^{\,2}I_1^{\,2}$$

$$+ E_n^{\,2}I_2^{\,2} + \ldots + E_n^{\,2}I_n^{\,2} = E_1^{\,2}I_1^{\,2} + E_2^{\,2}I_2^{\,2} + \ldots + E_n^{\,2}I_n^{\,2} + 2E_1I_1E_2I_2 + \ldots$$

$$+ 2E_1I_1E_nI_n + 2E_2I_2E_3I_3 + \ldots + 2E_2I_2E_nI_n + \ldots + 2E_{n-1}I_{n-1}E_nI_n$$

It reduces to

$$(E_1I_2 - E_2I_1)^2 + \ldots + (E_1I_n - E_nI_1)^2 + (E_2I_3 - E_3I_2)^2 + \ldots + (E_2I_n - E_nI_2)^2$$

$$+ \ldots + (E_{n-1}I_n - E_nI_{n-1})^2 = 0$$

It implies that

$$\frac{E_1}{I_1} = \frac{E_2}{I_2} = \frac{E_3}{I_3} = \ldots = \frac{E_n}{I_n}$$

That means that input electrical impedance of the actuating mechanism keeps constant in the whole welding process. It is evident that the impedance could not keep constant in the welding process. Therefore, we can get

$$\begin{vmatrix} \sum_{i=1}^{n} E_i^{\,2} & \sum_{i=1}^{n} E_iI_i \\ \sum_{i=1}^{n} E_iI_i & \sum_{i=1}^{n} I_i^{\,2} \end{vmatrix} \neq 0$$

Hence, the actuating mechanism has only the trivial solution.

To show that the unique solution of the actuating mechanism indeed minimizes $\prod$:

Let T_{21}^* and T_{22}^* be the unique solution of the actuating mechanism. According to Equation 3.72, there will be

$$\prod = \sum_{i=1}^{n} [V_i - (T_{21}E_i + T_{22}I_i)]^2$$

$$= \sum_{i=1}^{n} [V_i - (T_{21}^*E_i + T_{22}^*I_i) + (T_{21}^*E_i + T_{22}^*I_i) - (T_{21}E_i + T_{22}I_i)]^2$$

$$= \sum_{i=1}^{n} \left\{ \left[V_i - (T_{21}^* E_i + T_{22}^* I_i) \right]^2 + 2\left[V_i - (T_{21}^* E_i + T_{22}^* I_i) \right] \cdot \left[(T_{21}^* E_i + T_{22}^* I_i) \right. \right.$$

$$\left. \left. - (T_{21} E_i + T_{22} I_i) \right] + \left[(T_{21}^* E_i + T_{22}^* I_i) - (T_{21} E_i + T_{22} I_i) \right]^2 \right\}$$

$$\geq \sum_{i=1}^{n} \left[V_i - (T_{21}^* E_i + T_{22}^* I_i) \right]^2$$

$$+ 2\sum_{i=1}^{n} \left[V_i - (T_{21}^* E_i + T_{22}^* I_i) \right] \cdot \left[(T_{21}^* E_i + T_{22}^* I_i) - (T_{21} E_i + T_{22} I_i) \right]$$

$$= \sum_{i=1}^{n} \left[V_i - (T_{21}^* E_i + T_{22}^* I_i) \right]^2$$

$$+ 2\sum_{i=1}^{n} \left[V_i - (T_{21}^* E_i + T_{22}^* I_i) \right] \cdot \left[(T_{21}^* - T_{21}) E_i + (T_{22}^* - T_{22}) I_i) \right]$$

$$= \sum_{i=1}^{n} \left[V_i - (T_{21}^* E_i + T_{22}^* I_i) \right]^2$$

$$+ 2(T_{21}^* - T_{21}) \sum_{i=1}^{n} E_i \left[V_i - (T_{21}^* E_i + T_{22}^* I_i) \right] + 2(T_{22}^* - T_{22}) \sum_{i=1}^{n} I_i \left[V_i - (T_{21}^* E_i + T_{22}^* I_i) \right]$$

Note that the second term is zero because of Equation 3.73. Hence, The above equation gives

$$\prod \geq \sum_{i=1}^{n} \left[V_i - (T_{21}^* E_i + T_{22}^* I_i) \right]^2$$

i.e., T_{21}^* and T_{22}^* minimizes $\prod$.

Since the actuating mechanism has a unique solution and the solution indeed minimizes $\prod$, the least square method can be used to calculate T_{21} and T_{22} during ultrasonic welding.

Appendix C

In the equivalent circuit of the converter, the transformer ratio N_C between the electrical and mechanical terms depends on the piezoelectric coupling coefficients, defined as

$$N_C = \frac{E_2}{E_1} = \frac{I_1}{I_2} = \frac{eA_c}{l_c}$$

where E_1 and I_1 are the input voltage and current of the transformer; E_2 and I_2 are the output voltage and current; e is the piezoelectric stress constant; l_c is the thickness of the PZT disks; A_c is the cross sectional area.

R_0 and C_0 can be gotten from

$$R_0 = \rho \frac{l_c}{A_c}$$

$$C_0 = \frac{\varepsilon^S A_c}{l_c}$$

where ρ is the resistivity of the PZT material, and the dielectric constant ε^S is the permittivity with zero strain.

According to Standard Definitions and Methods of Measurement for Piezoelectric Vibrators, the values of R_c, C_c and L_c can be obtained using transmission circuit method. The mechanical reactance X_c combined by C_c and L_c is well approximated near resonate for a symmetrical transducer by

$$X_c = -Z_c \pi (1 - r)$$

where $Z_c = \rho V_s A$ is the characteristic impedance, V_s is the velocity of sound in the PZT material, ρ is the density of the material, and $r = f / f_n$ is the operating frequency to the resonant frequency. From this equation, we can see that X_c is zero when the transducer assembly is operating at its resonant frequency.

In the equivalent circuit of the booster, the transformer ratio N_B is defined as

$$N_B = \frac{A_{b1}}{A_{b2}} = \frac{V_{b2}}{V_{b1}}$$

where A_{b1} and V_{b1} are the cross-sectional area and the velocity at the input port of the booster, and A_{b2} and V_{b2} are the cross-sectional area and the velocity at the output port of the booster.

In the equivalent circuit of the horn, the transformer ratio N_H is defined as

$$N_H = \frac{A_{h1}}{A_{h2}} = \frac{V_{h2}}{V_{h1}}$$

where A_{h1} and V_{h1} are the cross-sectional area and the velocity of the input port at the horn, and A_{h2} and V_{h2} are the cross-sectional area and the velocity at the output port of the horn.